The Origin of Tharsis - A Deep Mantle Gravity Study

MSc. Thesis

Y. van der Tang

Delft University of Technology

TU Delft Delft University of Technology

Challenge the future

The Origin of Tharsis - A Deep Mantle Gravity Study

MSc. Thesis

by

Y. van der Tang

to obtain the degree of Master of Science
at the Delft University of Technology,
to be defended publicly on April 16th, 2021 at 10:00 AM.

Student number: 4712951
Project duration: September 1, 2020 – April 16, 2021
Thesis committee:

Dr. ir. B. C. Root,	Delft University of Technology, Supervisor
Dr. ir. W. van der Wal,	Delft University of Technology, Chair
Dr. R. E. M. Riva,	Delft University of Technology

An electronic version of this thesis is available at http://repository.tudelft.nl/.

Front image: Mars captured by Hope Probe (Mohammed bin Rashid Space Centre)

TU Delft

ABSTRACT

The gravity potential field of Mars is characterized by a long-wavelength feature located at the Tharsis region. In addition, this region houses large volcanoes that have been active until geologically recently (200 to 100 Ma ago). Research has not succeeded in pinpointing the cause of this long-wavelength areoid high, while some researchers claim it is due to a mantle plume, others suggest that it is caused by volcanic construction and the associated flexure in the lithosphere. This work aims to contribute to resolving this question with the development of a new mantle convection model for Mars. It is renewing in four aspects; (1) A Mars model is developed in SFEC (Tosi, 2007), which has been primarily used for Earth studies, (2) mantle anomalies are analysed in order to determine whether they could be involved in the creation of the Tharsis volcanoes, (3) the solutions challenge the current views upon the (pre-dominantly isostatic) support of Tharsis and (4) a new method is developed to assess the similarity of models and observations for low degree spherical harmonics ($n < 5$) fields. The research contributes to a better understanding of the Martian interior and the volcanic activity in the Tharsis region.

Seismic studies of the Earth's interior have correlated large provinces on the core-mantle-boundary with plume generation and hotspots that arise on Earth's surface. This research investigates whether similar structures in the Martian mantle could be connected to, or even be the cause of, the volcanism in the Tharsis region. Firstly, a crustal reduction is performed to obtain the gravitational field of the mantle and core. An Airy model is used for this as research found this to be the dominant form of compensation for long-wavelength features on Mars (Mussini, 2020). Subsequently, density anomalies are positioned in the mantle and their gravity potential is computed and compared with the observations.

The results of these models show a set of positive density anomalies that fit the observations. These solutions are primarily located between depths of 400 and 1000 km. For the best-performing model, the required density contrast $\Delta\rho$ is 400 kg/m^3. Such a density variation in the mantle is, geophysically seen, unlikely to be a realistic solution. To improve this model, the stresses caused by the density anomaly are taken into account. As a consequence of the stresses, boundary deformations of the surface and CMB topography occur and therefore the gravitational potential changes as well. Moreover, the observed topography is added as an additional constraint. With this addition, the results indicate that the observed topographic and gravity high can only be caused by a negative density anomaly at just 500 km below the surface. Therefore, the possibility of structures similar to the large-low-shear velocity provinces on the CMB being the primary cause of the observed long-wavelength feature is rendered unlikely. A solution that was found is a mantle superplume from the CMB up to a depth of 500 km with $\Delta\rho$ = -89 kg/m^3, corresponding to a temperature anomaly of approximately 847 K. In contrary to recent studies, the best-fitting solutions suggests scenarios in which Tharsis is almost completely supported by dynamic uplift, and isostatic compensation only contributes a minor part. This finding partially originates from the assumption of Airy support on long-wavelength features and the use of an instantaneous viscous flow mantle convection model.

The main recommendation is the implementation of a thin shell elastic crust to account for flexural isostasy, which has been proven to alter the contribution of dynamic support. Moreover, all results indicate a negative (buoyant) density anomaly, meaning an upwards motion of mass to the surface. The obtained superplume solution is currently rising with approximately 35 cm / yr towards the surface. Because the contribution of such anomalies to the long-wavelength gravitational field is large, one might be able to detect the movement by analysing temporal gravitational data. SFEC has proved to be a good candidate for future Mars convection studies, especially because its low computational requirements with respect to other mantle convection software. The code could be improved by enabling a time evolution instead of limiting the computation to instantaneous viscous flow. It could give better insights into time-dependent flexural responses which are proved to be more important in Mars compared to Earth studies.

PREFACE

This MSc thesis marks the end of a great time as an Aerospace Engineering student at Delft University of Technology. Studying Space Exploration reminded me day after day of the beautiful universe that we are part of. I believe mankind will discover extraterrestrial life, walk the surface of Mars and reveal many mysteries of the planets in, and beyond, our solar system. The end of my time as a student indicates the start of new journeys, in which I strive to contribute to this future of space exploration.

The research is about the Tharsis region on Mars [1], which is home to the largest known volcanoes in the solar system. A gravity and convection study is performed to determine whether this volcanic region could be related to density anomalies in the Martian mantle, similar to Large Low Shear Velocity Provinces in Earth's mantle. I am grateful for having Bart as my supervisor, his guidance and weekly meetings brought fruitful discussions and interesting insights. His enthusiasm and optimism supported me in conducting this research and in writing this work. In addition, I would like to thank the research group and especially Aaron and Weilun for the frequent meetings and their feedback on this work. Finally, my gratitude goes towards the graduation committee for their time and effort.

Youandi
Delft, April 2021

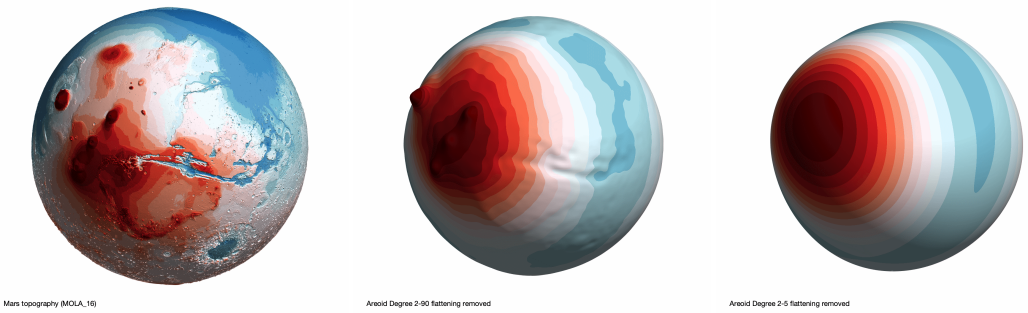

[1] Why Mars should intrigue you - Human missions to Mars are coming closer and closer to realisation. At first, as exploration missions in the search for extraterrestrial life, signs of previous life, and liquid water. Subsequently, with the goal to find a place to settle and start a civilisation on Mars, making humankind a multi-planetary species. Everything that makes Earth look alive is absent on Mars; oceans, vegetation, a turbulent atmosphere and much more. One might even conclude that it is an uninteresting giant rock. However, one couldn't be more wrong. Think of a human lifetime; in the younger years one is energetic, expressing itself in extraordinary ways, fertile and ready to create, bear and nurture new life. Research suggests that Mars was like this: fully active, a possible host of life, liquid oceans and enormous volcanic eruptions, releasing the heat from within. But Mars has matured and those features have disappeared, similar to a human ageing. The beautiful consequence is that elderly are wise, contain a tremendous amount information about their past and can even provide us with useful insights and perspectives for the future. Because Mars is smaller, the planet's cooling mechanism has cooled off the planet much quicker with respect to Earth. It is therefore in a further stadium of planetary life, that for Earth is yet to come. Scarred by its past experiences, Mars does not only tell a beautiful story with many mysteries to be unraveled, but could also give mankind a better understanding of Earth and its driving processes.

Contents

List of Figures

LIST OF TABLES

NOMENCLATURE

$\Delta\rho$	Density anomaly	kg/m^3
δg_B	Bouguer gravity correction	mGal
ΔT	Temperature Anomaly	K
η	Reference viscosity	10^{22} Pa s
λ	Equivalent wavelength	km
μ	$G \cdot M_{Mars}$	$0.042828 \cdot 10^6$ kg^3/s^2
ρ_{core}	Core density	kg/m^3
ρ_c	Mean crustal density of Mars	2900 kg/m^3
ρ_M	Mean density of Mars	3933 kg/m^3
ATR	Areoid-to-Topography Ratio	m/km
C_a	Center of Anomaly	[deg,deg]
C_{20}	SH coefficient containing hydrostatic flattening	–
C_{nm}	Spherical harmonic coefficients	–
D_a	Anomaly depth	km
DV	Degree Variance	-
G	Gravitational Constant	$6.67384 \cdot 10^{-11}$ N m^2/kg^2
g_B	Bouguer gravity anomaly	mGal
g_F	Free-air gravity anomaly	mGal
g_T	Gravity correction due to terrain unevenness	mGal
g_{Mars}	Surface gravity of Mars	3.71 m/s^2
Ga	Giga-annum	$1 \cdot 10^9$ years
h	surface elevation	km
H_0	Zero-elevation crustal thickness	km
I	Intersection of two shapes	m^2
m	Spherical Harmonic order	–
M_{Mars}	Mass of Mars	kg
Ma	Mega-annum	$1 \cdot 10^6$ years
N	Areoid height	m
n	Spherical Harmonic degree	–
R	Equatorial radius of Mars	3396 km

r	Radial distance	km
R_{core}	Assumed core radius of Mars	1700 km
S_{lat}	Latitude range of Anomaly (up and down with respect to C_a)	[$\deg_{up}$,$\deg_{down}$]
S_{lon}	Longitude range of Anomaly (left and right with respect to C_a)	[$\deg_{left}$,$\deg_{right}$]
S_{total}	Similarity	-
T_a	Anomaly thickness	km
U	Union of two shapes	m^2
V	Gravitational Potential Mars	m^2 / s^2
V_s	Relative shear-wave velocity contrast	%
V_{nm}	Stokes Coefficients	–
$Y_{nm}(\theta,\phi)$	Surface spherical harmonic functions	–

ACRONYMS

ATR Areoid-to-Topography Ratio. 10

CMB Core–Mantle Boundary. 5

GSH Global Spherical Harmonic. 15, 40

GSHA Global Spherical Harmonic Analysis. 15

GSHS Global Spherical Harmonic Synthesis. 15

HPE Heat Producing Elements. 66

IVF Instantaneous Viscous Flow. 72

LIP Large igneous province. 5

LLSVP Large low-shear-velocity province. 5

MGS Mars Global Surveyor. vi, 2

MOLA Mars Orbiter Laser Altimeter. vi, 2

MP MaxPeak- Highest gravity field value. 18

PGZ Plume Generation Zone. 5

RMS Root Mean Square. 10

RMSE Root Mean Square Error. 20

SFEC Spectral Finite Elements Convection. 21

SH Spherical Harmonics. 11

1

INTRODUCTION

Named after the Roman God of war, Mars is the fourth planet counted from the sun and the second smallest planet in our solar system. It is often referred to as "The Red Planet" due to its red color when observing it from a distance. This color is the result of iron which oxidized over time and formed a dusty rust layer. Besides its reflective spectrum, Mars is characterized by the absence of an atmosphere, oceans, vegetation and complex life. Its surface contains a large amount of impact craters, Hellas Planitia being the largest one. Moreover, Mars has two features that distinguish it from any other planet; the Martian dichotomy and the Tharsis region. The dichotomy is the sharp elevation contrast between the Northern and Southern hemisphere, in which the Northern hemisphere is 1 to 3 kilometers lower than the Southern hemisphere. The Tharsis region is characterized by shield volcanoes, a large valley (Valles Marineris), its fault patterns, geological information and a high gravity signal. Furthermore, it is the home of the largest known volcano in our solar system; Olympus Mons. A visualization of Mars is presented in Figure 1.1.

Figure 1.1: True color visualization of Mars, oriented at the Tharsis region. Image retrieved from NASA (1999).

In this thesis, the Tharsis region is investigated by using topography and gravity data. As can be seen in Figure 1.1, there are enormous volcanoes located in this region. The potential relationship between structures in the mantle and the volcanism that is observed on the surface is explored. In Section 1.1, the Tharsis region is discussed in more detail. Subsequently, Section 1.2 elaborates upon Earth's deep mantle structures and its relationship to volcanism. Ultimately, the research questions are formulated in Section 1.3.

1.1. THARSIS REGION

Tharsis is positioned in the Martian Western hemisphere, centered a few degrees south of the equator at a longitude of 95 ° W (Golabek et al., 2011). Because of its extreme topographic anomalies ranging from a depth of approximately 7 km in Valles Marineris up to a height of 22 km for Olympus Mons, the Tharsis region is one of Mars' largest features. Two topographic maps, one of Mars and one specifically of Tharsis, are presented in Figure 1.2.

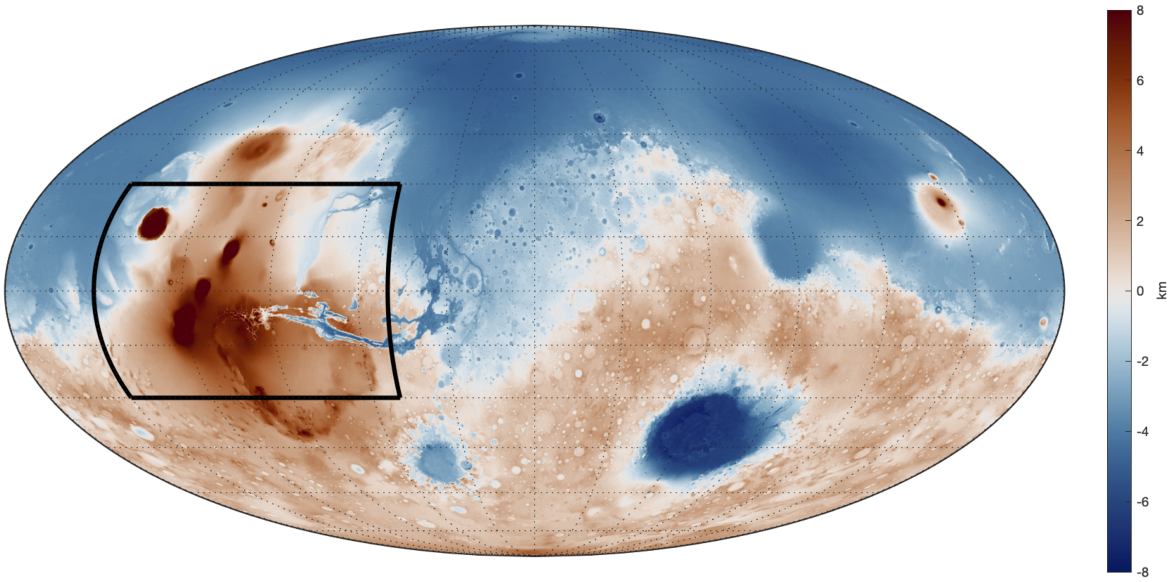

(a) Topography map of Mars with respect to areoid, represented in a Mollweide projection with a central meridian of 0 ° longitude. The Tharsis region is indicated by the black outline. The colorbar has been clipped at -8 and 8 km to dampen the distorting effect of Olympus Mons.

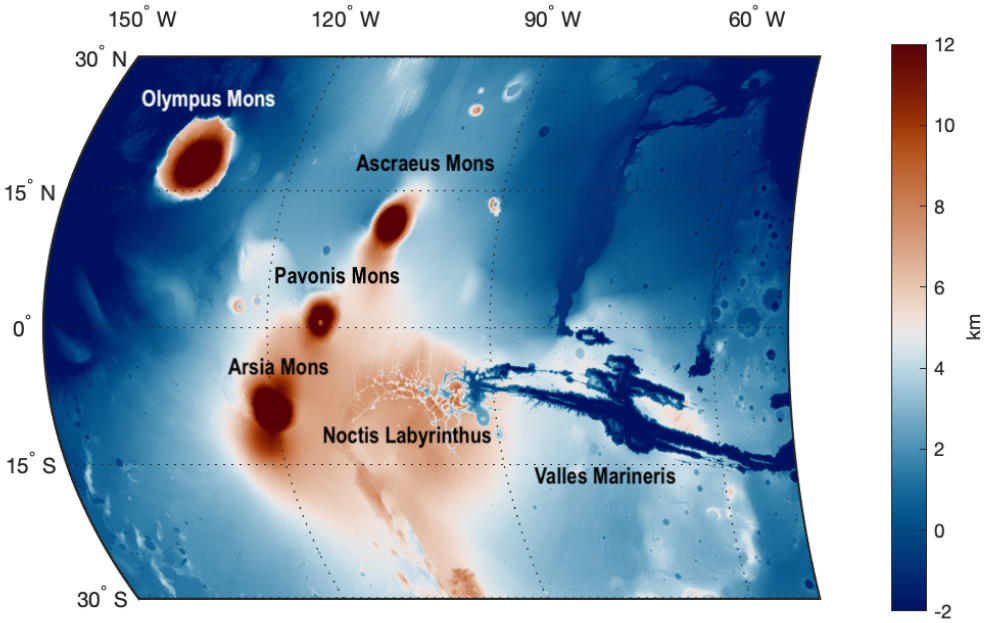

(b) A close-up of the topography of the Tharsis region as was indicated by the black outline in Figure 1.2a. The map is a Mollweide projection with a central meridian of 100 ° W longitude. The center of the colorbar approximately indicates the mean elevation of Tharsis and the bar has been clipped at -2 and 12 km. Several features have been labeled with their corresponding names.

Figure 1.2: Topographic maps with respect to the areoid. The data used for both figures is 64 pixels/degree topography from the MOLA instrument on board of the MGS. Data source: Smith (2003). The colorbars have been clipped at different limits according to their regional characteristics.

Several remarkable observations can be made on the basis of the Martian topographic map (Figure 1.2a). Firstly, the crustal dichotomy is a very distinct feature; the Southern hemisphere is primarily red (elevated) and the Northern hemisphere is approximately 3 kilometers lower. Secondly, the Tharsis region is uplifted with respect to the surrounding areas and large volcanic constructs are present. Another distinct feature is Hellas Basin, a crater positioned in the Southern hemisphere that reaches a depth of 7 kilometers. Henceforward, the primary focus will be upon the Tharsis region, which is described in Figure 1.2b. In the top left corner, a dark red (high topography) feature centered at about 18° N latitude and 135 ° W longitude can be seen, this is Olympus Mons. With 25 km in height with respect to its surroundings, it is the tallest, known volcano in our solar system. Olympus Mons consists of several calderas and has a diameter of 550 km. Besides, the volcano was active until geologically recent timescales of about 165 Ma ago (Robbins and Achille, 2011). The Tharsis Montes consists of three large shield volcanoes positioned in almost a perfect straight line (chain); Arsia Mons, Pavonis Mons and Ascraeus Mons (Werner, 2009; Neukum and Hiller, 1981). From Arsia Mons up to Ascraeus Mons, a decreasing surface age is observed, which might indicate that they are the result of a hotspot moving Northeast relative to the crust. Young flank eruptions indicate very recent activity of the volcanoes (Werner, 2009). Valles Marineris (the blue region valley-shaped region at latitude of 10 ° S and a longitude of 100 ° to 50 W °) is a manifestation of canyons up to 7 km deep. This research will focus on the support of this volcanic region and on investigating the possibility of having a correlation between the remarkable topography of Tharsis and mantle structures. A feature that is not visible on topographic maps like the ones presented in Figure 1.2, are faults.

1.1.1. FAULT PATTERNS

A fault is a crack or fracture in the solid surface, often caused by large stresses. Once a fault has been formed, the two separated bodies of rock can move independently from one another, this movement can result in Mars quakes, analogous to Earthquakes. The fault pattern could contain valuable information about stresses on the Martian surface, such knowledge might shed light on the main forces that have acted upon the surface, for instance a dynamic supporting force of flexure in the lithosphere. Moreover, relative ages of faults can be determined, resulting in an age determination of the surface, independent of crater statistics (Knapmeyer et al., 2006).

As can be seen in Figure 1.3, the extensional faults (colored red) are mainly located at the periphery of Tharsis, at the heavily cratered red stippled pattern. This is an indication that volcanic material on Tharsis is younger than the faults, as the faults were covered by the volcanic material.

The extensive fault systems could be a result of an uplift of the Tharsis, whereby a single-layer mantle stretches the crust. However, Wise et al. (1979) proposed a multiple-layer model with gravity spreading of shallow brittle layers since this is more harmonious with the fault structure that is created. In addition, this study supports the claim that Tharsis volcanism postdates the period of intense faulting. A study by Banerdt et al. (1982) also investigated the possible cause of this fault pattern around Tharsis. They found that a dynamic support (uplift) of the lithosphere would cause circumferentially positioned features within the supported region and radial features in the periphery. For isostatic features this is the other way around. However, the fault pattern that is observed shows the radial (extensional) features also in the supported region and the circumferential features seem to correspond to the compressional faults in the periphery of Tharsis. Bases on this,, the authors dismissed a flexural uplift at Tharsis and state that the faulting pattern around Tharsis is better explained by isostasy and flexural loading.

The proposed process for the evolution of Tharsis begins with a convection cell causing subcrustal erosion. When this ceased, the eroded material was underplated beneath Tharsis, this produced a rapid rise of the Tharsis. Subsequently, the gravity sliding produced the observed radial fault system. Three and a half billion years ago the astenosphere cooled and became solidified, stopping the gravity sliding and radial faulting. Carr (1974) showed that the formation of the Tharsis bulge likely happened before the formation of the volcanoes and that the bulge could have been supported by a dynamic uplift. One of the conclusions is that such a fracture pattern is unlikely to be caused from local events, but as a results of a single, discrete event. The observation that the fracture pattern is not symmetrical can be explained by the asymmetric shape of the dynamic uplifting bulge (Carr, 1974).

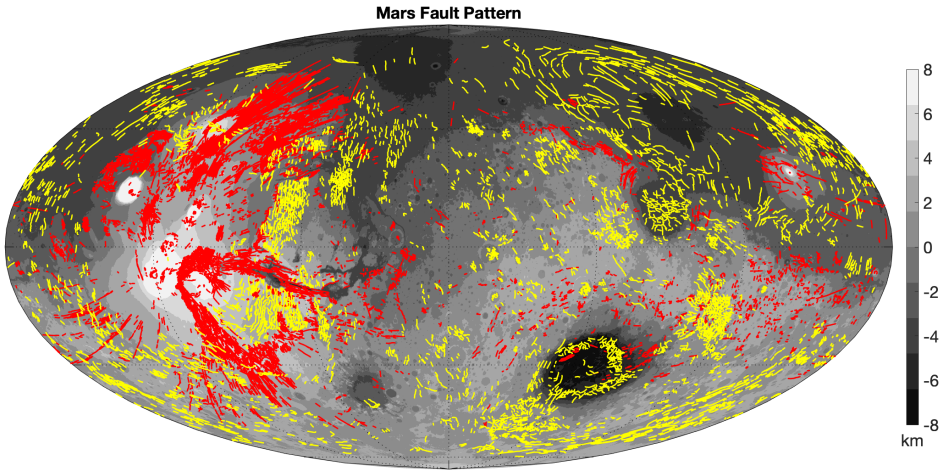

Figure 1.3: A representation of the fault patterns on Mars, the compressional faults are marked in yellow, the extensional faults in red. Data was obtained from Knapmeyer et al. (2006). The map is a Mollweide projection with a central meridian of 0 ° longitude. The topographic colorbar has been clipped at -8 and 8 km.

Another observation to take into account is the volcanic history and activity in the Tharsis region, this requires a long-lasting supply of heat. Schubert (1990) indicate that certain regions such as Tharsis may have a weakened lithosphere that enable a strong heat flow very localized (at the locations of the shield volcanoes). The volcanic activity in the Tharsis region is characterized by a periodicity. This could be explained by a recurring mechanism such as presented by Breuer et al. (1996); their mantle flow model showed that long-lasting super-heated plumes are characterized by period of extreme activity and could be the cause of the observed changes in activity at Tharsis. Additionally, the stress-effect of such a periodicity has been correlated with the observed tectonic activities (Mège and Masson, 1996). It could be possible that there is currently such a magmatic activity under Tharsis causing the observed dynamic uplift.

The fault patterns gives an additional set of constraints that could be helpful in the interpretation of the results. Whether mantle anomalies are the cause of the gravitational and topographic uplift of Tharsis or whether other processes are in play, the findings should be in congruence with the stress field and fault pattern studies on Mars. The fault patterns primarily give information about Mars' past and how this can be correlated to the creation of the Tharsis region. The Tharsis region remains to be topographically uplifted, possible explanations for this are given in the next section.

1.1.2. ORIGIN OF SUPPORT

According to Wise et al. (1979), the development of Tharsis can be divided into two separate processes. Firstly, a rapid topographic rise happened, resulting in the formation of a gigantic fault system. This was followed by a long stage of volcanism caused by a hot underplate under the Tharsis. This underplate, resulting in radial gravity motions of layers, could also be the cause of the radial fault system that is observed on Mars. However, the question remains how this topographic rise could have happened, and how this remains stable. Studies into the origin and support of the topographic rise of Tharsis have generated several potential explanations.

Several processes could be responsible for origin and support of Tharsis and it is difficult to pinpoint one specific process. Currently, there are two main, non-mutually exclusive, theories (Zhong and Roberts, 2003; Zhong, 2002):

1. A thermal plume in the mantle supports the Tharsis Rise (Kiefer and Hager, 1989; Harder and Christensen, 1996; Breuer et al., 1996)
2. The topographic anomalies are a combination of volcanic construction and lithospheric flexural events (Turcotte et al., 1981; Phillips et al., 2001; Wise et al., 1979).

Neither one of those theories can explain the origin of the Tharsis Rise separately, but the theories can coexist. There probably is a superposition between those two theories that results in the long-wavelength topographic and areoid anomalies in the Tharsis Rise (Redmond and King, 2004). According to Zhong and Roberts (2003) and Kiefer and Hager (1989), there also has to be a large heat source in the form of mantle upwellings to provide for the recent volcanic activity, which could imply the existence of a deeper mantle plume source as suggested by Redmond and King (2004).

Tharsis is characterized by a high gravity field at its center and a ring of low gravity field around it. A similar phenomenon is observed in Earth, where tomographic studies of the mantle have revealed structures called Large low-shear-velocity provinces (LLSVPs). Those structures cause a higher observed gravity field and could be related to the hotspot-volcanism that manifests itself on the surface. The question arises whether Mars' mantle could accommodate similar structures deep in the mantle, being correlated to the high gravity field and potentially also to the generation of the volcanism. Furthermore, such structures in the mantle or near the Core–Mantle Boundary (CMB) could have played a role in the formation and support of Tharsis. The role of deep mantle anomalies in support of Tharsis is elaborated upon in the following section.

1.2. MANTLE STRUCTURES

There are two data driven methods to observe the deep mantle: gravity and seismic studies. On Earth, two large reservoirs, one under the Central Pacific and one under Africa, have been found by the first seismic studies of Earth's interior (Dziewonski and Anderson, 1981). They are characterized by a low shear-wave velocity, therefore the reservoirs are called: Large low-shear-velocity provinces (LLSVPs). Debates are still ungoing about the nature of those regions, for instance whether they are chemically distinct from the surrounding mantle (e.g. (Ishii and Tromp, 1999; Ni et al., 2002; McNamara and Zhong, 2005; Zhang et al., 2012). In addition, it is not yet clear whether the average density of the LLSVP is higher than the surrounding mantle (e.g. (Li et al., 2018)) or lower (e.g. (Ishii and Tromp, 1999; Koelemeijer et al., 2017)). A correlation between the location of these deep mantle structures and the volcanism on the surface has been found, this finding is elaborated upon in the next section.

DEEP MANTLE RESERVOIRS AND VOLCANISM

For many years, researchers have theorized about the origin of hotspot volcanoes. Because the location of eruption sites changes over time it seems that the relative movement of the crust and mantle is relevant, it is expected that the origin is in the mantle (Gripp and Gordon, 1990). Whether the source is in the upper mantle or lower mantle is still debated (Courtillot et al., 2003), but the current models strongly suggest that the source lies in the deep mantle, in the region of the Core-Mantle Boundary (DePaolo and Manga, 2003). Geo-chemists have hypothesized for decades about isolated reservoirs (LLSVPs) in the deep mantle that were not part of the mantle convection cycle (Burke et al., 2008; Trønnes, 2010). Burke et al. (2008), Burke and Torsvik (2004) and Torsvik et al. (2006) showed that it was unlikely that the LLSVPs have changed significant mass in the last 0.3 Ga. It could be the case that they are even isolated for a duration of 2.5 Ga. According to Torsvik et al. (2006), this stability of LLSVPs is consistent with independent evidence of the reservoirs being compositionally distinct and not just a structure with simply a higher temperature.

The tomographic anomalies are correlated to the global hotspot distribution (Burke et al., 2008; Anderson, 1981). The eruption zones, Large igneous provinces (LIPs), have to be a result of huge amounts of internal heat dissipation (Burke and Torsvik, 2004), which is believed to be caused by eruptions from major plumeheads that came all the way from LLSVPs on the CMB (Richards et al., 1989; Burke et al., 2008). Mantle convection is the primary process of transporting the heat that is required for plume formation (Kiefer and Hager, 1989). Based on such geodynamic and mantle convection studies, it was shown that there is a high correlation between the position of the LLSVP boundaries and the manifestation of volcanism on the surface (Davies et al., 2015; Torsvik et al., 2006). The correlation of the eruption locations and the LLSVPs was obtained by using a paleomagnetic reference frame. In this reference frame, the past positions of plates are taken into account. In total, 25 LIPs have been restored to their eruption site from which ninety percent of the LIPs correlated with the position of the LLSVPs in the deep mantle (Burke and Torsvik, 2004). The generation of the plumes is expected to be at the margins of the LLSVPs, at the so-called Plume Generation Zones (PGZs) (Torsvik et al., 2006; Burke and Torsvik, 2004; Torsvik et al., 2010). According to Burke et al. (2008), the LIPs cannot be connected to anything else in the deep mantle than the PGZs. However, according to Li and Zhong (2017) and Zhong and Liu (2016), the evidence is not as clear as Burke et al. (2008) claim it to be.

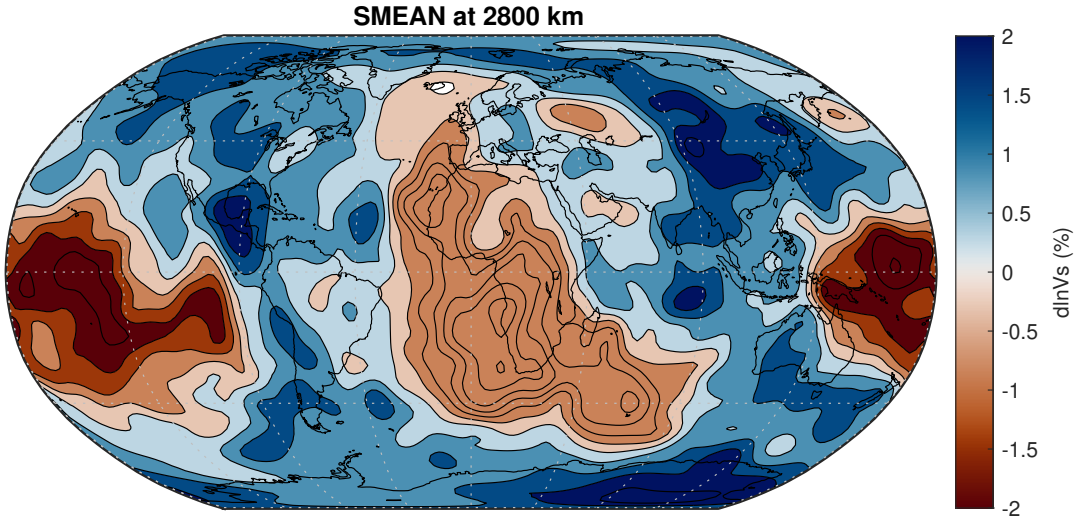

(a) Earth SMEAN model representing seismic shear-wave velocities with respect to the surrounding mantle at a depth of 2800 km ((Becker and Boschi, 2002)). Two provinces with a low shear-wave velocity are visible: on located under Africa and in the mantle under the Pacific ocean. The colorbar has been clipped at -2 and 2 % of V_S with respect to the surrounding mantle.

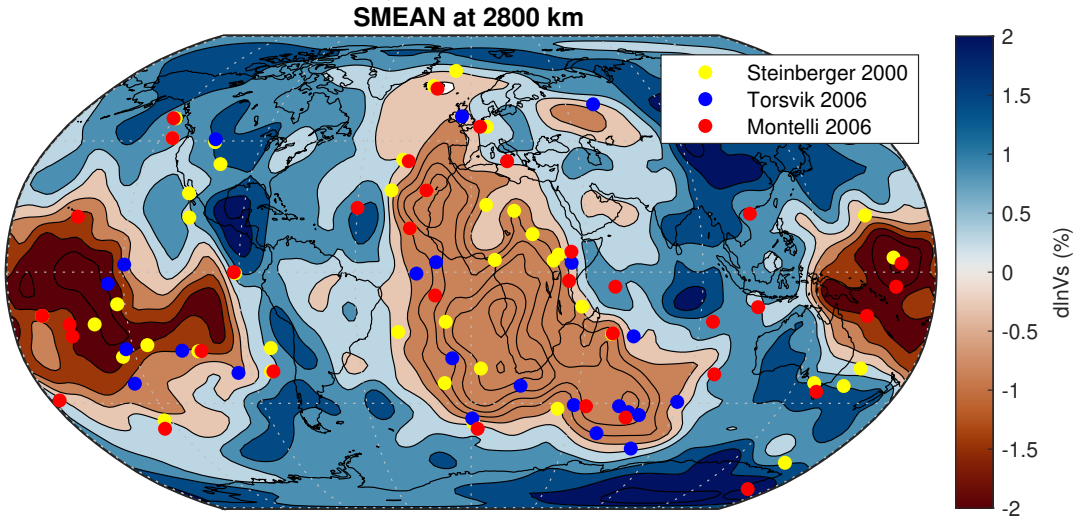

(b) Distribution of the LLSVPs, presented in Trønnes (2010). The yellow and blue dots are LIP-sites restored to their original eruption locations (Steinberger, 2000)(Torsvik et al., 2006). The red dots are locations of deep mantle plumes (Montelli et al., 2006). The colorbar has been clipped at -2 and 2 % of V_S with respect to the surrounding mantle.

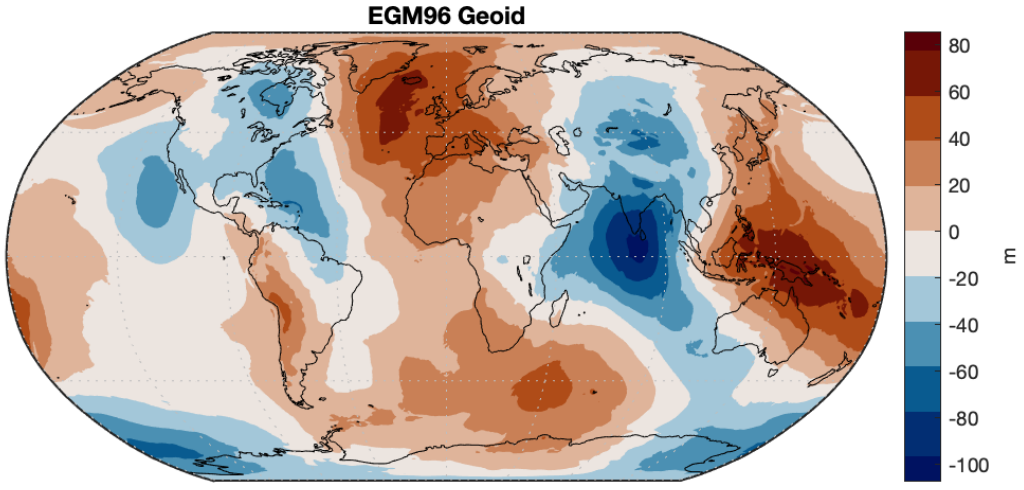

(c) EGM96 geoid, inspired upon Davies et al. (2015); Becker and Boschi (2002).

Figure 1.4: Robinson projections of Earth with a central meridian of 0 ° longitude. This image is inspired upon the work of Davies et al. (2015).

This is also supported by studies of Tan et al. (2011) and Kimura and Kawabata (2015) in which they developed convection models that resulted in the generation of mantle plumes not only at pile edges, but also in the middle and on top of the piles as well as far outside the piles (Li and Zhong, 2017). Moreover, there was a debate about the statistical method used to determine the spatial correlation of LLSVP margins and LIPs (Li and Zhong, 2017; Austermann et al., 2014; Davies et al., 2015; Doubrovine et al., 2016). Until today, the spatial correlation found by Torsvik et al. (2006) has not been demonstrated to be false and this is used as one of the primary motivators of setting up this study. Figure 1.4a presents the locations of the LLSVPs, the locations of the reconstructed eruption sites are presented in Figure 1.4b. Figure 1.4 shows the SMEAN model at a depth of 2800 km and the observed geoid (EGM96) (Becker and Boschi, 2002). A correlation, especially on the long-wavelength structures can be observed between the regions with a low shear wave velocity and a high geoid. Note that most of the hotspots are located closely to the margins of the LLSVPs. In addition, geoid represented in Figure 1.4c shows an elevated geoid above the Pacific LLSVP. Although not presented in Figure 1.4c, the "Residual Geoid" shows an even clearer correlation between the geoid signal and the location of LLSVPs (Burke et al., 2012). The residual geoid is the field that is left after removal of the geoid effects caused by the upwellings, for example at Iceland, and subduction-zones, such as the Andes (Hager, 1984; Kiefer and Hager, 1989).

All in all, a correlation has been found between structures in the Earth's mantle and eruption sites on the surface. Moreover, there is a high correlation between the position of those structures and the observed elevated residual geoid. For Mars, Steinberger et al. (2010) found a similar relationship; volcanism occurs primarily at regions with an observed areoid high. They also inferred that such a large gravitational signature would probably be due to density anomalies in the mantle. Nonetheless they were not able to determine whether there are structures similar to Earth's LLSVPs in the deep mantle of Mars. A similarity between the relationships of volcanism and gravitational potential on Earth and Mars might indicate that the volcanism is caused by the same mechanism at plume generation zones near the boundaries of deep mantle anomalies.

1.3. RESEARCH QUESTIONS

It has been suggested that hotspot-volcanism on Earth is correlated to the LLSVPs that are positioned in the deeper mantle. Furthermore, a relationship between the LLSVPs and the observed geoid has been found. For Mars, a similar relationship between volcanism and the observed areoid was discovered by Steinberger et al. (2010). Therefore, it would be interesting to investigate whether there are structures in the Martian mantle similar to the LLSVPs on Earth that are related to the volcanism and areoid. Since the magnitude of the volcanoes on Mars is larger than those on Earth, while Mars is significantly smaller, it might indicate that the volcanism-generating zones are more dominant and easier to find. Besides, the absence of plate tectonics on Mars in combination with the recent volcanic activity, might indicate that the volcanic regions (e.g. Tharsis) are exactly radially above a plume generation zone or a mantle anomaly. Thus, the research question is:

Could the unique volcanic topographic features of the Tharsis region be related to density anomalies in the Martian mantle?

This question is divided into the following sub-questions:

1. *What constraints can be put on the gravity field data to find anomalies in the mantle?*
   (a) What wavelength gravity field data reveals information about the lower mantle of Mars?
   (b) What information is available on the Martian gravity field and how can the deep mantle be modelled?
   (c) Are there crustal models of Mars available?
   (d) Can the thickness and density contrast of the anomalies be constrained by using existing mantle models?
2. *What could be possible explanations for density anomalies in the mantle of Mars?*
   (a) Assuming crustal models have acceptable uncertainties, how could we develop models for the Martian mantle?

(b) What would be the effect of temperature variations on the gravity field findings?
(c) What would be the effect of variations in composition on the gravity field findings?
(d) What would be the effect of Core Mantle Boundary topography on the gravity field findings?

3. *What could be possible relationships between mantle density anomalies and volcanism?*

(a) Is there a geological relationship between mantle gravity anomalies and the volcanic features on Mars?
(b) Is there a geological relationship between mantle composition and the volcanic features on Mars?
(c) What is the relationship between LLSVPs found in the deep mantle of the Earth and possible deep mantle density anomalies in the Martian mantle?

Answers to these questions could develop our understanding of the Martian mantle. In addition, it could give more insight into the origin of the Tharsis region. If there can be found similarities between structures in the deep mantle of Mars and the LLSVPs on Earth, one could get more insight into the origin of hotspot volcanoes on Earth and the dynamics of the mantle of both planets.

Chapter 2 discusses the method and tools used throughout this research. It elaborates upon the usage of Martian gravity data and how this is used to determine contributions due to mantle anomalies. This approach is validated and verified in Chapter 3. The method is used to obtain results for three types of models, each researching the effect of density anomalies in the mantle. The DA-models assume a simplified scenario in which stress interactions due to the density anomaly are neglected, the GSH code is used for these models [1]. The BD-grav-models research the effect of placing a density anomaly in the mantle while also taking into account interactions (mantle convection), SFEC [2] is used for this purpose . The third type, the BD-Hybrid models, take into account the observed topography as an additional constraint. The results are presented in Chapter 4. Subsequently, Chapter 5 discusses the findings and method. Ultimately, Chapter 6 draws the conclusion of this study.

[1] Software: Global Spherical Harmonic Analysis (Root et al., 2016)
[2] Software: Spectral Finite Element Convection with 1D viscosity and 3D response (Tosi, 2007)

2

METHOD

Currently, only one seismometer is placed on Mars; the SEIS instrument on board of Insight. With only one seismometer it is not feasible to accurately trace back the impact location of an event (Böse et al., 2017). This also makes it impossible to detect deep mantle structures using the seismometer. Therefore, only gravity and topography data has been used to investigate the mantle of Mars for possible anomalies. This chapter describes the approach of obtaining the results. Section 2.1 elaborates upon the pre-processing steps of the gravity data that has been performed. After the removal of crustal contributions, the gravity contributions due to mantle anomalies were investigated, this approach is elaborated upon in Section 2.3. Additionally, the boundary deformations that are a result of placing anomalies in the mantle, have been determined. Section 2.4 discusses this process. Subsequently, Section 2.4.3 shows how to the topography is taken into account as an additional constraint. In total, four models are introduced. The tools used for assessing the performance and sensitivity of a model are explained in Section 2.4.4.

2.1. PRE-PROCESSING GRAVITY DATA

Each body in the universe that has mass, creates a gravitational field. The movement of larger bodies is guided by gravity, for example a satellite orbiting a planet. The satellite can measure the acceleration that is caused by the Martian gravity field. That acceleration is not always the same, irregularities in Mars' topography, mass distribution and overall shape could cause irregular attractive forces on the satellite. The gravity field is proportional to r^{-2}, whereas the gravitational potential is proportional to r^{-1}, where r is the radial distance between the measurement point (satellite) and the matter. Consequently, the field is less sensitive to masses that are positioned deeper (larger r) in the Martian mantle compared to the potential. Since the primary interest of this study is in the deep mantle of Mars, the gravitational potential has been used in this research. The gravity potential can be expressed as a sum of the spherical harmonic functions (Root et al., 2016):

$$V(r,\theta,\phi) = \frac{GM}{R}\sum_{n=0}^{\infty}\sum_{m=0}^{n}\left(\frac{R}{r}\right)^{n+1} V_{nm}Y_{nm}(\theta,\phi) \tag{2.1}$$

R is the reference radius, G is the gravitational constant and M is the mass of Mars. Furthermore, n is the spherical harmonic degree and m is the order. $Y_{nm}(\theta,\phi)$ are the surface spherical harmonic functions given by:

$$Y_{nm}(\theta,\phi) = \begin{cases} (-1)^m\sqrt{(2)}\sqrt{(\frac{(2n+1)}{4\pi}\frac{(n-|m|)!}{(n+|m|)!})}P_n^{|m|}(cos(\theta))sin(|m|\phi) & \text{, if m} < 0 \\ \sqrt{(\frac{(2n+1)}{4\pi})}P_n^m(cos(\theta)) & \text{, if m} = 0 \\ (-1)^m\sqrt{(2)}\sqrt{(\frac{(2n+1)}{4\pi}\frac{(n-m)!}{(n+m)!})}P_n^m(cos(\theta))cos(m\phi) & \text{, if m} > 0 \end{cases} \tag{2.2}$$

The Stokes coefficients V_{nm} are derived from C_{mm}, coming from the density and geometry of the modelled layer.

$$V_{nm} = \frac{3}{2n+1}\frac{1}{\rho_M}C_{nm} \tag{2.3}$$

Those coefficients are related to the interior mass distribution of Mars. The zeroth degree spherical harmonic is the mass of the planet, the first degree depends on the location of the centre of mass with respect to the

origin of the fixed reference frame of Mars. Since this study focused on variations in the gravitational potential, degree and order 0 and 1 were removed. Also the coefficient for the hydrostatic flattening of Mars (C_{20}) was removed for 95% unless indicated otherwise. There are a few analytical expressions that are being used throughout the research. They are listed below:

- Degree Variance: a tool that is used to determine the contributions of each of the spherical harmonic degrees. It gives an indication of how susceptible the gravity measurements are to which wavelengths.

$$DV = log_{10} \sum_{m=0}^{n} (C_{nm}^2 + S_{nm}^2) \tag{2.4}$$

  Where C_{nm} denotes the coefficients for the spherical harmonic terms with the order equal or larger than 0 (the cosine terms in the expression for $Y_n m(\theta,\phi)$ (Equation 2.2) and the S_{nm} terms the coefficients with an order smaller than 0 (the sine terms in the expression).

- Root Mean Square (RMS) Power per degree n (Goossens et al., 2020):

$$\sigma(n) = \sqrt{\sum_{m=0}^{m=n} (C_{nm}^2 + S_{nm}^2)} \tag{2.5}$$

- An equation to determine the Areoid-to-Topography Ratio (ATR) (Geoid-to-topography in Wieczorek and Zuber (2004)) for the case of Airy compensation;

$$ATR = \frac{N}{h} = \frac{2\pi\rho_c R^2}{M} H_0 \tag{2.6}$$

  Where N the areoid height, h the topography height, ρ_c the crustal density, H_0 the crustal thickness at zero elevation and R and M the radius and mass.

- The equivalent wavelength λ is the wavelength of the spherical harmonic degree n on a sphere of radius R. It is calculated with the Jeans relation (Wieczorek and Simons, 2005):

$$\lambda = \frac{2\pi R}{n(n+1)} \tag{2.7}$$

The gravity power spectrum of Mars is presented in Figure 2.1. In addition, the spatial resolution (half-equivalent wavelength $\lambda/2$) corresponding to the spherical harmonic degree. is presented in this figure. The terms long-wavelength (referring to the Jeans equivalent wavelength from Equation 2.7) and low degree (referring to spherical harmonics) have been used interchangeably throughout this research.

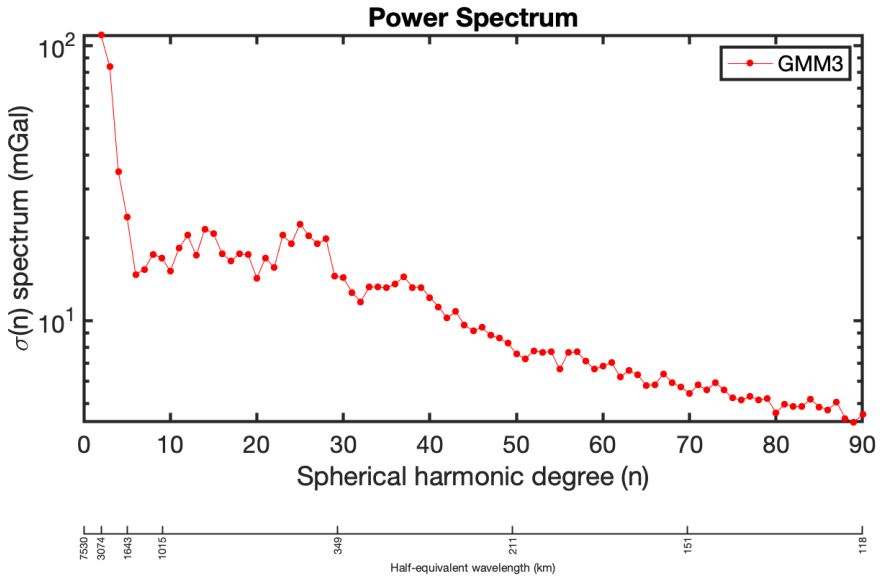

Figure 2.1: Power spectrum of the GMM-3 gravity. Data source: Genova et al. (2016).

Although the spectrum in Figure 2.1 only shows the gravity power spectrum, it was also used to express the gravity field due to topography later in this study. The gravity data that was used is a spherical harmonic set (GMM-3) up to degree 120. The areoid is the surface of points where the potential (centrifugal and gravitational combined) is equal, it is equivalent to the geoid in Earth studies. A representation of the areoid is shown in Figure 2.2, the hydrostatic flattening effect (C_{20} term) of the planet is visible in Figure 2.2b. In Figure 2.2a, the hydrostatic flattening was removed by keeping only 5% of the original C_{20} term (Zhong and Roberts, 2003).

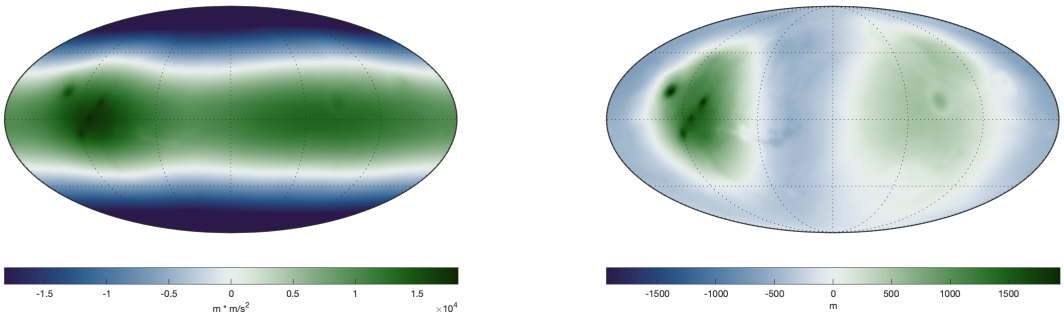

(a) Observed gravitational potential in Spherical Harmonics (SH) degrees 2-90.

(b) Observed areoid in SH degrees 2-90 with respect to the reference ellipsoid, hydrostatic flattening (95% of C_{20}) was removed.

Figure 2.2: Observed areoid in SH degrees 2-90 with respect to the reference ellipsoid. Both images are in Mollweide projection with a central meridian of 0 ° longitude. Data source: Genova et al. (2016).

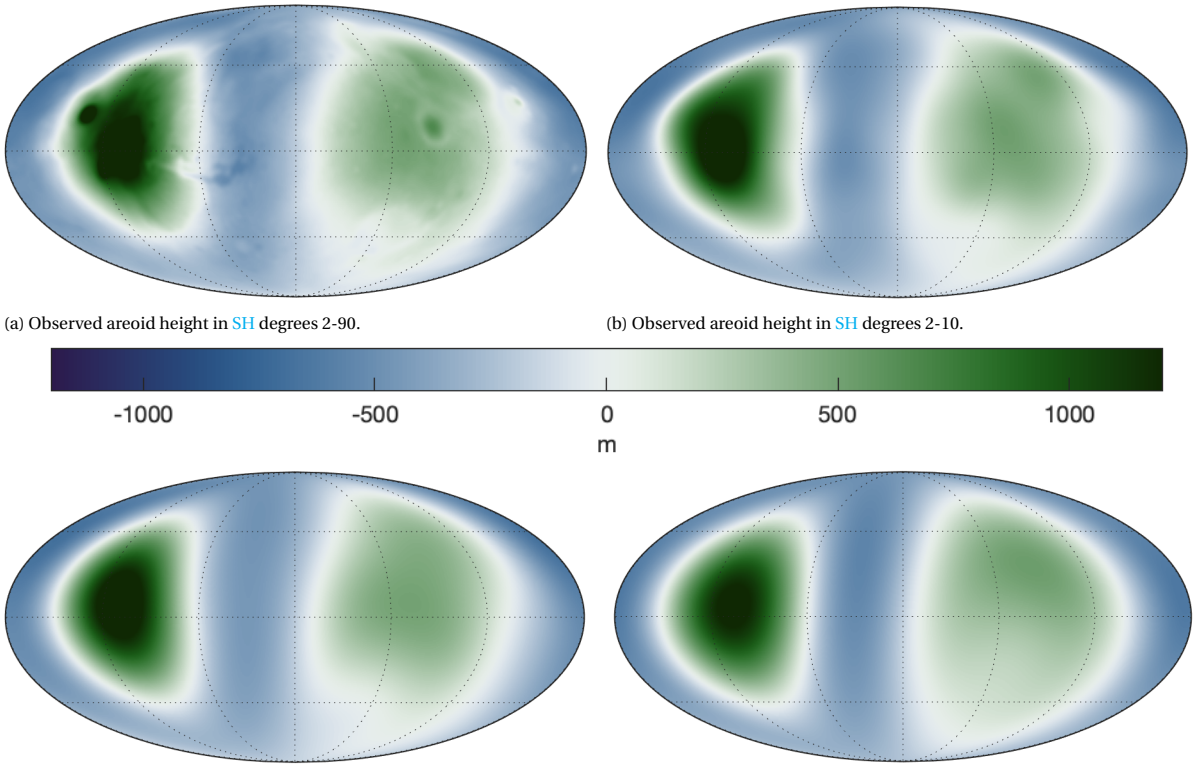

(a) Observed areoid height in SH degrees 2-90.

(b) Observed areoid height in SH degrees 2-10.

(c) Observed areoid height in SH degrees 2-5.

(d) Observed areoid height in SH degrees 2-3.

Figure 2.3: Observed areoid for varying SH degree limits (90, 10, 5 and 3), the hydrostatic flattening effect (95% of C_{20}) has been removed. The colorbar has been clipped at -1200 and 1200 m. All images are in Mollweide projection with a central meridian of 0 ° longitude. Data source: Genova et al. (2016).

A feature that is worth accentuating is the areoid high (the dark green region) at the equator at 110 ° W, which is located at the Tharsis region. Such an areoid high can be caused by several phenomena such as; a region with a higher density material, mantle density anomalies or upward deflection of the CMB. This region with a positive gravity field (areoid high) is encircled by a region with an areoid low, called the "Tharsis trough" (Wieczorek and Zuber, 2004; Phillips et al., 2001). At approximately 180 degrees longitude from Tharsis there is an antipodal positive gravity field, whether this is due to Tharsis or another mass anomaly is still unknown. There are many possible explanations for such an observation. This study investigated whether the areoid high at Tharsis could be a result of mantle anomalies as well as what impact this would have on mantle convection, volcanism on Tharsis and the structure and features of these deep mantle anomalies.

Wieczorek (2007) deduced that the high gravity signals up to degree 5 are not completely due to topography, it could for example be a consequence of lithospheric loads in the Tharsis region as also mentioned by Phillips et al. (2001). In addition, Steinberger et al. (2010), stated that the gravity anomalies under the lithosphere mostly manifest themselves up to spherical harmonic degree $n = 5$ for Mars. However, it cannot be derived if those density anomalies were caused by mantle structures with a density anomaly, or by phenomena such as for example upward deflection of the core-mantle boundaries. For higher degrees, the gravity anomalies of the upper layers (such as the lithosphere) became more dominant. Although the gravity effect of the upper layers is not dominant at low spherical harmonic degrees, the contribution of the crust was eliminated as much as possible from the total gravity field. Under the assumption that this crustal reduction is accurate, the gravity field solely due to the deeper layers in the planet was obtained.

2.2. CRUSTAL REDUCTION

This section focuses on the creation of a model that is representative of the Martian crust. With this model, the gravity field contributions of the crust were calculated. By subtracting this from the observed gravity field, the information of the mantle and below remains. At first, the Bouguer Anomaly was researched, after which the role of local isostasy was taken into account. The verification and validation of the observation data and crustal models is documented in Chapter 3.

2.2.1. BOUGUER ANOMALY

The effect of the mass between the reference level and the gravity field instrument can be taken into account. This gives a more realistic representation of the sub-surface gravity field since there are a lot of topographic variations on the Martian surface, which influence the gravity field. The lower regions are gravitationally attracted by high topographic features such as mountains. The Bouguer correction is due to the gravitational attraction of the terrain.

The Bouguer anomaly (which is the observed gravity field minus the Bouguer correction), comes in two versions: the simple or refined Bouguer reduction. For the simple Bouguer correction, one calculates:

$$g_B = g_F - \delta g_B \tag{2.8}$$

Where g_B is the Bouguer anomaly and g_F the free air reduction. The Bouguer gravity correction δg_B is calculated by Equation 2.9.

$$\delta g_B = 2\pi G \rho H \tag{2.9}$$

The definition comes from the infinite plate assumption; the magnitude of the gravitational acceleration above a plate with thickness H is the mass per unit area times $2\pi G$ with G the gravitational constant.

For the refined Bouguer anomaly, another term is added:

$$g_B = g_F - \delta g_B + \delta g_T \tag{2.10}$$

Instead of assuming an infinite plate, the gravity anomaly due to an uneven terrain topography is also subtracted from the observed free-air gravity. The Bouguer correction is useful for this research since it takes away the topographical aspect in the gravity data, resulting in gravity anomalies unrelated to topography (Backer, 2018; Fowler, 2004). In order for this to be truly correct, the topography is assumed to have a homogeneous density. The Martian topography is visualized in Figure 2.4.

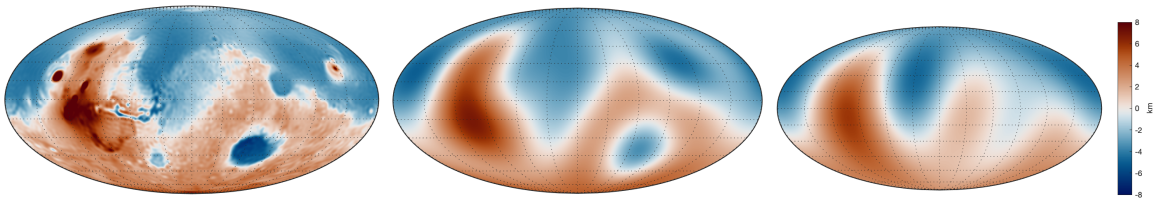

Figure 2.4: Observed topography with SH degrees 1-90, 1-5 and 1-3 respectively. All images are in Mollweide projection with a central meridian of 0 ° longitude. The colorbar has been clipped at -8 and 8 km. Data source: Smith (2003)

With the topography, the simple and refined Bouguer correction are calculated. Note that the R-component of the gravity field vector is used in the determination of the Bouguer anomaly since the gravity field has a higher sensitivity to the upper layers (topography) than the gravitational potential. The units that are used to express the gravity field vector are mGal [1]. In order to determine whether the refined correction significantly deviates from the simple Bouguer correction, a comparison is presented in Figure 2.5.

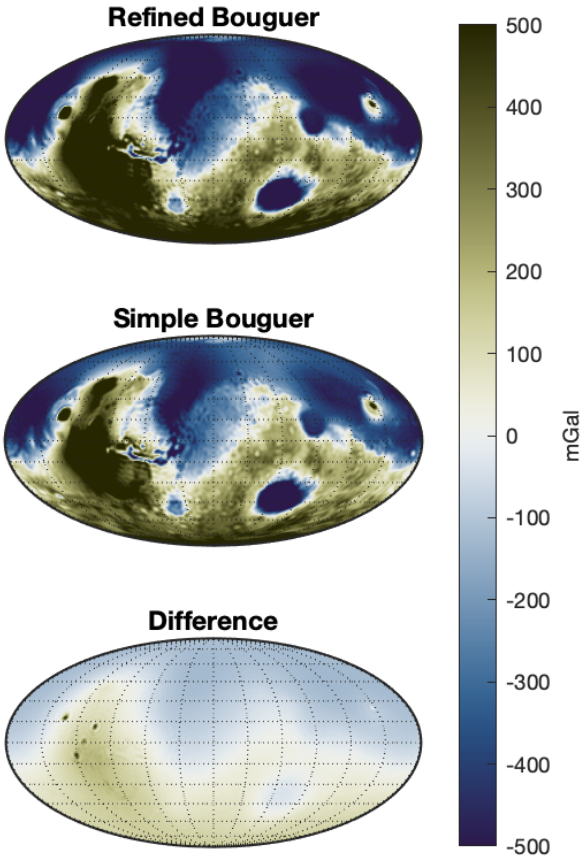

Figure 2.5: Top: refined bouguer correction. Middle: simple bouguer correction. Bottom: difference (refined-simple). Axis are clipped from -500 to 500 mGal. Both models assumed an average crust density of 2900 kg/m^3. All images are in Mollweide projection with a central meridian of 0 ° longitude.

Figure 2.5 illustrates that the refined Bouguer correction is similar to the simple Bouguer correction. Differences are visible at the Tharsis volcanoes because the unevenness of the terrain is relatively large at those locations, so the infinite plate approximation is less accurate here. Moreover, the southern hemisphere has regions where the refined correction is slightly higher because the refined correction takes into account the

[1] 1 Gal = 1 cm / s^2

unevenness of the terrain. Henceforward, the refined Bouguer anomaly is used. The remaining gravity field is presented in Figure 2.6.

Figure 2.6a shows the Bouguer anomaly for a crustal density of 2900 kg/m^3. As can be seen, the gravity anomaly that is caused by the topography (Bouguer correction) is high at locations of high elevation, as expected. Therefore, the crustal dichotomy is clearly distinguishable in the bouguer correction of Figure 2.6a. Since the observed gravity field has no clear crustal dichotomy and the Bouguer correction of this feature is large compared to the observed field, it is also clearly observable in the Bouguer anomaly. The bouguer correction is successful in removing the effect of the topography, but it does not result in a good approximation of the gravity field of the deeper layers. Since the crustal dichotomy is very dominant in the Bouguer anomaly, Figure 2.6b represents the anomaly once the crustal dichotomy (degree 1) has been removed. There are still regions with a high bouguer anomaly, meaning that the observed gravity field at those regions is not purely caused by topography and therefore there should be other processes at play. Something that was disregarded in the determination of the Bouguer anomaly is isostasy. This is the phenomenon of a gravitational equilibrium of a mass in a fluid. For isostatic models, the effect of the topography on layers below is also taken into account.

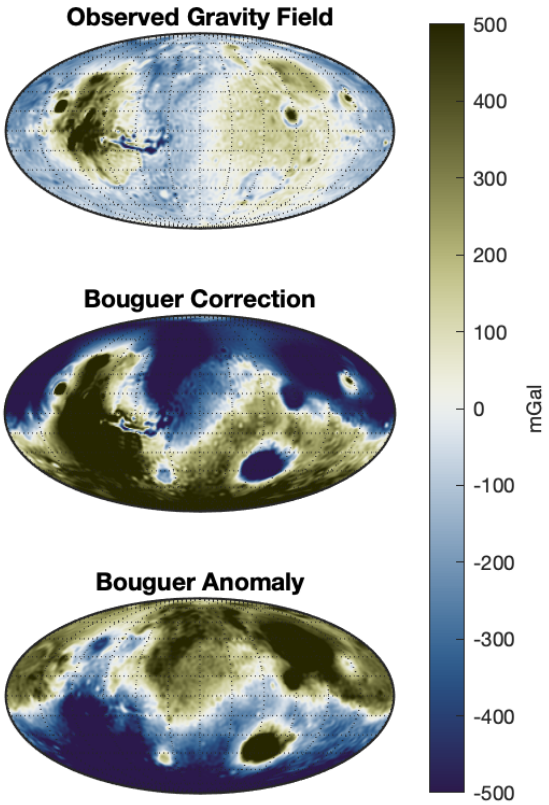

(a) Bouguer anomaly without removal of the crustal dichotomy.

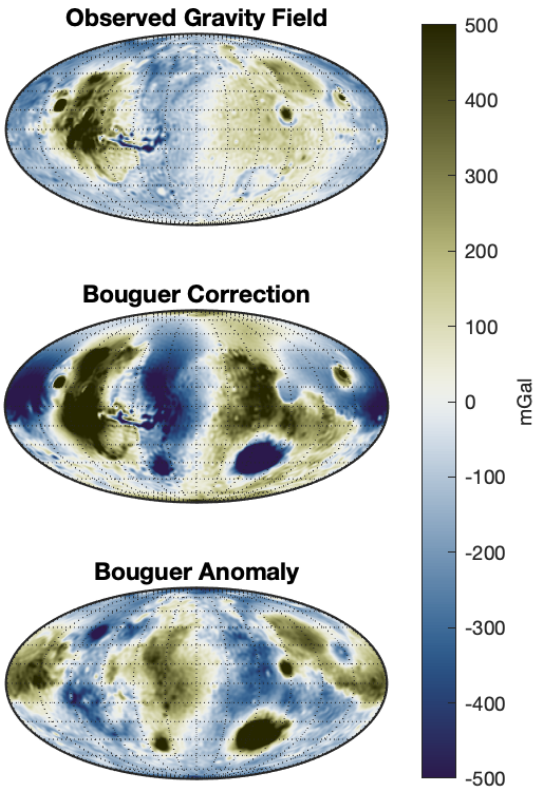

(b) Bouguer anomaly with removal of the crustal dichotomy.

Figure 2.6: Bouguer anomaly. The axis are clipped from -500 to 500 mGal and an average crustal density of 2900 kg/m^3 was assumed. All images are in Mollweide projection with a central meridian of 0 ° longitude.

2.2.2. AIRY ISOSTASY

There are many options in the creation of an isostatic model, two of the most used cases are Airy and Pratt isostasy. A study by Mussini (2020) showed that in the long-wavelength regime, which is the focus of this research, Airy isostasy is the dominant form of compensation. Additionally, flexural response functions show a large close to one, indicating an Airy response instead of a flexural or Bouguer response (Mussini, 2020; Watts, 2001). Therefore, an Airy model was developed to estimate the gravity contribution of the upper layers.

Isostasy makes use of the equilibrium of a mass. An example is given by a floating iceberg where a gravitational equilibrium is present of the iceberg floating in the water. To reach this equilibrium, a significantly

larger part of the iceberg is below the water surface. The part below the water surface is called the root. Likewise for the Martian planet, where the crust rests on the layers below (or the lithosphere on the astenosphere). The heavier the crust the larger the root, the reverse is also true. This concept is called buoyancy, the crust 'floats' on the mantle. The mantle can in this case be seen as a fluid, with a very high viscosity. Over long timescales, such a gravitational equilibrium can be reached.

The model is developed by Sir George Biddell Airy and later refined by Veikko Aleksanteri Heiskanen. It takes into account topographic heights by changing the thickness of the crust below. If the topography is high, its compensation requires a thicker crust (meaning that the crust reaches deeper into the mantle on that location). Lower topographies are compensated by a thinner crust, meaning that the mantle is thicker in that area. The Airy model is based on Pascal's Law: the hydrostatic pressure is constant for a specific elevation.

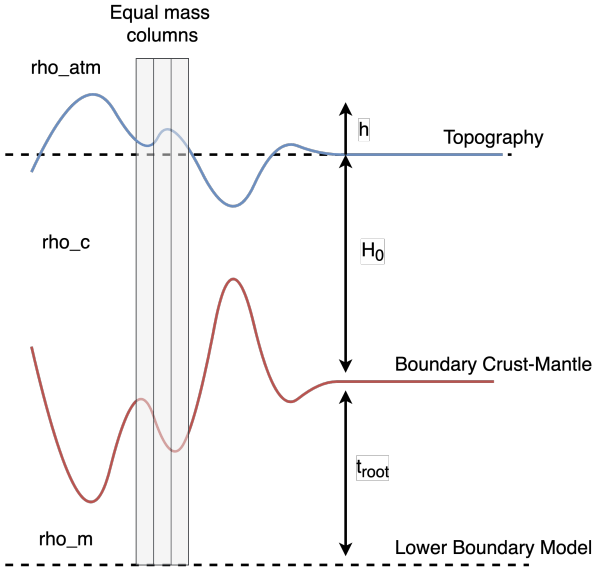

Figure 2.7: Airy model, topography with height h is isostatically compensated by a crustal root t_{root} into the mantle, this crustal root has a lower density than the surrounding mantle material $\rho_c < \rho_m$. h denotes the elevation of the topography with respect to the areoid.

Figure 2.7 shows the Airy model with the required parameters for a calculation to determine the column heights. According to Pascal's law, the hydrostatic pressure a certain depth should be the constant at all locations. The columns indicate columns of similar width and mass, meaning that the same hydrostatic pressure is applied on the lower boundary. With this information, the crustal thickness (excluding topographic variations) is determined by:

$$t_c = H_0 + \frac{h * \rho_c}{\rho_m - \rho_c} \tag{2.11}$$

The boundaries and densities of the topography and the crust, together with crustal thickness at a topography elevation of zero: H_0, are the required information to calculate the corresponding gravity field. These calculations were performed by the Global Spherical Harmonic (GSH) code Root et al. (2016). In the case of Airy isostasy, a constant crustal density and constant mantle density are assumed. Besides the topography (and crustal root) variations, no other anomalies were present that could cause gravity anomalies. The Global Spherical Harmonic Analysis (GSHA) code analyses the planet layer by layer, converting each layer into a set of spherical harmonic coefficients which were subsequently added together to retrieve the spherical harmonic representation in C_{nm} and S_{nm} coefficients. This set of spherical harmonics was translated by the Global Spherical Harmonic Synthesis (GSHS) to calculate the grids of the gravity vectors, gravitational potential and tensor fields. A schematic visualization is presented in Figure 2.8.

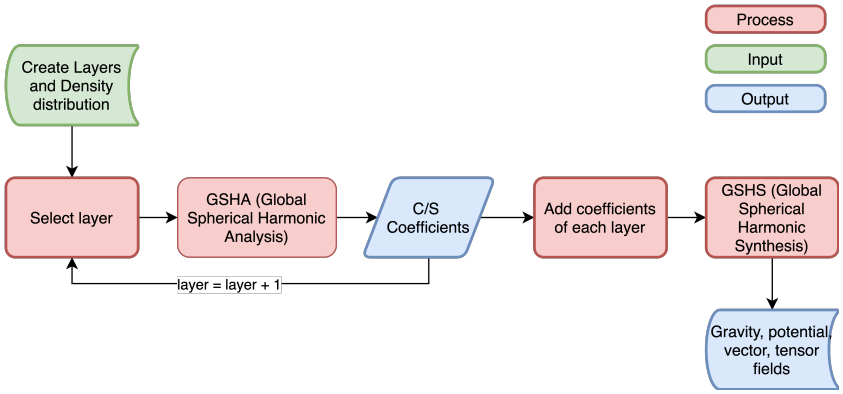

Figure 2.8: Flowchart of the Global Spherical Harmonic Analysis (Root et al., 2016).

Since the topography (elevation h) is an observation, the three parameters that were varied are the compensation depth H_0, the crustal density ρ_c and the mantle density ρ_m. The results of this study are presented in Chapter 4, Section 4.1. It was determined that the crustal density should be approximately 2900 kg/m^3 and a mantle density of 3550 kg/m^3. A zero-elevation crustal thickness of approximately 100 km results was assumed. These values are also within the limits of other research (e.g. (Backer, 2018; Wieczorek, 2015; Neumann et al., 2004)).

A crustal model was created with those parameters and was subtracted from the observed gravity field.

$$g_{mantle} = g_{observation} - g_{crust,Airy} \tag{2.12}$$

Where $g_{observation}$ is the observed gravity field, $g_{crust,Airy}$ is the gravity field due to the Airy compensated topography and g_{mantle} is the gravity field due to the mantle. Assuming that the crustal model is an acceptable representation of the crust, it is save to state that the remainder of the gravity field is caused by density anomalies in the deeper layers (below the lithosphere). Figures 4.4 and 4.5 present these remaining gravity field and gravitational potential fields that were used as 'observation' henceforward.

Since the source of the remainder is in the deeper layers of the planet, the gravitational potential field was used because it is more susceptible to variations in deeper layers. It is evident that the crustal reduction did not succeed in eliminating all variations in the gravity field, those variations are due to mantle anomalies or boundary variations of (e.g. Core-Mantle Boundary undulations), each having its own topography and deformations and therefore a contribution to the gravity field. Figure 4.5 is visualized in Figure 2.9, in order to define terminology that was used throughout this study.

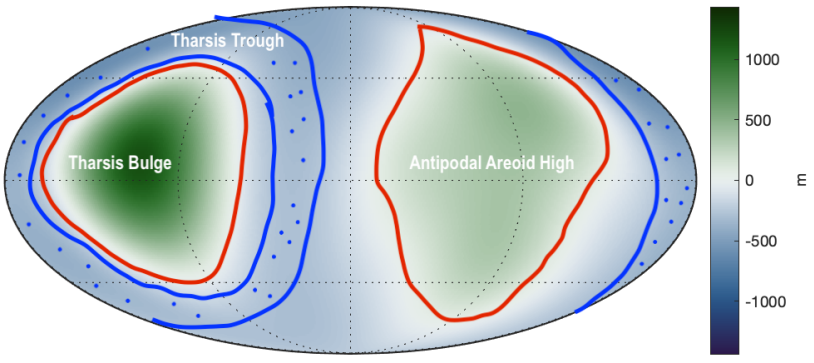

Figure 2.9: Remaining areoid after crustal reduction of an Airy compensated crust with a zero-elevation crustal thickness of 100 km, a crustal density of 2900 kg/m^3 and a mantle density of 3550 kg/m^3. The image is in Mollweide projection with a central meridian of 0 ° longitude. The lower limit of the colorbar is manually set to the negative of the maximum observed areoid. Spherical harmonic degrees 2-5. C_{20} is removed for 95%.

The remaining areoid of Figure 2.9 shows several large, distinguishable features; the Tharsis bulge and

trough, as well as the positive areoid at the antipodal of Tharsis. Those features are expected to be caused by large regions in the mantle with a density or temperature anomaly.

In all models researched in this study, density anomalies were positioned in the Martian mantle, the areoid caused by those density anomalies was compared to the observed mantle areoid of Figure 2.9. Section 2.3 elaborates upon the creation and assessment of the density anomalies.

2.3. DENSITY ANOMALIES IN THE MANTLE

After subtracting the crustal model from the total areoid, the residual can be assumed to be complete caused by the mantle and CMB. In order to determine what kind of mantle anomalies are able to create a gravity field similar to that of the observations, a code was written. It places anomalies in the mantle, calculates their gravity field, and determines the best-fitting solutions with a search-algorithm. Furthermore, a sensitivity study was performed to identify which variables are robust modelling and which are not.

A density anomaly was created by defining a region inside the mantle where the density is different from the surrounding mantle density. This region is indicated by the following variables;

- Radially: a depth D_a (in km) at which the anomaly starts (and is continued downwards) and a thickness T_a (in km).
- Laterally: a center of anomaly C_a ([lon degree, lat degree]) and the latitude range S_{lat} ([lat up, lat down]) and longitude range S_{lon} ([lon left, lat right]) with respect to this center. For a clarification, the reader is referred to Figure 2.10.
- The density anomaly $\Delta\rho$ (in kg/m^3), the density of the anomaly was assumed to be homogeneous, so no density gradient was applied.

A schematic overview of these parameters is presented in Figure 2.10.

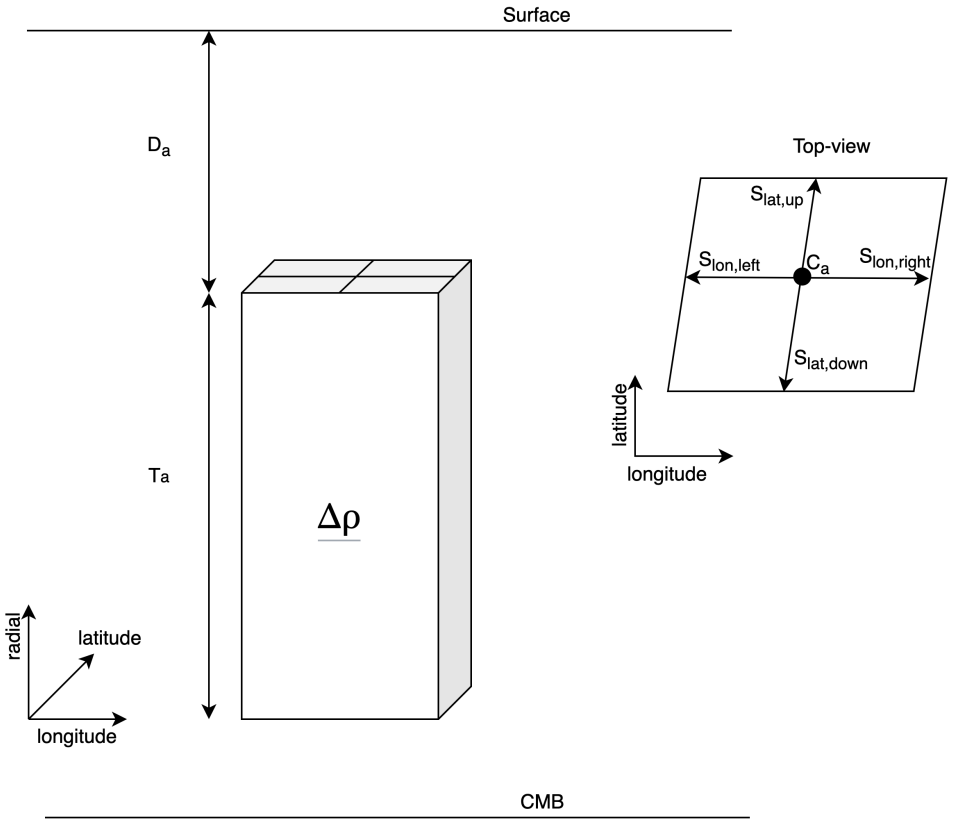

Figure 2.10: Visualization of the density anomaly variables. The distances in the figure are not on scale.

With this information, the density anomaly was created and the resulting gravity field was modelled. The modelled gravity field is only dependent on the anomalies in the mantle as the gravity of the crust was already subtracted from the observations to obtain g_{mantle}. In Section 2.4, other components are added to the computation.

$$g_{model} = g_{anomalies} \tag{2.13}$$

The aim was to create a modelled gravity field g_{model} close to the observed gravity field of the mantle (g_{mantle}). Since there are six (D_a, T_a, C_a , S_{lat} , S_{lon} and $\Delta\rho$) variables, it was necessary to put constraints on them to limit the search space. Firstly, the location of the density anomaly was assumed to be located on the gravitational bulge peak that is observed in the Tharsis region, at: $C_a = [110°W, 3°N]$. Secondly, the anomaly was assumed to be a rectangle (in a latitude/longitude grid projection) to limit the S_{lat} and S_{lon} search space. Moreover, the thickness T_a was assumed to be at least 100 km (the LLSVPs on Earth are expected to be continuous piles not extending higher than 200-300 km above the core (Davaille and Romanowicz, 2020)). Since one of the goals of this research was to test to hypothesis of structures similar to LLSVPs being in the Martian mantle, the initial depth D_a of the anomaly was set at 1000 km, this means that it is within 700 km from the CMB which is at a depth of approximately 1700 km. So the search-algorithm starts modelling around these depths, but if no solutions were found, it was able to move to shallower depths. Three types of models were tested:

1. (DA-S): Density Anomaly - Symmetric with respect to the center ($S_{lon,left} = S_{lon,right}$)
2. (DA-A): Density Anomaly - Asymmetric (skewed to one side) with respect to the center, the left and right longitude were inserted separately. The difference with a DA-S is that, seen from the center point C_a, the left longitude boundary of the anomaly can be further away than the right longitude boundary ($S_{lon,left} != S_{lon,right}$)
3. (DA-CMB): Density Anomaly - CMB imitating variations in the Core Mantle Boundary, this model is characterized by an assumed depth (at CMB) and density (ρ_{core}), thickness of the anomaly that fits the observations is determined, this would be the CMB variation that is required to cause the observed gravity field.

2.3.1. SINGLE LATITUDE MODEL ASSESSMENT

In order to assess whether a modelled gravitational potential field fits the observations, four fitting parameters were established (visualized in Figure 2.11);

1. MaxPeak- Highest gravity field value (MP): Highest gravity field value
2. Peakzero: Longitude distance (in degrees) from MP to the first zero-gravity line
3. Zerozero: Longitude distance (in degrees) from the first zero-potential line from MP to the second zero-potential line
4. Peakratio: Ratio of MP and second maximum peak (often at the antipodal)

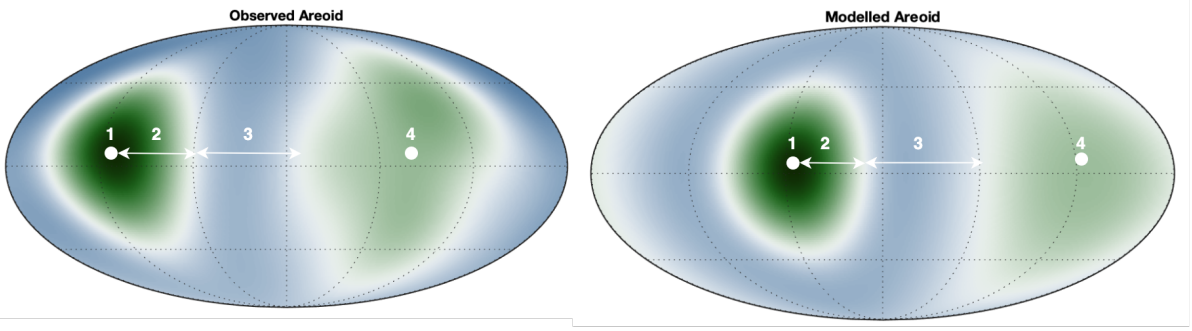

Figure 2.11: Schematic representation of the gravity field parameters used for the sensitivity studies. Left: observed gravity field and identified key values to describe the field. Right: locations of the parameters in a modelled gravity field.

A sensitivity study was performed to determine the hierarchy in which parameters influence the gravity field, the results are shown in Section 4.2.1. On the basis of those results, a search-code has been written that models density anomalies and assesses the resulting gravity fields. The code first estimates the parameters

that are associated with a low robustness. Ultimately, good-fitting results were determined for each assumed density anomaly $\Delta\rho$, a flowchart of the code is depicted in Figure 2.12.

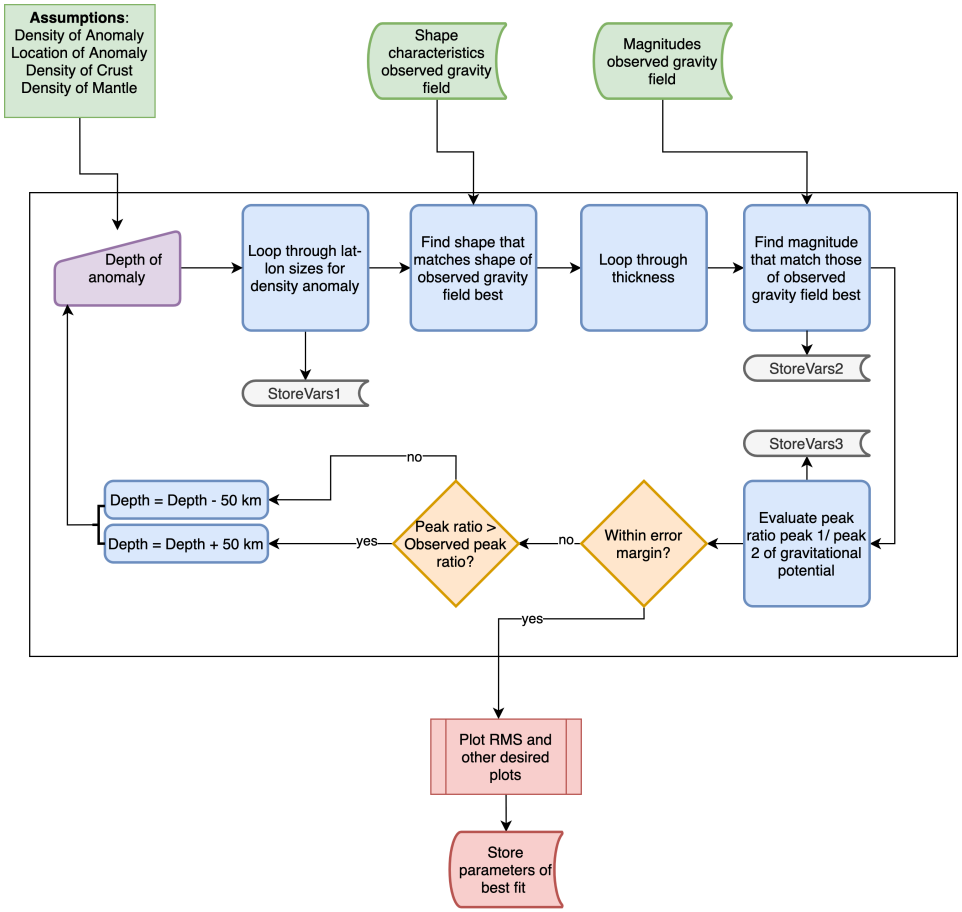

Figure 2.12: Flow Diagram of the Search-Code. Assuming a certain density anomaly, the code finds solutions that best fit the observations considering the four criteria established above.

The search spaces and step sizes that were considered depend on the model. For a symmetric density anomaly (DA-S Model) and the asymmetric density anomaly (DA-A Model), the considered density anomalies were $\Delta\rho = 20, 50, 100, 200, 400$ and 800 kg/m^3. Negative density anomalies do not lead to a positive gravity field anomaly when neglecting mantle convection, so negative anomalies were disregarded in these models. The DA-CMB model puts a density anomaly on the CMB that has exactly the same density contrast as that of the mantle and the core. In this way, the density anomaly can be modelled as a variation in the CMB-topography. In total, two different core radii have been assumed: 1) a radius of 1700 km and a corresponding core density of 7000 kg/m^3 and 2) a radius of 1400 km and a core density of 8500 kg/m^3. Those densities were derived from radial profiles created by Steinberger et al. (2010).

For the DA-S and DA-A models, an initial depth of 1000 km was considered, but the allowed search space was set at a range from 200 km depth down to approximately 1700 km (the core radius) with a step size of 50 km. The thickness of the density anomaly starts at a minimum of 100 km, and was increased in steps of 50 km. On Earth, the estimated thickness of LLSVPs was in the order of 300 km (Trønnes, 2010). Since the radius of Mars is approximately twice as small as that of Earth, it could be reasonable to expect that the LLSVPs in Mars would be smaller than 300 km. The DA-CMB models assumed a depth such that the bottom of the anomaly with a thickness T_a was exactly on the core-mantle boundary. The thickness was varied in steps of 10 km in order to determine how large the CMB variations should be to create a model fitting well to g_mantle.

For the DA-S model, the longitude and latitude sizes (in degrees) of the density anomaly S_{lon} and S_{lat} are symmetric with respect to the center of anomaly. For example, an assumed $S_{lon} = 10$ deg means that the den-

sity anomaly extents to 10 degrees left to 10 degrees right from the center (so from 60 degrees to 80 degrees longitude). The step size for both longitude and latitude is 2 degrees. For the DA-A model, $S_{lon,left}$ can be different from $S_{lon,right}$, the same is true for $S_{lat,up}$ and $S_{lat,down}$. A step size of 2 degrees is taken in for both parameters. In the DA-CMB models, the best-fitting size of a density anomaly close to the CMB was used as configuration, no optimization for size was performed in this model, only for thickness. For all three models, an anomaly center of $C_a = [110^\circ W, 3^\circ N]$ is assumed, since the peak of the Tharsis bulge is at that location.

For each model, the best-fitting solutions were determined for the specified configuration. The was done by the search-code in combination with a calculation of the Root Mean Square Error (RMSE) of the model with respect to the observed values:

$$RMSE = \sqrt{\frac{\sum_{i=1}^{N}(Obs_i - Mod_i)^2}{N}} \tag{2.14}$$

Where i indicates the data-points (pixel in grid). For instance, Obs_3 indicates data-point 3 in the observation data. Likewise, Mod_3 indicates data-point 3 in the model. The results of models DA-S, DA-A and DA-CMB are presented respectively in Sections 4.2.2, 4.2.3 and 4.2.4. Although the DA-models introduced above give a good first order impression of the effect of placing a density anomaly in the mantle, it is not representative of the physical world. This is because the stresses created by those anomalies were not taken into account. For instance, it could be that the resulting (dynamic) topography deformation is too high and is not realistic. Therefore, the observed topography can be taken as an additional constraint on the dynamic topography deformation to constraint the model outcomes even more. In the next section, the stresses and their effect on the gravity field are integrated in the models.

2.4. BOUNDARY DEFORMATIONS

The results of models DA-S and DA-A demonstrated the possibility of a positive density anomaly beneath Tharsis. The gravitational field fitted very well by placing a single density anomaly under the Tharsis region. However, the density contrast of the anomaly was geophysically unlikely. In reality, a density anomaly is inclined to move upwards if it is lighter than its surrounding and downwards if it is heavier. This in turn puts stresses (forces) on the boundary surfaces such as the topography and CMB. As a result of those stresses, the surfaces deform and those deformations affect the observed gravitational field. This phenomenon was taken into account in the models presented in this section. The effect can be explained with the visualization represented in Figure 2.13.

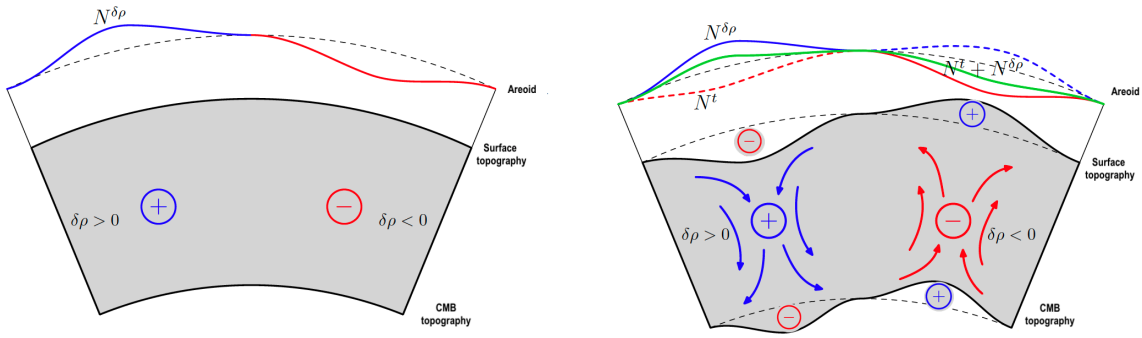

(a) A static positive (negative) density anomaly $\Delta\rho$ causes a positive (negative) areoid anomaly $N^{\Delta\rho}$

(b) Boundary deformations as a result of a convecting mantle (stresses), the boundary variations have to be taken into account in the calculation of the gravity field. A positive density anomaly $\Delta\rho$ could result in a negative areoid anomaly $N^{\Delta\rho}$.

Figure 2.13: Visualization of the difference in approach. a) represents the initial approach for models DA-S, DA-A and DA-CMB. b) calculates the stresses and boundary deformations as a result of the presence of a density anomaly. Those topography variations have a positive (blue circle with a plus) or negative (red circle with a minus) effect on the observed areoid. Inspired by Tosi (2007).

The implementation of this approach, the calculation of boundary deformations, is expected to change the best-fitting results. For instance, a possible outcome is that a negative density anomaly causes a positive

areoid anomaly, something that was impossible in the DA Models. This is because of the buoyant nature of negative density anomalies, pushing the surface topography upwards and also causing an upwards deflection of the CMB. These changed boundaries have a counteracting effect on the gravity that is purely due to the anomaly itself (static gravity) .

In order to solve the Stokes-Poisson problem, the Spectral Finite Elements Convection (SFEC) (SFEC) approach was used (Tosi, 2007). SFEC solves the Stokes equations for a spherical shell with 3D density and a 1D-radial viscosity profile. It calculates the stresses at the boundaries of the layers defined in the model, those stresses are being used to compute the dynamic surface topography and the dynamic CMB variations, these topographies influence the total gravity field. The resulting gravity is calculated with:

$$g_{model} = g_{anomalies} + g_{dyn,topo} + g_{dyn,CMB} \tag{2.15}$$

Where g_{model} is the total modelled gravity field, consisting of the gravity of the anomalies ($g_{anomalies}$) and the gravity of the dynamic boundary of the surface ($g_{dyn,topo}$) and CMB ($g_{dyn,CMB}$). Similar to Section 2.3, the closer the modelled gravity field g_{model} is to the observed g_{mantle}, the better. The assumption of an incompressible fluid was made. This assumption is a valid approximation of reality since hydrodynamic stresses are significantly smaller compared to hydrostatic pressure changes (Tosi, 2007). In order to model a mantle convection flow, the situation has to be solved for conservation of mass, conservation of linear momentum and the Poisson equation. Another assumption of the flow is that it can be modeled as a linear viscous rheology, so no (Maxwell) viscoelastic forces were taken into account. This assumptions was done by previously conducted studies as well and was proven to be successful (Tosi, 2007).

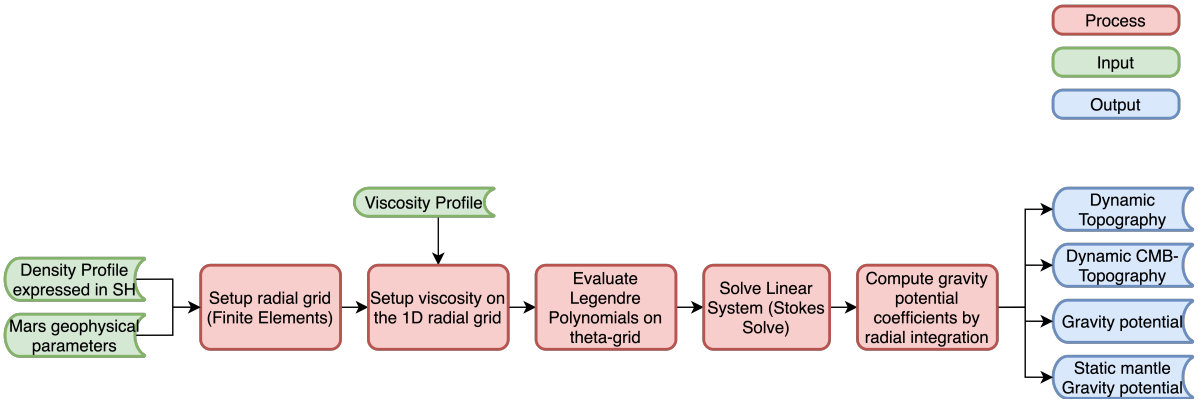

Figure 2.14: SFEC schematic overview.

Figure 2.14 visualizes the inputs, process and output of SFEC. Firstly, SFEC requires the geophysical parameters of the relevant planet. It also requires a density distribution per layer, expressed in spherical harmonic coefficients and a viscosity profile. These inputs are discussed in more detail in Section 2.4.1.

Each layer is divided in N nodes, creating a radial grid. The lateral variations are described by spherical harmonics. On this Gaussian longitude latitude grid the Legendre polynomials are evaluated, consequently the Stokes equation can be solved for and the gravity potential can be computed by radial integration. The output contains spherical harmonic coefficients for the dynamic surface topography, dynamic CMB topography, gravitational potential and a static mantle gravity potential (only taking into account the mass distribution, without any deformed topographies).

2.4.1. MODELLING THE INTERIOR LAYERS

The available SFEC code and its parameters were appropriate for Earth studies, but not for other planets. By changing the input parameters from Earth to Mars, it was possible to perform mantle convection studies in Mars (or any other arbitrary spherical planet). The constants (listed in the file modules.f90) that were changed are depicted in Table 2.1. Moreover, a customized layering structure was applied: assuming a core radius of 1597 km, a lithosphere of 100 km and an equatorial radius of 3397 km, there is 1700 km of mantle. This region has been split up in 17 layers, of each 100 km thickness. It was assumed that a density anomaly

has a thickness that is an integer multitude of 100 km, therefore precisely occupying one or more layers. Note that the density anomaly has limits in the lateral directions.

A tomography file containing the SH coefficients of the density distribution of each of the layers is required as input for the convection model. Since there is no tomographic data of the Martian interior, only a density anomaly was modelled. Assuming the remainder of the mantle is homogeneous is a large oversimplification but since little is known about Mars' mantle, a necessary one. The process of creating the tomography file is shown in Figure 2.15.

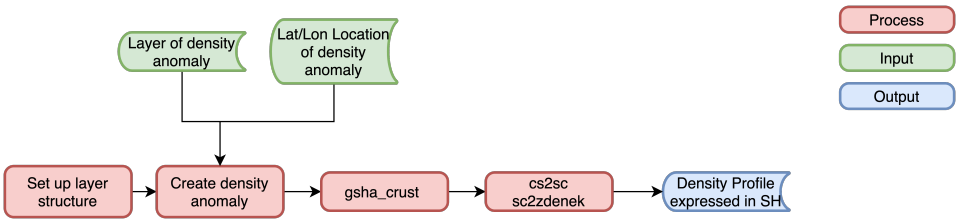

Figure 2.15: Schematic representation of the process generating a file containing density distributions of each of the layers.

As was depicted in Figure 2.14, the other requirement is a viscosity profile. The original SFEC code contained three viscosity layers: the lithosphere, upper mantle and lower mantle. The impact of the assumed viscosity profile on the resulting boundary deformations can be significant. Therefore, the code was adjusted, enabling the user to change the viscosity profile of each of the tomographic layers. Validation and verification of SFEC and the inputs can be found in Chapter 3.

Table 2.1: SFEC Parameters for Earth and Mars

	Earth	**Mars**
yr [10^7 sec]	3.1536	5.94
g_{ref} [m/s^2]	9.8	3.72
g_{cmb} [m/s^2]	10.68	3.21
ρ_0 [10^3 kg/m^3]	3.3	3.55
$\Delta\rho_t$ [10^3 kg/m^3]	3.3	2.9
$\Delta\rho_{core}$ [10^3 kg/m^3]	4.5	3.5
R [10^6 m]	6.371	3.397
R_{core} [10^6 m]	3.48	1.597
R_{mantle} [10^6 m]	5.7	3.297
R_{lith} [10^6 m]	6.271	3.297
$dvfac$	0.3	0.3

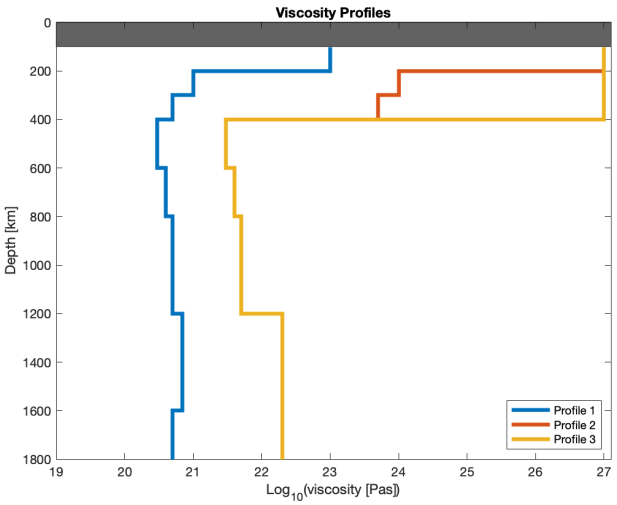

Figure 2.16: Radial viscosity profiles used in this study. Profile 1 (blue line) is a viscosity profile by Steinberger et al. (2010), Profile 2 (orange line) by Plesa et al. (2018) and Profile 3 is a modification of Profile 2 in which the upper layers are more viscous.

Three viscosity profiles were considered: one by Steinberger et al. (2010), one by Plesa et al. (2018) and the third one is a modification on the second, where the upper layers have a higher viscosity. The third viscosity profile was created to determine the effect of having an increased viscosity in the top layers, expecting less topography deformations. The radial profiles are visualized in Figure 2.16.

2.4.2. GRAVITY MODELLING

Using the gravity fields modelled by SFEC, two types of models were researched:

1. (BD-Grav-FULL): Boundary Deformations modelling gravity, $g_{model} = g_{anomalies} + g_{dyn,topo} + g_{dyn,CMB}$
2. (BD-Grav-SC): Boundary Deformations modelling gravity - Solid Core, assuming a solid core (no CMB topography deformations): $g_{model} = g_{anomalies} + g_{dyn,topo}$

For each configuration, a range of density anomalies (as a percentage of the surrounding mantle) and different depths (from 100 km downwards) were modelled. The baseline settings are indicated by the bold values in Table 2.2. Several sensitivity studies were performed with respect to the viscosity, spectral resolution (SH-degrees), lithosphere thickness and anomaly thickness. The results can be found in the section indicated in the third column of Table 2.2.

Table 2.2: The configuration settings in the modelling of BD-Grav-FULL and BD-Grav-SC. Column 1 presents the variable. The parameters that are varied with respect to the **baseline** (indicated in bold) are listed in column 2. Column 3 states in which section the results of the corresponding search space can be found.

SFEC	**Settings**	**Results**
Solid core	Yes (BD-Grav-SC) or **No** (BD-Grav-FULL)	Section 4.3.2 and 4.3.1
Viscosity Profile	Profile **1**, 2 or 3	Section 4.3.1
SH	2-3, 2-4, **2-5**	Section 4.3.1
Lithosphere thickness	50, **100**, 200 km	Section 4.3.1
Lithosphere density	2900 kg/m^3	Constant
Lithosphere viscosity η_{lith}	10^{30} Pa $\cdot$ s	Constant
Core radius	1597 km	Constant
C_{20}	95% removed	Always
Density Anomaly	**Settings**	**Results**
Thickness	**400**, 600, 800 km	Section 4.3.1
Longitude size	[46 to 94] deg	Constant
Latitude size	[-27 to 44] deg	Constant
Density range	[-10 to 0 %]	Always
Depth	100 km to 1400 km	Always

The modelling that was performed with these configurations used the modelled gravity field and compared it to the observed gravity field. However, the output of SFEC also contains the deformed surface topography boundary. This boundary is used in the calculation of the gravity field but whether the resulting boundary is realistic, was not taken into account. The dynamic surface topography can be used as an additional constraint on the models, as is discussed in the Section 2.4.3. A new method (Similarity) was proposed that is able to analyse and assess whether the modelled gravity field fits the observations. This method is introduced in Section 2.4.4.

2.4.3. HYBRID MODELLING

In the hybrid modelling, the dynamic topography (the result of the stresses caused by a density anomaly) was constrained by the observed topography. As was concluded by other research into the support under Tharsis (Zhong and Roberts, 2003), the topography is supported partially by buoyant forces (e.g. a plume). The remainder of the topography should be supported by a combination of isostatic compensation and flexural loading, the dominant contribution being the isostatic compensation (Mussini, 2020). The bottom loading by a buoyant mantle is assumed to be completely decoupled from Airy isostasy compensation. Accordingly, the topography that should be compensated by Airy isostasy is the remainder of the topography after subtracting the dynamic topography from the observed topography:

$$t_{Airy} = t_{Obs} - t_{Dyn} \tag{2.16}$$

The gravity ($g_{crust,Airy}$) due to the topography that is compensated by Airy isostasy was calculated in the same way as in Section 2.2.2, but now the t_{Airy} from Equation 2.16 is used as topography instead of t_Obs. SFEC calculates the gravity field due to the mantle anomalies and boundary deformations: $g_{model} = g_{anomalies} + g_{dyn,topo} + g_{dyn,CMB}$. In this way, both the Airy isostasy and the gravity of SFEC are taken into account;

$$g_{model} = g_{Airy} + g_{anomalies} + g_{dyn,topo} + g_{dyn,CMB} \tag{2.17}$$

This modelled field was subsequently compared with the complete observed gravity field ($g_{observation}$ from Equation 2.12) since the Airy crust was also modified. Two different kinds of models are investigated:

1. (BD-Hybrid-UC): Boundary Deformations Hybrid modelling of an upwelling cell (negative density anomaly)

2. (BD-Hybrid-Superplume): Boundary Deformations Hybrid modelling with a superplume (anomaly from CMB to upper layers)

The search space for model BD-Hybrid-UC was similar to the BD-Grav-FULL model presented in Table 2.2. The results of the studies are presented in a similar order in Section 4.3.4. For the BD-Hybrid-Superplume model, several adjustments were made in the configuration, as shown in Table 2.3.

Table 2.3: The configuration settings in the modelling of BD-Hybrid-Superplume. Column 1 presents the variable. The parameters that were varied with respect to the **baseline** (indicated in bold) are listed in column 2. Column 3 states in which section the results of the corresponding search space can be found.

SFEC	**Settings**	**Results**
Solid core	No	Constant
Viscosity Profile	Profile **1**	Constant
SH	2-3, **2-5**	
Lithosphere thickness	**100**	Constant
Lithosphere density	2900 kg/m^3	Constant
Lithosphere viscosity η_{lith}	10^{30} Pa · s	Constant
Core radius	1597 km	Constant
C_{20}	95% removed	Always
Density Anomaly	**Settings**	**Results**
Thickness	1300, 1400, 1500, 1600 km	Section 4.3.5
Longitude size	[46 to 94] deg	Varied on best-fit
Latitude size	[-27 to 44] deg	Varied on best-fit
Density range	[-10 to 0 %]	Always
Depth	100, 200, 300, 400 km	Always

The longitude and latitude sizes were not varied for each configuration as this is computationally expensive. However, once a best-fitting model was found, the longitude and latitude sizes were varied in order to get an even more accurate model. The results of these models were analysed by the Similarity approach introduced in the following section.

2.4.4. SIMILARITY MODEL ASSESSMENT

Because of several limitations encountered in the Single Latitude Assessment of Models (Section 2.3.1), a new assessment method was created. This approach takes into account the complete areoid (and its geometrical features) instead of just one circle of latitude. Each field can be represented in the form of contour lines, indicating the locations of the same areoid height. Figure 2.17 depicts a visualization of the contour lines.

From the shapes of these contour lines, the similarity (between the modelled field and observed field) calculated with Equation 2.18:

$$S = \left[1 - \frac{U - I}{U}\right] \tag{2.18}$$

Where U is the union of the two shapes and I is the intersection. This is sometimes referred to as the Jaccard Index. S can range from 0 to 1, the higher the value the more similarity between the shapes. In our case, the similarity of the 0m, 200, 400 and 800 m areoid contours were determined separately. Figure 2.18 shows the shapes of the observed and modelled contour line at different areoid heights, and the intersection (I) and union (U).

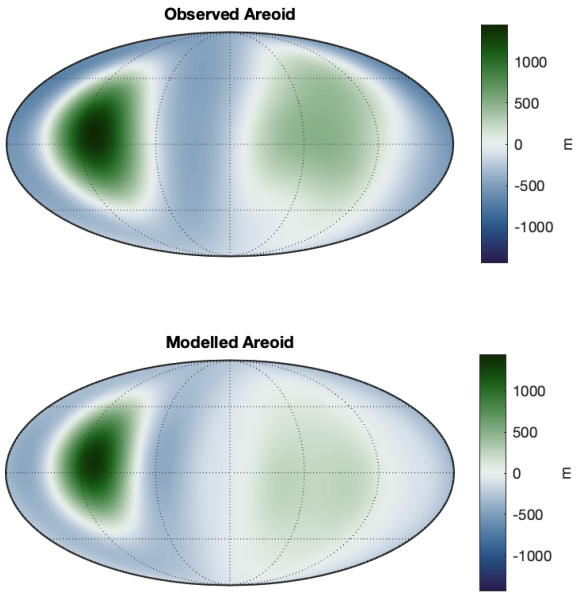

(a) A representation of the observed areoid and a modelled areoid. The configuration settings are not relevant for the purpose of this image.

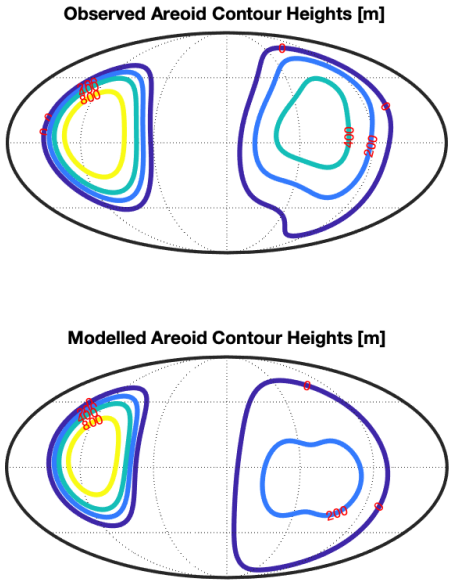

(b) A visualization of the areoid fields from (a), but expressed in contours lines. Each line consists of points with the same areoid value. The colors are selected to distinguish between different heights. Only the contours at areoid heights of 0, 200 400, 800 and 1200 meters are shown.

Figure 2.17: Observed and modelled areoid fields (Figure 2.17a) and their corresponding contour line representation (Figure 2.17b. All images are in Mollweide projection with a central meridian of 0 ° longitude. The hydrostatic flattening effect (95% of C_{20}) has been removed.

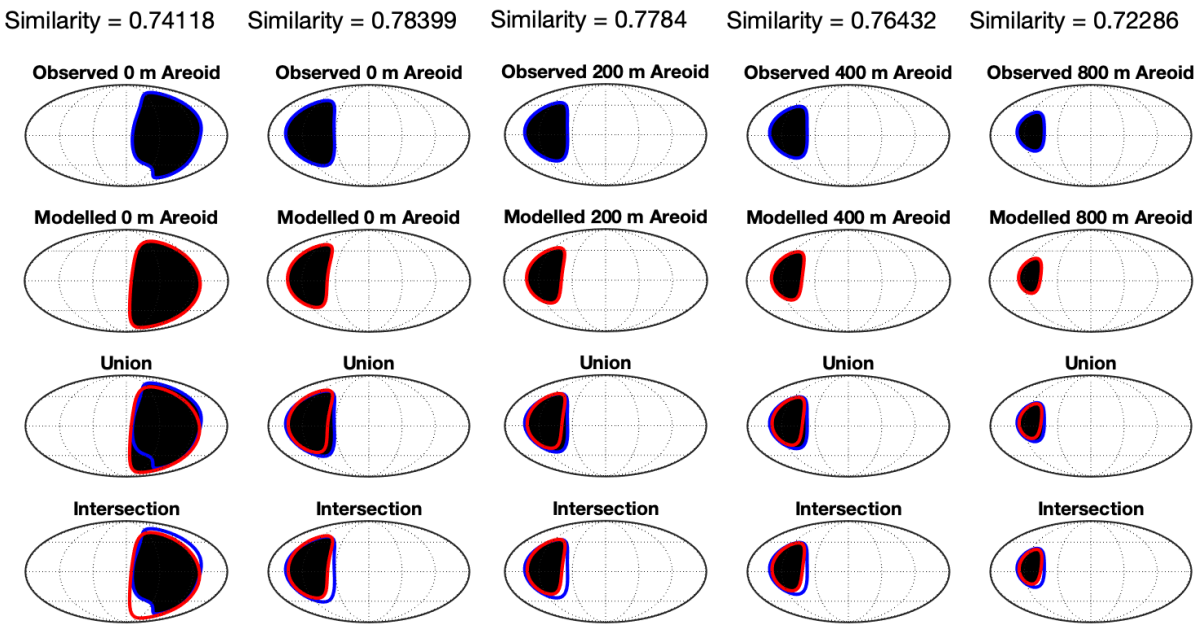

(a) Contour shapes for the 0 m contour on the Eastern hemisphere (antipodal to Tharsis).

(b) Contour shapes for the 0 m contour on the Western hemisphere (around Tharsis).

(c) Contour shapes for the 200 m contour on the Western hemisphere (around Tharsis).

(d) Contour shapes for the 400 m contour on the Western hemisphere (around Tharsis).

(e) Contour shapes for the 800 m contour on the Western hemisphere (around Tharsis).

Figure 2.18: From top to bottom Mollweide projections: contour shape of the observation, contour shape of the model, the union of the observed and modelled contour shape, and the intersection of the observed and modelled contour shape. The value for the similarity of that specific contour line is presented above the Mollweide projections. All images are in Mollweide projection with a central meridian of 0 ° longitude.

The similarity between the observed areoid contours and the modelled areoid contours is calculated by using the areas of the union and the intersection and inserting them in Equation 2.18. A similarity of 1 means

that the model matches the observation precisely ($U = I$), a similarity of 0 means that there is no overlap ($I = 0$). The more contour shapes of the model are compared to the observation, the better the computed value represents the actual similarity between the two fields. For this research, the contour lines 0m, 200m, 400m and 800m on the Western hemisphere and the 0m contour on the Eastern hemisphere (antipodal to Tharsis) are considered. This selection was chosen since those areoid heights characterize the gravity potential field at the Tharsis rise well when considering either SH degrees 2-3, 2-4 or 2-5. If one would choose an areoid height above 1200 m , this mode of analysis fails in SH 2-3 and SH 2-4 since the 1200m areoid only comes into existence at $n = 5$ and higher.

The computed similarities of each of the contours are averaged using a weighted average according to the area of the contour shapes. The larger the area of the contour, the smaller the weight. The consequence is that more importance is giving to the similarities of the higher areoid contours (e.g. 800m) - which have a smaller area. Equation 2.19 is used to compute the total similarity, which is used as key parameter to determine the goodness-of-fit of a model.

$$S_{total} = \sum_{n=1}^{N} \frac{\frac{1}{A_n} \cdot S_n}{T} \tag{2.19}$$

Where $T = \sum_0^n \frac{1}{A_n}$, the sum of the weights applied. S_n the similarity of contour line n. N is the total number of contours analysed, which was 5 throughout this research.

As already elaborated upon in Sections 2.3 and 2.4, the models that were researched have an initial configuration (SFEC and Density anomaly settings). For each configuration, a range of anomaly density ($\Delta\rho$) and a starting depth (D_a) of the anomaly was considered. For each density and depth, the similarity of each of the contours in the modelled field is calculated. By presenting the similarities in a heat map, one can get insight into what depth and density parameters result in well-fitting models (those with a high similarity). Figure 2.19 illustrates an example of such a heat map. Only the weighed average heat map of the similarities (see Figure 2.19f) is presented in Chapter 4 to determine which configurations model the observations.

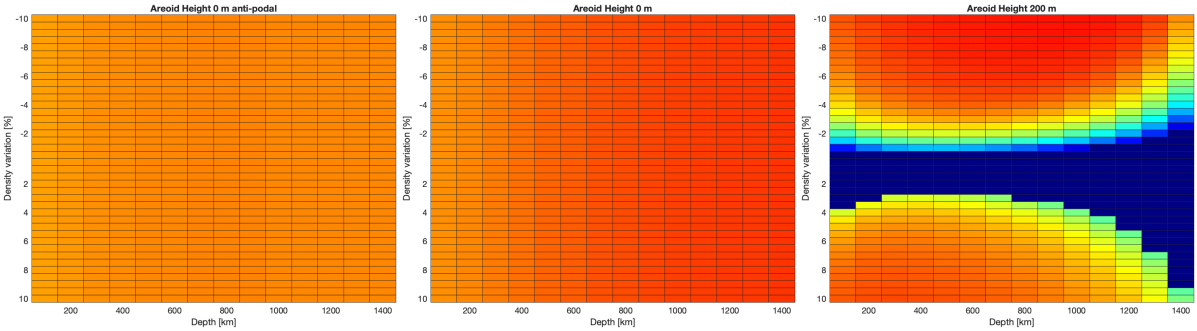

(a) Heat map of similarities between model and observation for the 0 m contour on the Eastern hemisphere (antipodal to Tharsis).

(b) Heat map of similarities between model and observation for the 0 m contour on the Western hemisphere (located around Tharsis).

(c) Heat map of similarities between model and observation for the 200 m contour on the Western hemisphere.

(d) Heat map of similarities between model and observation for the 400 m contour on the Western hemisphere.

(e) Heat map of similarities between model and observation for the 800 m contour on the Western hemisphere.

(f) Heat map of the weighted average of the similarities presented in Figures (a) to (e). These values represent the total similarity (S_{total}).

Figure 2.19: Similarities of contours at a specific areoid height for a range of depths and densities of the anomaly. Figure 2.19f presents the weighted average, this value was used as ultimately parameter to assess goodness-of-fit. The similarities range from a value of 0 (bad fit) to a value of 1 (perfect fit).

The interpretation of those heat maps is explained by using Figure 2.19. A brief look at Figures 2.19a and 2.19b shows that for these areoid heights, the heat maps show almost the same color for all depths and density variations. This means that the similarity, and therefore the performance of the model, does not depend on the depth and density of the anomaly in this depth-density regime. Figure 2.19c - representing similarities for the 200 m areoid on the Western hemisphere - depicts high similarities at large negative density variations (above -4 % in the heat map), so these are good fits. From -2% to approximately 2% the similarity is very low (close to zero), meaning that those models do not match the observations well. For a density variation of approximately 3% (depending on the depth), the similarity indicates a yellow-ish color: between 0.5 and 0.6 similarity. So solutions in this regime fit the observations reasonable, but not as well as the regime above -4 % density variation. For the areoid heights of 400 m (Figure 2.19d), the similarities of the positive density variation regime decrease significant (they are light blue - indicating a similarity of about 0.35). In Figure 2.19e, for an areoid height of 800 m, those positive density variation models result in a similarity of 0, meaning that is does not fit the observation. Moreover, in this figure an orange line (of high similarities) is observable in the large negative density variation regime. This indicates the well-fitting models (and depend on both depth and density variation). Ultimately, the weighted average of all the similarities is calculated, this is presented in Figure 2.19f. This plot is primarily used in the assessment of the models. The validation and verification of the methods is elaborated upon in Chapter 3. Chapter 4 presents the results of each of the models that were introduced.

3

VERIFICATION AND VALIDATION

In addition to the verification and validation (V&V) steps that have been undertaken in the method and results, some V&V tests were performed in parallel to the study. This chapter presents the V&V on the datasets in Section 3.1, models in Section 3.2 and new software in Section 3.3. The areoid is often referred to as 'geoid' throughout this chapter, as other studies often refuse to change their terminology to Martian standards.

3.1. DATA PREPARATION

The topography data that is used for this study is the MGS MOLA dataset from Smith (2003), represented in spherical harmonics. These spherical harmonics are converted by the software into a topography grid that can be represented on a map. In order to validate this process of converting from spherical harmonics to a grid, the resultant topography is compared with a published topography map by Wieczorek (2015) in Figure 3.1.

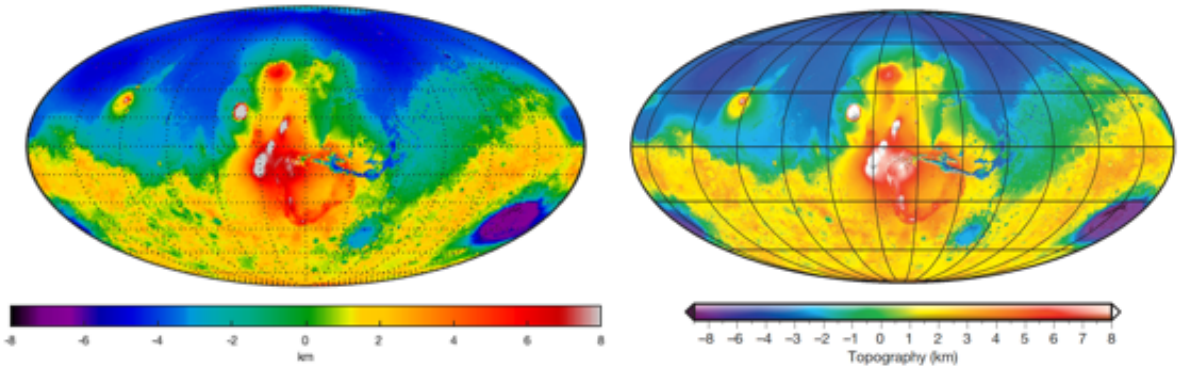

Figure 3.1: Left: Obtained topography grid field after converting the spherical harmonic datasets. Right: Topography as presented in Wieczorek (2015). In both cases, the colorbars are clipped at -8 and 8 km. Both images are in Mollweide projection with a central meridian of 100 ° W longitude. SH degrees: 1-75.

As can be seen in Figure 3.1, the topography of the MGS MOLA dataset matches the topography presented by literature. One should note that the fields created by Wieczorek (2015) contain a topographic relief on top of the maps, making it slightly more difficult to compare the two fields precisely. In addition to this visual confirmation, several points in the field have been selected and compared manually.

For the gravity data, the spherical harmonic dataset of GMM-3 by Genova et al. (2016) has been used. This set of spherical harmonics is converted into a gravity field by the GSH code. A validation of this data and conversion has been performed with results obtained by Wieczorek (2015). The gravity anomalies are shown in Figure 3.2.

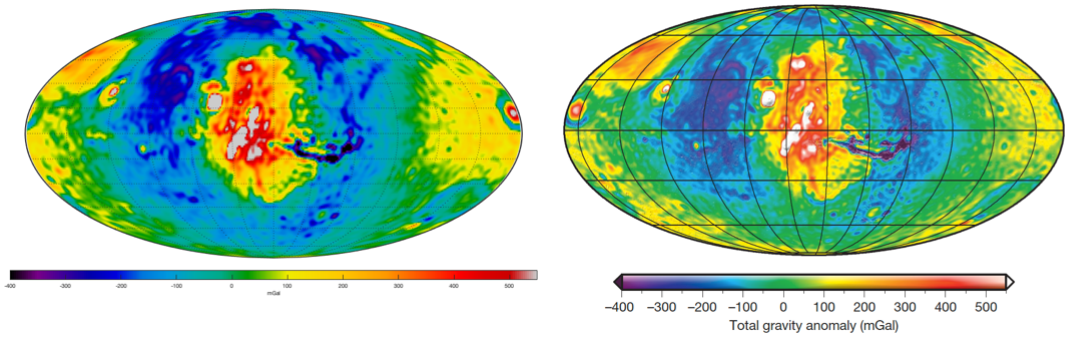

Figure 3.2: Left: Obtained gravity anomaly grid field after converting the spherical harmonic datasets. Right: Gravity anomaly as presented in Wieczorek (2015). In both cases, the colorbars are clipped at -400 and 550 mGal. Both images are in Mollweide projection with a central meridian of 100 ° W longitude. SH degrees: 2-75, where C_{20} has been removed for 95 %.

The obtained gravity anomaly field fits quite well. However, a higher number of yellow spots on the high latitude regimes are visible in the field presented by Wieczorek (2015). A possible explanation of this difference is that Wieczorek (2015) used a reference ellipsoid obtained by Ardalan et al. (2010), while the GSH code did not use this approach. Moreover, it could be the case that the colorbars have a slight mismatch is the yellow-green region which results in the discrepancy. As the gravity anomalies of small wavelength features are not relevant for this research, these discrepancies were not investigated in further detail. The areoid (geoid), which is the primary form of data field that is used throughout this study, is represented and compared in Figure 3.3.

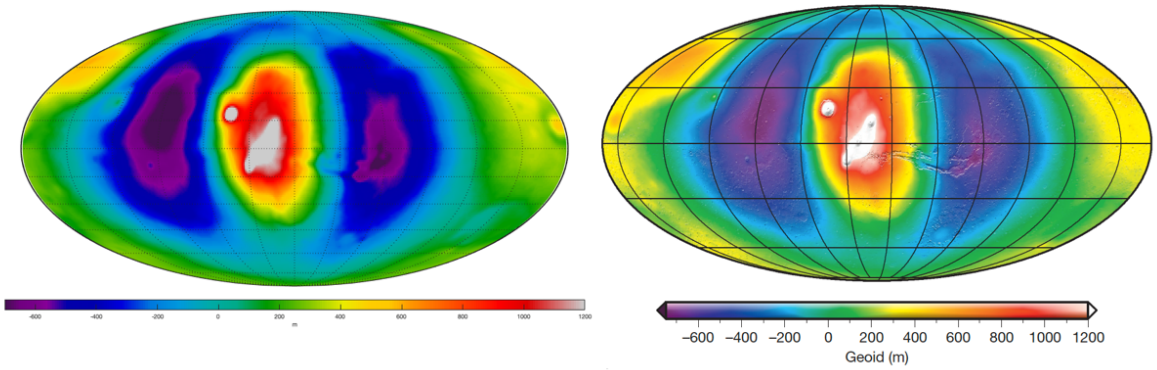

Figure 3.3: Left: Obtained geoid grid field after converting the spherical harmonic datasets. Right: Geoid as presented in Wieczorek (2015) . In both cases, the colorbars are clipped at -700 and 1200 m. Both images are in Mollweide projection with a central meridian of 100 ° W longitude. SH degrees: 2-75, where C_{20} has been removed for 95 %.

Figure 3.3 shows that the areoid of this study (for spherical harmonic degrees 2-75) matches the areoid of Wieczorek (2015) in great detail. Slight variations are visible in the deep purple areoid heights and the green-yellow regime. However, those differences are allocated to the small difference in colorbar. Hereby, the datasets and their conversion to grids have been validated.

The next test involves comparison of the intermediate results of this study to the studies of Steinberger et al. (2010) and Zhong and Roberts (2003), as the results are compared to both studies. Steinberger et al. (2010) addressed the possible sub-lithospheric origin of the Tharsis bulge, and Zhong and Roberts (2003) researched the dynamic contribution to the observed areoid. Both studies have their own methods of preprocessing their data. To ensure that the approaches used in this study are comparable to those of Steinberger et al. (2010) and Zhong and Roberts (2003), the intermediate results are validated (in the same order).

In this study, a gravity power spectrum was used for determining the contributions of each spherical harmonic degree to the gravity field (see Figure 2.1). However, this spectrum is expressed in mGal while the power spectrum of Steinberger et al. (2010) is expressed in m. This makes it difficult to compare and

to determine whether this study actually starts with the same assumptions as Steinberger et al. (2010). In order to validate our power spectrum, the downward-continuation method that is introduced in Steinberger et al. (2010) has been applied. Additionally, the gravity field power spectrum is converted to a gravity potential (areoid) power spectrum to obtain the unit m. The spectrum obtained in this research is depicted in Figure 3.4 on the left. The power spectrum from Steinberger et al. (2010) is presented on the right. Because Steinberger uses the JGM95J01 gravity field model and this study uses the GMM-3, both spectra are visualized.

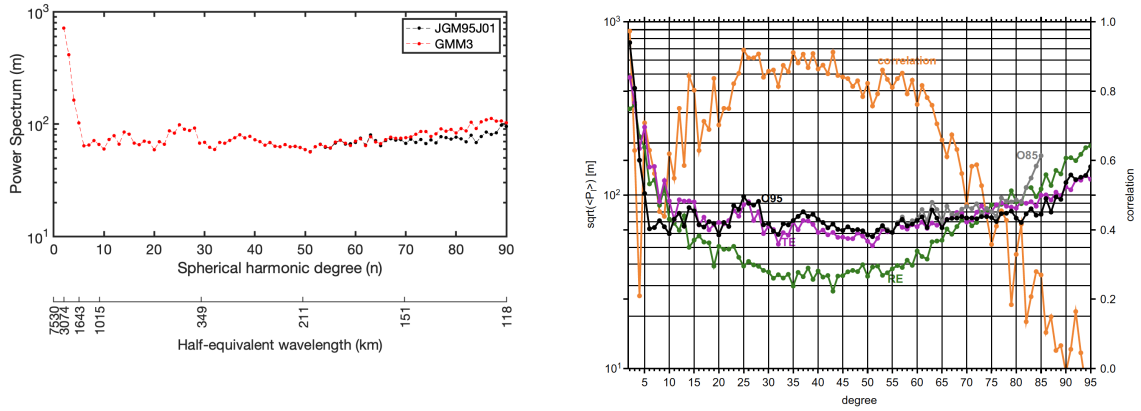

Figure 3.4: Left: Gravity power spectrum (square root of power per degree downward-continued to depth 120 km) for models JGM95J01 and GMM-3. Right: power spectrum obtained by Steinberger et al. (2010). The black line (O95) is the observed gravity field and should be compared to the power spectrum of GMM-3 from the left figure.

Figure 3.4 shows that the power spectrum obtained in this study matches the O95 power spectrum of Steinberger et al. (2010). Additionally, the left figure shows that the GMM-3 observations do not differ significantly from the JGM95J01 (validated) observations. A slight deviation can be seen from degree 65 onwards, but since the interest of this study is in the low degrees this deviation is of no concern. Hereby, it is known how to obtain the results of Steinberger et al. (2010) with the available data. This verifies that all the processing steps of Steinberger et al. (2010) have been identified and it can be stated that their conclusions are valid for the data used in this study. Therefore, this validates the assumption of sub-lithospheric density anomalies being present in Mars that play a role in the creation of the areoid bulge.

Another study to which the results from this research are often compared to is Zhong and Roberts (2003). A validation is performed with the $R_{G/T}$ values as derived by Zhong and Roberts (2003). Firstly, the topographies are plotted and compared to those presented by Zhong and Roberts (2003), this is visualized in Figure 3.5.

The fields in Figure 3.5 seem to match the fields presented by Zhong and Roberts (2003). For spherical harmonics 2 to 3, a smaller yellow region at Tharsis is observed in the results compare to Zhong's topographic field from SH 2-3. The values around this location have been checked manually and are close to the values observed in the plots of Zhong and Roberts (2003). It can therefore be concluded that the colorbar that is used for the obtained topography field is slightly different from the colorbar used by Zhong, this difference seems to have influenced the green-yellow (0 to 4 km) topographic elevations. For a more thorough validation of the topography and geoid data that is used, the ratio of geoid-to-topography ($R_{G/T}$) has been calculated by Zhong. To compute this, the power per degree is defined in the following way:

$$\sigma(n) = \sqrt{\frac{\sum_{m=0}^{m=n}(C_{nm}^2 + S_{nm}^2)}{2n+1}} \tag{3.1}$$

Note that the normalization of 2n+1 applied to the power per degree computation (Goossens et al., 2020), this was not mentioned by Zhong and Roberts (2003) and therefore has likely to do with the normalization of the coefficients. So with this RMS power per degree, $R_{G/T}$ is determined by:

$$R_{G/T}(n) = \frac{\sigma_G(n)}{\sigma_T(n)} \tag{3.2}$$

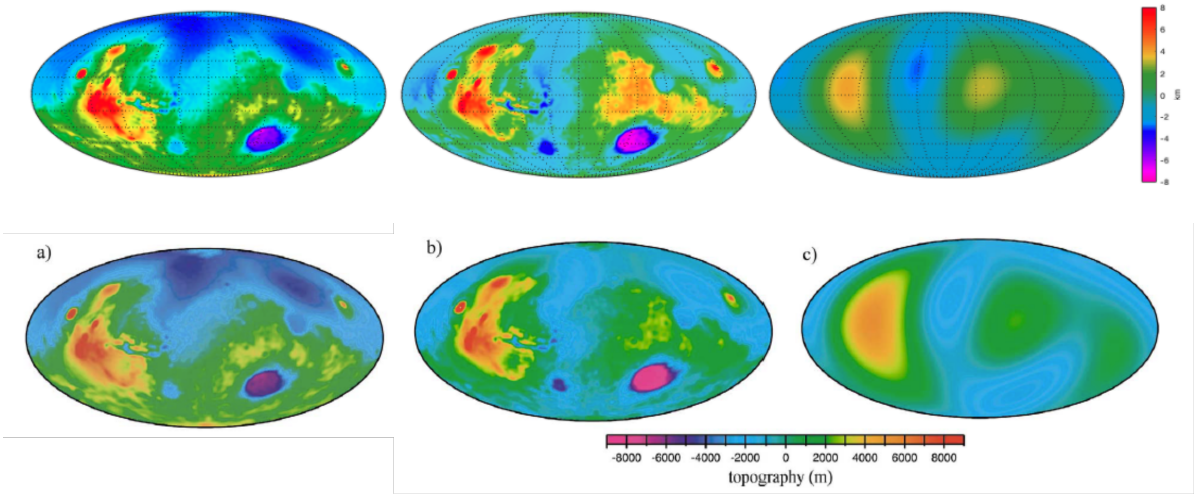

Figure 3.5: Top: Obtained topographies in this study for different spherical harmonics. Bottom: Topographies obtained by Zhong and Roberts (2003) represented in the same order. From left to right: spherical harmonics 1-70, spherical harmonics 2-70 (degree 1/crustal dichotomy is removed) and degree spherical harmonics 2-3 (no crustal dichotomy).

The values by Zhong and Roberts (2003), along with the values obtained in this study, are presented in Table 3.1.

Table 3.1: Ratio of geoid to topography for degrees 2 to 5.

Degree (l)	$R_{G/T}$	Zhong $R_{G/T}$	Topography (km)	Zhong Topography (km)	Geoid (km)	Zhong Geoid (km)
2	0.3013	0.30	4.2801	4.275	1.2898	1.283
3	0.1899	0.19	3.4709	3.481	0.6592	0.655
4	0.1132	0.11	1.9834	1.984	0.2244	0.223
5	0.0469	0.05	2.6406	2.661	0.1238	0.123

An important remark to be made about Table 3.1 is that 95% of the C_{20} effect is removed by Zhong and Roberts (2003) to account for hydrostatic flattening. When this has not been taken into account (for instance by removing the complete term), the $R_{G/T}$ of degree 2 deviates from the value found by Zhong and Roberts (2003).

By the validation process described above, both the topography and the gravity potential datasets have been verified. Moreover, the conversion from a set of spherical harmonic coefficients into the correct fields is proven correct, including the normalization of the coefficients and removing the correct amount of hydrostatic flattening from the C_{20} term. The GSH has been verified many times before this study, but since it is a crucial element to this study, it was done here as well. Section 3.2 will verify the software that is used to create crustal models and to put density anomalies in the mantle.

3.2. MODELS

In previous research (e.g. (Root et al., 2016)), the GSHA code has been verified already. However, putting a density anomaly somewhere in the mantle is not the usual way in which the code is used, and therefore some V&V steps have been undertaken.

First of all, a check was performed to determine whether all dependencies (other functions called by the GSHA code) work properly. For instance, the boundaries of the layers are required as input for the GSHA code, these boundaries are stored in a gmt format. A thorough check was performed to verify that the gmt file is translated correctly onto a grid, the reverse was also verified.

This study requires running a large number of iterations in which it is possible that the location of the anomaly, and therefore the boundaries of this anomaly in the gmt file, change each iteration. For this reason,

the writing of grid to a gmt file has to be completed before the gmt file is read by the GSHA. In order to save storage and reduce complexity, the gmt file is overwritten every iteration. A check was performed that the file is always overwritten before being accessed, otherwise the gmt file of the previous iteration is used in the current iteration, which yields the wrong results. A pausing time was implemented in the code of 1 second to ensure that this process works smoothly.

A test has been performed to determine whether the GSHA code would yield similar results as Mussini (2020). For this, the Bouguer Anomaly is determined, but it works also for a multi-layered mantle (e.g. Airy isostasy) or a density anomaly in the mantle. Figure 3.6 compares the Bouguer anomaly results with those obtained by Mussini (2020).

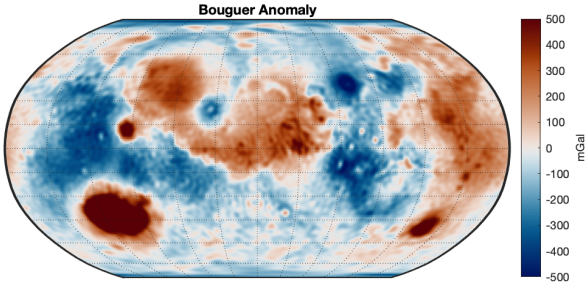

(a) Bouguer anomaly without degree 1 (crustal dichotomy).

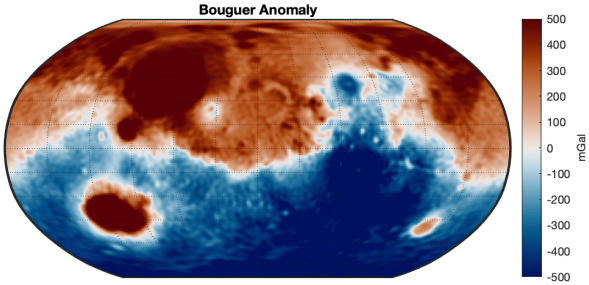

(b) Bouguer anomaly with degree 1 (crustal dichotomy).

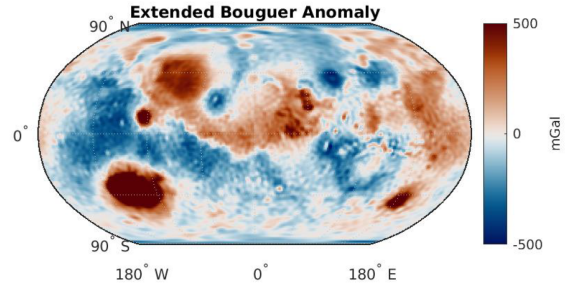

(c) Bouguer anomaly without degree 1 (crustal dichotomy) by Mussini (2020).

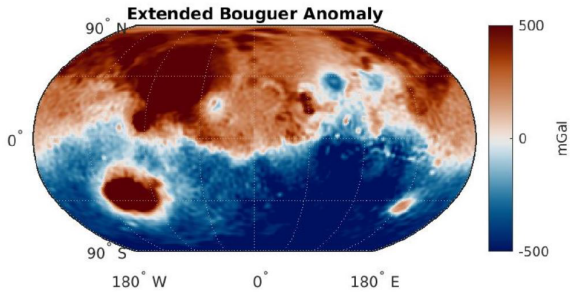

(d) Bouguer anomaly with degree 1 (crustal dichotomy) by Mussini (2020).

Figure 3.6: Bouguer anomalies obtained after subtracting the bouguer correction from the observed gravity field. A crustal density of 2800 kg/m^3 is assumed. Images (a) and (c) are in SH degrees 2-90. Images (b) and (d) in SH degrees 1-90. The colorbars have been clipped at -500 and 500 mGal. All images are in Robinson projection with a central meridian of 180 ° E longitude (the longitudinal labels in Mussini (2020) are incorrect).

Figure 3.6 shows that the obtained Bouguer anomalies correspond to the ones presented by literature. Therefore, the GSHA code does properly take into account the boundaries (and densities) of the input. In addition to the Bouguer anomaly, an Airy isostatic reduction is performed. Since GSHA takes the boundaries into account correctly, the determination of the crustal roots under the Airy compensated topography should be verified. This was done by manually calculating the crustal root depth at several latitude,longitude locations and verifying it with the grid presenting the lower boundary of the crust. The next step is to validate that a density anomaly is actually modelled at the pre-determined location. A code is written that creates the boundaries of the density anomaly, this anomaly has an upper and lower boundary and will be placed in the mantle. In order to verify whether the anomaly is placed correctly, all layers analysed by the GSHA are plotted, see Figure 3.7.

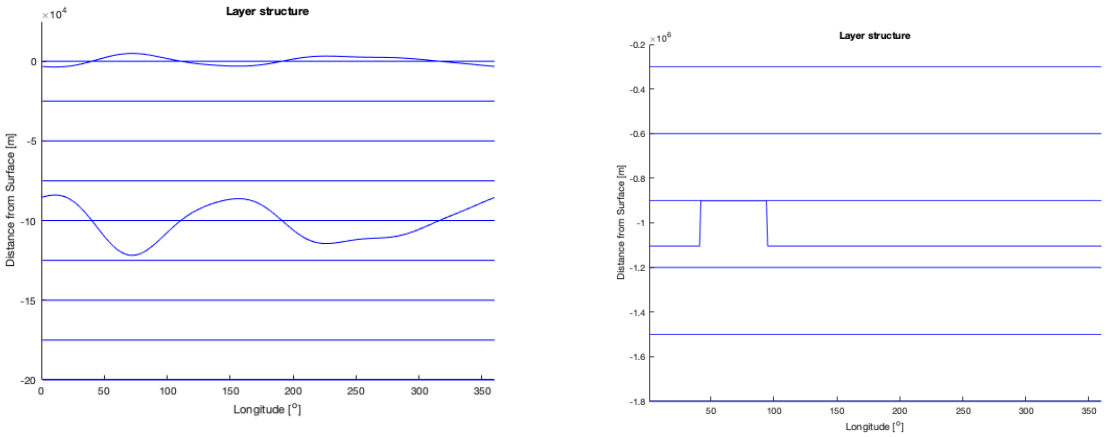

(a) Layer structure in the GSHA code for an Airy isostatic crustal root (at a zero-elevation crustal thickness of 100 km).

(b) Layer structure in the GSHA code for a density anomaly.

Figure 3.7: Layer structures in GSHA to check whether the boundaries are taken into account correctly. The density anomaly is visualized in Figure 3.7b.

Figure 3.7 shows that the density anomaly is placed at the right location. The code for the creation of the boundaries of the density anomaly and its implementation in the GSHA is now verified. Note that the layer does not have to end exactly on the bottom of the boundary, since the goal is to model density anomalies. With this verified code, the DA-Models are researched. However, the BD-Models require an additional tool that is not verified for Mars yet; SFEC.

3.3. SFEC

SFEC is a mantle convection code that computes the boundary deflections of the surface topography and CMB topography. Due to these deformations, the gravity field changes with respect to a model where the boundary are static (GSHA). The SFEC code was delivered (and verified) for an Earth configuration so it has to be verified for a Martian model. The code runs primarily with Fortran and is compiled from command line (Terminal).

The received code is tested with the Earth configuration in order to check whether the model works properly for Earth. A visual inspection of the resulting geoid was performed and verified. The next step consists of changing the parameters to a Mars configuration and verifying the results. This is done with the help of the thoroughly tested GSHA code. The SFEC output contains a static potential (of the mantle anomaly) which should be exactly similar to the geoid resulting from the GSHA code, which does not take into account any dynamical effects and is therefore inherently static. In both of the models, a density anomaly of 100 km is constructed with the same longitudinal and latitudinal boundaries. The GSHA results are compared with the static geoid results of SFEC, they should be identical. The complete process up to the final validation is elaborated upon for other SFEC users to spot similar discrepancies if they wish to validate their own results.

It should be noted that a term "$fatt$" was added as multiplication factor of the static geoid, since the received code was missing this factorization. This term is a normalization that is used to in the process of calculating the spherical harmonic coefficients. Testing the processing of SFEC coefficients resulted in the fields presented in Figure 3.8. This was due to an incorrect longitude range which resulted in the field shifting one pixel to the left every row, resulting in the curvy pattern.

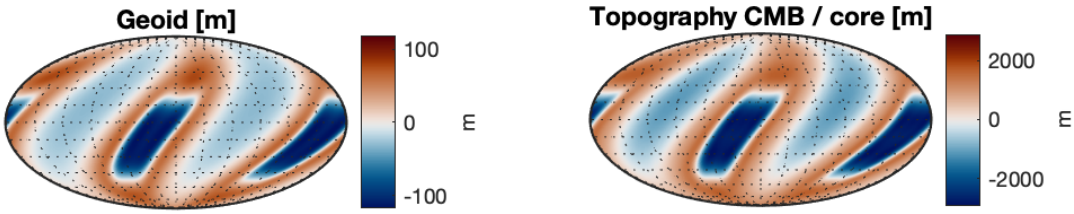

Figure 3.8: Processing mistake that was encountered when performing the analysis (going from coordinates to the gridded fields).

After fixing the curved pattern presented in Figure 3.8 by adjusting the longitude range, several other discrepancies are detected, as presented in Figure 3.9.

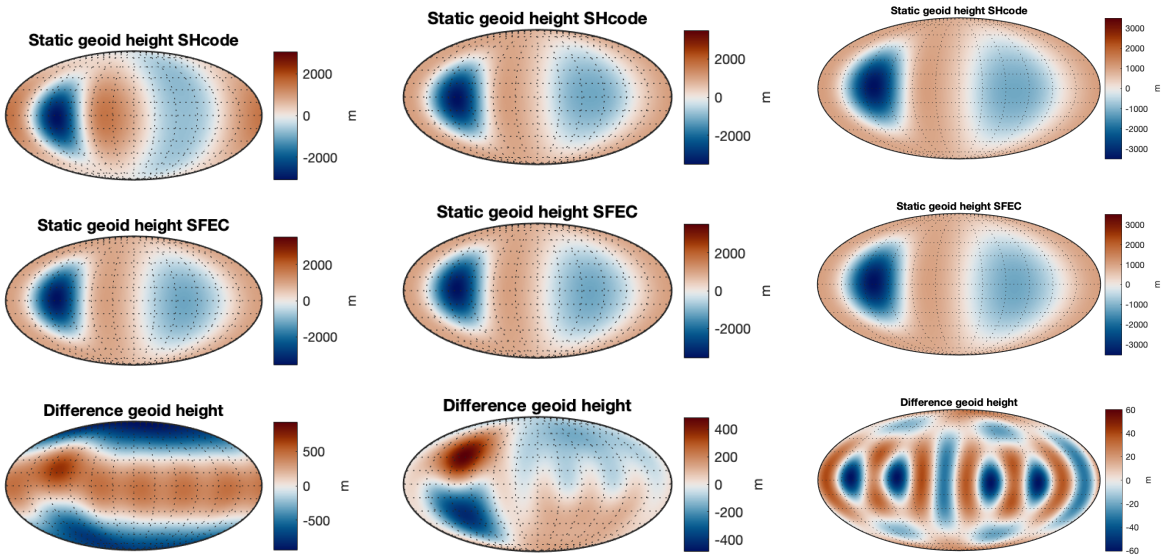

(a) C_{20} discrepancy

(b) Latitude mirror discrepancy

(c) Spectral resolution discrepancy

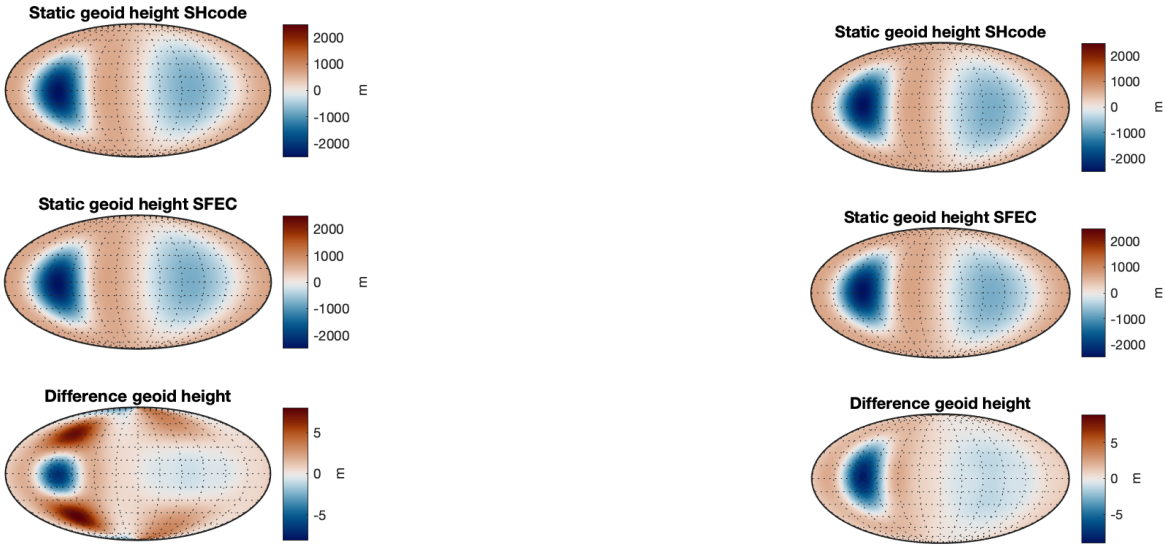

(d) Latitude grid range discrepancy

(e) Gaussian grid discrepancy (Assumed)

Figure 3.9: Intermediate results of the SFEC validation process.

Each of the intermediate results presented in Figure 3.9 is elaborated upon in this paragraph. The C_{20} discrepancy (Figure 3.9a) is the result of GSHA code in which this term was not removed. Because it is always removed in the results from SFEC (which considers a spherical model of Mars), this effect was visible in the difference between the two models (bottom plot). Figure 3.9b shows very similar static geoid heights computed by the GSHA code and the SFEC code. However, after subtracting the two fields a mirrored (red and blue is mirrored) field arises. This pattern is due to a mirrored field in the 0 latitude (equator) line, which is fixed by mirroring the GSHA field. Consequently, Figure 3.9c presents an even smaller difference between the two models (the difference in geoid height is 50 m at maximum). The pattern visualized in Figure 3.9c is due to a discrepancy in spherical harmonics used to represent the grid fields; spherical harmonics 2-6 were used for SFEC, while 2-5 were used for the GSHA grid. Removing this discrepancy leads to Figure 3.9d, where only a maximum difference of -7 m is observed. The pattern in the bottom plot of this figure is mirrored in the equator and shows a negative as well as a positive discrepancy at the location of the anomaly. This effect seemed to be the results of the latitude limits that are assumed by SFEC: -89.24 to 89.24. After changing the limits to the same values in GSHA, the results presented in Figure 3.9e appeared, having a clear discrepancy only at the location of the anomaly. After further investigation, this effect seemed to be caused by the fact that the gravitational field from SFEC is presented on a Gaussian grid (which has a different latitudinal spacing) while the GSHA code maps the spherical harmonics on an equi-angular grid.

By comparing the coefficients of both of the methods, a relationship was found between the degree and the error that was produced, this is presented in Figure 3.10. The fact that the difference increases with the spherical harmonic degree could be due to a normalization term (that depends on degree n). However, it is expected to be related to the Gaussian grid on which SFEC calculates the field. The data points at the peak of the areoid bulge are better modelled in SFEC because the Gaussian grid has more data points around the equator (at the location of the peak). The lower the spherical harmonic degree, the higher the spectral resolution, and the better those data points are presented in the Gaussian frame of SFEC. This could be the reason why the error increases with increasing spherical harmonic degree. Since the focus of this study is on spherical harmonic degree up to 5, the error that is observed between the SFEC and GSHA coefficients is smaller than the measuring accuracy, so the error is neglected in this study.

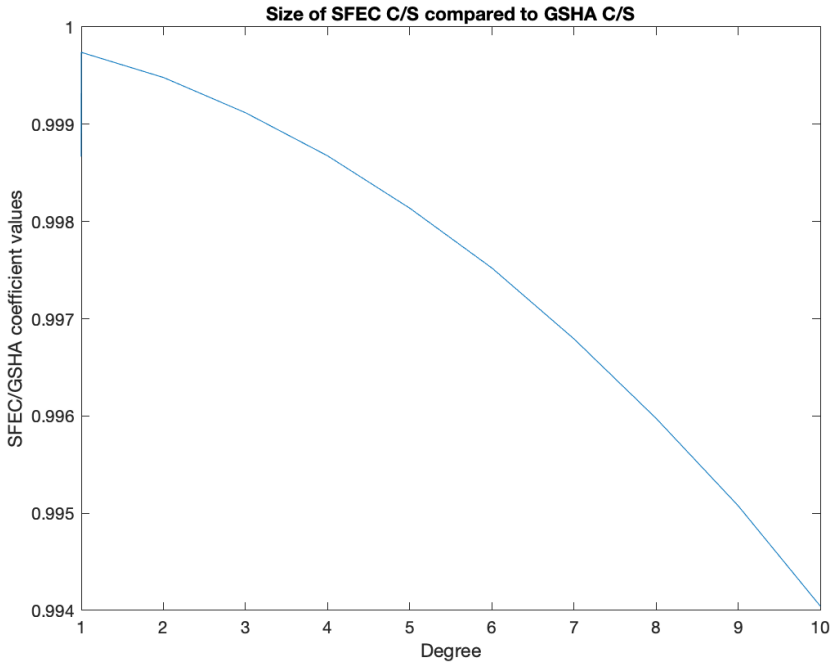

Figure 3.10: Relationship between SH degree and the ratio of the coefficient values ($\frac{SFEC}{GSHA}$)

Besides the gravity fields that are computed by SFEC, the adjusted input files are verified. For the received SFEC code, a tomography file of Earth's interior was used for the determination of the interior density profile.

No such tomography file is present for the Martian mantle, so a homogeneous mantle is assumed. The density anomaly that is placed in this mantle has to be represented by the tomography file.

Firstly, the tomography file contains the density variations, expressed in spherical harmonic coefficients, for each layer. If there is no density anomaly placed inside that layer, it means that there is no density variation and therefore the tomography should state all zeros for the spherical harmonic coefficients in that layer. If there is a density anomaly, the tomography file should contain the spherical harmonic coefficients that represent this anomaly. It was manually verified that the tomography file consists of 17 layers, and that only the layers that contain a density anomaly had non-zero spherical harmonic coefficients. Additionally, the depth of each layer (also indicated in the tomography file) has been verified.

Besides the tomography file, an input is required for the viscosity profile. In the original SFEC code, the option was enabled to put in the viscosity of the lithosphere, upper mantle and lower mantle. The robustness study of this research required a more refined viscosity profile so the code was altered to be able to ingest an ASCII file specifying the viscosity of each of the 17 layers. The ingestion of this data by SFEC works accordingly and is verified. The viscosity profile that is used primarily is the profile suggested by Steinberger et al. (2010). In order to verify that the profile used in this study is the same, they are compared in Figure 3.11.

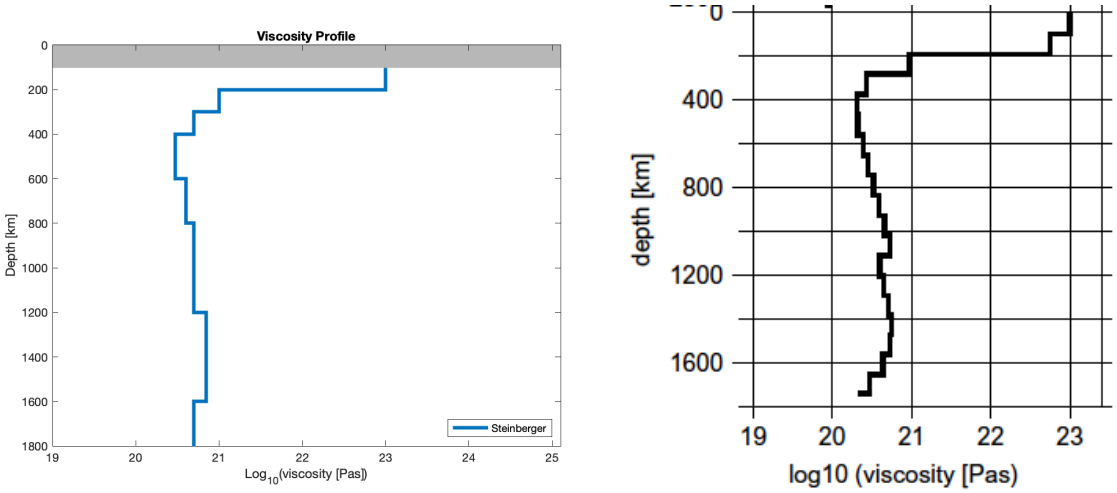

Figure 3.11: Left: viscosity profile ingested by SFEC. Right: viscosity profile by Steinberger et al. (2010).

As can be seen in Figure 3.11, the viscosity profile used in this study closely matches the one published by Steinberger et al. (2010). A noticeable difference is the step size used by Steinberger et al. (2010), resulting in a more refined viscosity profile. Because the ingestion of the SFEC is limited to 17 layers, the viscosity profile could not be more refined. However, it is much more detailed (17 layers) with respect to the received SFEC version (3 layers). The ingestion of the viscosity layers is hereby verified.

In addition to the ingestion of the inputs, it was verified that adjusting the CMB contribution actually turned of the effect on the CMB on the observed areoid. Moreover, a Fortran warning 'iflag' arose in the *modules.f*90 file, this was due to a mistake in 'goto' terminology. It was verified that this warning was not influencing the results and the error warning was fixed.

Hereby, the modifications that have been applied to SFEC are all validated and verified. The received code was already validated before and therefore it is save to state that the code can be used for obtaining the results. A final validation study has been conducted on the performance of the Similarity tool, this is discussed in the next section.

3.4. MODEL ASSESSMENT

The assessment of the BD-Models required the development of a new method. This section verifies that this approach works according to the requirements.

Firstly, the code finds all contours at a specified contour height that are present in the grid field. It could be the case that multiple contours exist for one height. For instance, the areoid-height of 0 m has at least two contours; one around Tharsis and one around the areoid high anti-podal to Tharsis. For the Martian gravitational field up to degree 5, it has been verified that the code works properly, so the right contours are selected. However, if one desires to analyse the field at higher spherical harmonic degrees, the code could be prone to mistakes and select the wrong contours. This is because the higher the spectral resolution, the more contours lines are observed for a specific contour height, and the code does not know which contour to choose for analysis.

Sometimes, a scenario is encountered in which a closed contour has to be compared with an open contour. An example is presented in Figure 3.12a.

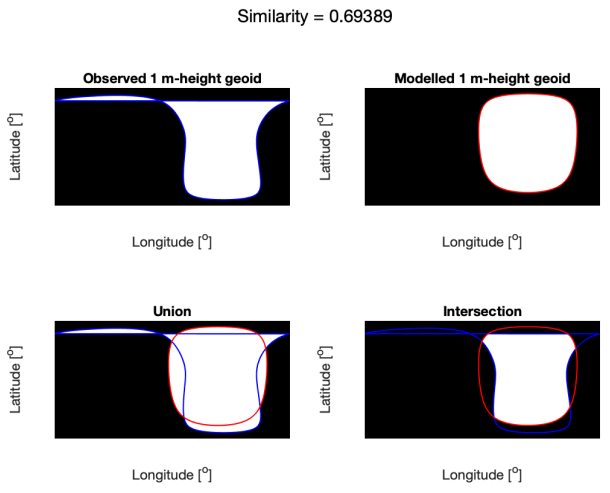

(a) Example of a contour where the observed contour is open while the modelled contour is closed, even in this extreme case the similarity functions works properly. A visual check was performed for all other contours.

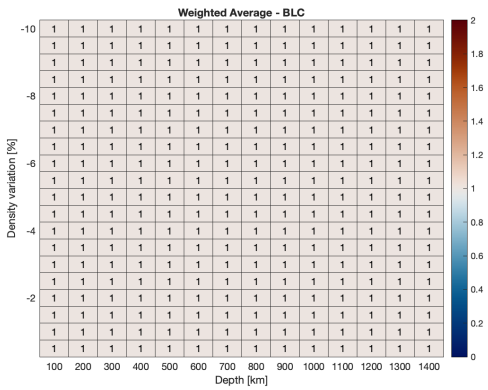

(b) Validation that the comparison of average similarities of the baseline with itself results in 1 on all data points.

Figure 3.12: Supporting images for the validation of the similarity method.

Figure 3.12a shows that the comparison of an open contour (left column - top figure) and a closed contour (right column - top figure) is done correctly. The union and intersection are determined without errors. The selection of the right contours is hereby verified and the calculation of the similarities can be performed. Several similarities are manually re-calculated to determine whether their weighted averages are computed correctly by the code. This test was passed. Moreover, Appendix D discusses several instances where the heat map of a model is compared to the baseline to determine the differences. This comparison is done by dividing the heat map of the model by the heat map of the baseline, which can be validated by proving that the comparison of the baseline to the baseline would result in 1 for all configurations. Figure 3.12b shows that this is indeed the case. Hereby, the approach to comparing the solutions to one another is verified.

4

RESULTS

This chapter presents the findings of the conducted studies. In section 4.1, an Airy isostasy model is created, enabling the computation of the gravity due to the crust and removing this from the observation. The remainder, after applying this crustal reduction, is the gravity field due to the mantle. Section 4.2 presents several potential configurations of density anomalies that closely model the observed mantle gravity field. However, stresses (mantle convection) have not been taken into account in this study. Therefore, Section 4.3 presents the results when the stresses caused by density anomalies are computed as well. This section will investigate a possible superplume under Tharsis as well.

4.1. CRUSTAL REDUCTION

The results of a study into an Airy isostatic crust are presented in this section. Several studies have attempted to determine the best fitting models by varying the zero-elevation crustal thickness, crustal density and mantle density. Overall, a crustal density of 2900 kg/m^3, a mantle density of 3550 kg/m^3 and a crustal thickness of at least 45 km are found to be the best-fitting parameters (Backer, 2018). Firstly, the sensitivity of the (Airy) model on the mantle density, crustal density and zero-elevation crustal thickness is determined. Figure 4.1 presents the overall RMS of the gravity field (R-component of the gravity vector) when varying those parameters.

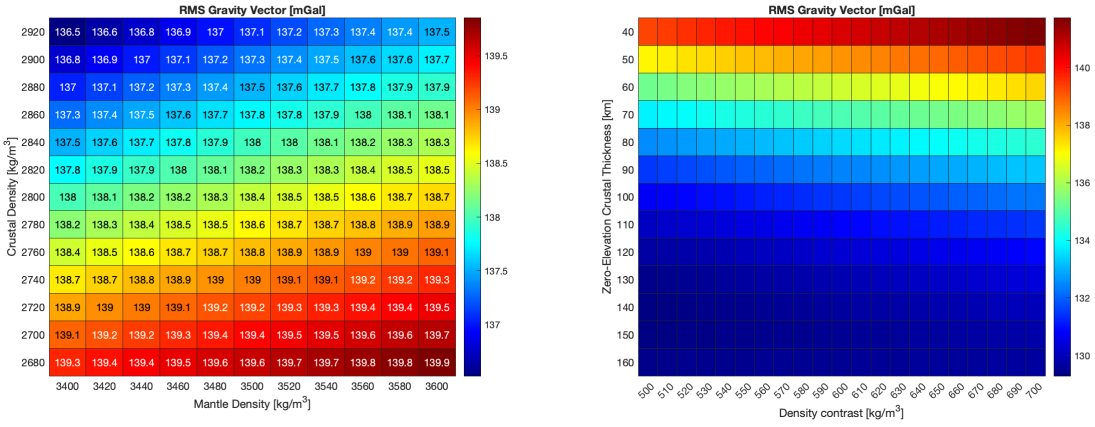

(a) RMS of the R-component of the gravity vector for a varying mantle density and crustal density. The zero-elevation crustal thickness is 55 km and constant.

(b) RMS of the R-component of the gravity vector for a varying density contrast and zero-elevation crustal thickness.

Figure 4.1: RMS of the R-component of the gravity field vector at different settings. The lower the RMS value, the better the modelled gravity field (with an isostatically compensated topography) fits the observed gravity field.

Figure 4.1a shows a high RMS values in the bottom right (high mantle density and low crustal density) and low RMS (better fits) in the top left (low mantle density and high crustal density). Note that the RMS increases for an increasing density contrast ($\rho_m - \rho_c$). The performance of the Airy model is dependent on

the density contrast, not only the mantle density or crustal density. Figure 4.1b shows the dependence on the density contrast and the zero-elevation crustal thickness (H_0). The solutions are robust to a change in density contrast (the RMS values stay approximately the same) but are sensitive to a change in zero-elevation crustal thickness. The higher this value, the better the fit, meaning that the gravity field is fitting better by only considering topography and placing the counteracting root deeper in the mantle. The deeper the root, the lower the counterbalancing effect of the crustal root, resulting in a more dominant topography contribution in the modelled gravity field. In order to stay within the realm of values found by literature, a zero-elevation crustal thickness of 100 km is considered for the Airy model. This results in a minimum crustal thickness below Hellas Basin of approximately 70 km and a maximum crustal thickness under Olympus Mons of approximately 200 km. These values are high, but within the crustal thickness range found by other research (e.g. (Neumann et al., 2004; Wieczorek, 2015; Goossens et al., 2017; McGovern et al., 2002)).

The Airy gravity field assuming a zero-elevation crustal thickness of 100 km, a crustal density of 2900 kg/m^3 and a mantle density of 3550 kg/m^3 is presented in Figure 4.2.

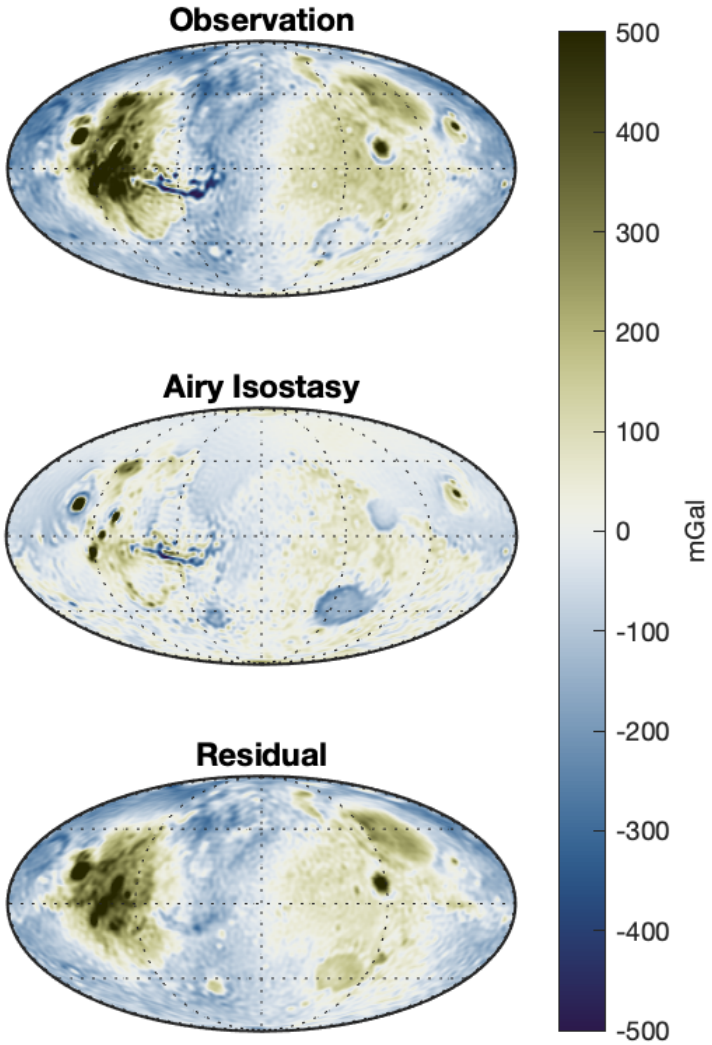

Figure 4.2: Top: observed gravity field (R-component of gravity vector). Middle: gravity field of the topography compensated with Airy isostasy, assuming a zero-elevation crustal thickness of 100 km, a crustal density of 2900 kg/m^3 and a mantle density of 3550 kg/m^3. Bottom: Airy isostasy gravity field subtracted from the observed gravity field to obtain a gravity field representative of the lower layers. The colorbar has been clipped at -500 and 500 mGal. All images are in Mollweide projection with a central meridian of 0 ° longitude. Spherical harmonic degrees 2-90 (with 95% of C_{20} removed) are used.

Figure 4.2 shows that the gravity field due to Airy isostasy is small compared to the observations, having a limited impact on the residual gravity field where the crustal contributions are removed. The Tharsis volcanoes show gravity highs in the Airy plots, even though the crustal root below is counteracting this force. Since the main interest of this research is on the long-wavelength features, an Airy crustal reduction is also computed for spherical harmonic degrees 2-3 and 2-5. Moreover, the crustal dichotomy (degree $n = 1$) is removed from the topography since the focus is on the Tharsis region. The topographies and crustal depths are presented respectively in Figure 4.3a and 4.3b.

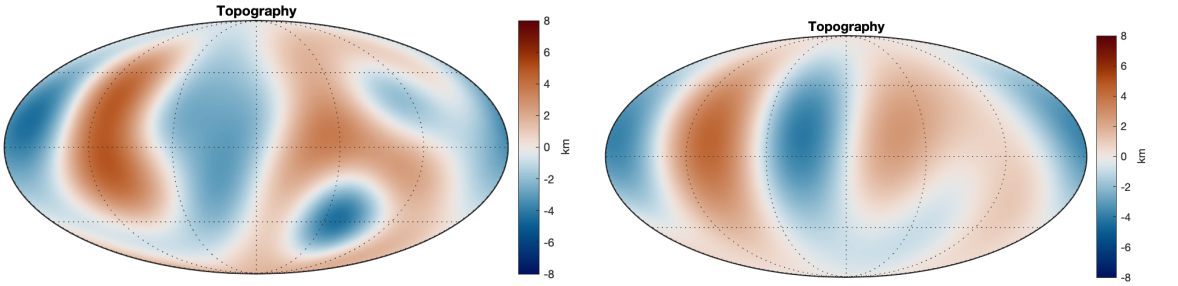

(a) Martian topography at spherical harmonic degrees 2-5 (left) and 2-3 (right). The colorbar has been clipped at -8 and 8 km. The images are in Mollweide projection with a central meridian of 0 ° longitude. The crustal thickness dichotomy ($n = 1$) has been removed.

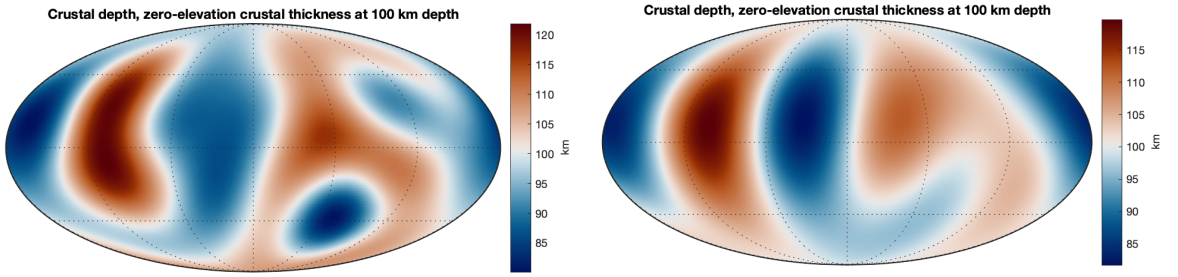

(b) Crustal depths for an Airy model assuming a zero-elevation crustal thickness of 100 km, a crustal density of 2900 kg/m^3 and a mantle density of 3550 kg/m^3. At spherical harmonic degrees 2-5 (left) and 2-3 (right).

Figure 4.3: Observed topography and calculated Airy root depths. The images are in Mollweide projection with a central meridian of 0 ° longitude. The crustal thickness dichotomy ($n = 1$) has been removed.

Figure 4.3 shows a clear topographic high at the Tharsis region; the Tharsis bulge. Moreover, Hellas Basin is clearly visible in degrees 2-5 (the blue circular dots on the Soutern Hemisphere), the effect of this feature is reduced when considering only degrees 2 and 3. The contribution of this topography (and the crustal roots) to the gravity field can now be calculated with the GSH code. The results are depicted in Figure 4.4.

The residuals presented in Figure 4.4 show the resulting gravity field after crustal reduction. Note that this field is due to the mantle, as the signals of degrees 1 to 10 are likely not caused by flexure (Mussini, 2020). So, the Airy isostasy should take into account most of the the long wavelength topographic and gravity features of the crust. The residuals should be allocated to variations in deeper layers. Besides the gravity field, the areoid after crustal reduction is presented in Figure 4.5.

In Figure 4.5, the Tharsis bulge, Tharsis trough and antipodal areoid high are visible. It can be seen that small effects of Hellas Basin and Utopia Planitia are visible for spherical harmonic degrees 2-5. If the spectrum is set to degrees 2-3, the effects are almost completely removed. Moreover, the areoid reaches higher values when considering degrees 2-5 (note that the colorbar has a higher maximum). In addition, the results of the observed gravity field of 4.4 show more variations in at the antipodal of Tharsis, whereas the areoids show a more smoothened areoid peak at that location. In the following section, density anomalies are put in the mantle to determine whether the gravity field presented in Figure 4.5 can be modelled by an anomaly.

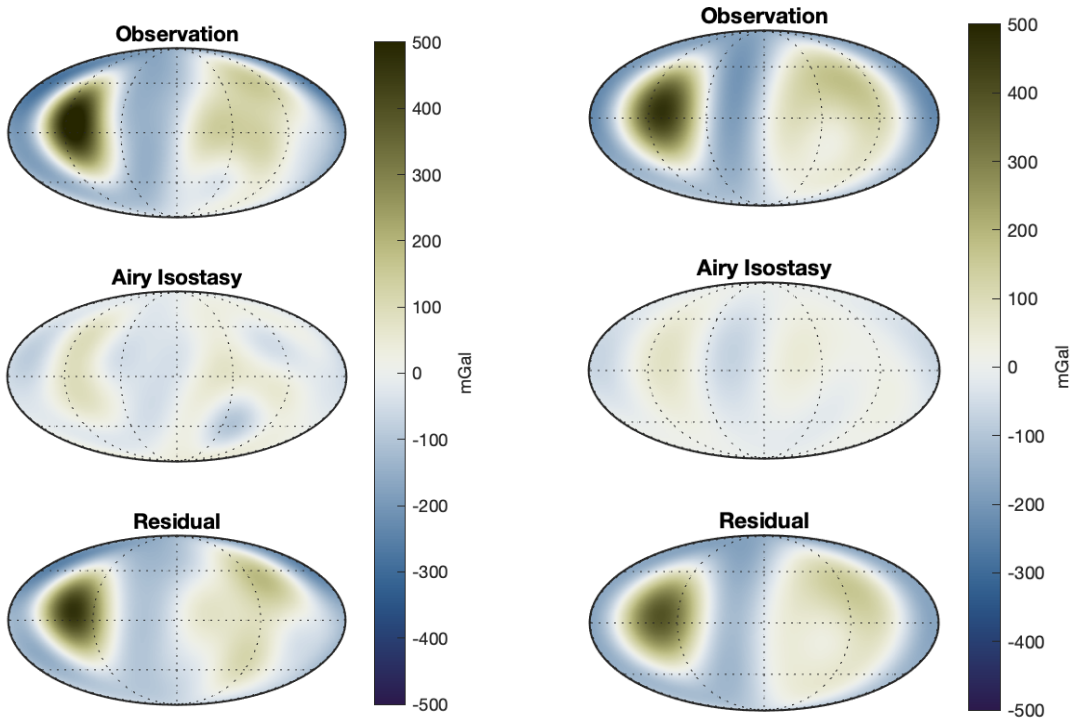

(a) Spherical harmonic degrees 2-5.

(b) Spherical harmonic degrees 2-3.

Figure 4.4: Top: observed gravity field (R-component of gravity vector). Middle: gravity field of the topography compensated with Airy isostasy, assuming a zero-elevation crustal thickness of 100 km, a crustal density of 2900 kg/m^3 and a mantle density of 3550 kg/m^3. Bottom: Airy isostasy gravity field subtracted from the observed gravity field to obtain a gravity field representative of the lower layers. The hydrostatic flattening (C_{20}) is removed for 95%. The colorbar has been clipped at -500 and 500 mGal. All images are in Mollweide projection with a central meridian of 0 ° longitude.

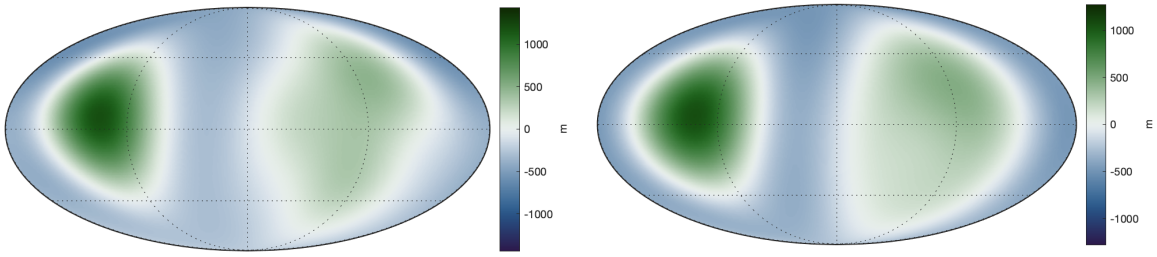

(a) Spherical harmonic degrees 2-5.

(b) Spherical harmonic degrees 2-3.

Figure 4.5: Areoids (in meters) after crustal reduction of an Airy compensated crust with a zero-elevation crustal thickness of 100 km, a crustal density of 2900 kg/m^3 and a mantle density of 3550 kg/m^3. The hydrostatic flattening (C_{20}) is removed for 95%. Both images are in Mollweide projection with a central meridian of 0 ° longitude. The lower limit of the colorbar is manually set to the negative of the maximum observed areoid.

4.2. DENSITY ANOMALIES IN THE MANTLE

In order to set up the optimization code that searches for best-fitting solutions, a robustness study was performed. Those results are briefly discussed in Section 4.2.1. In the sections that follow, the results to models DA-S, DA-A and DA-CMB are presented.

4.2.1. ROBUSTNESS

The four parameters (MaxPeak, Peakratio, Peakzero and Zerozero) are determined in the gravity field that is computed for a specific density anomaly. The settings of the anomaly have an effect on those parameters and its robustness is mapped (See Figure 4.6). Figure 4.6a shows the value of the parameters as a function of the anomaly thickness and the density of the anomaly at a constant depth and lateral size. Figure 4.6b presents the parameters as a function of the lateral (longitude) size and the depth of the anomaly for a constant density and thickness. Note that the heat maps do not represent whether the model is fitting well to the observations or not, it is just showing the absolute values of the four established parameters and how these values change as a function of the variables on the axis.

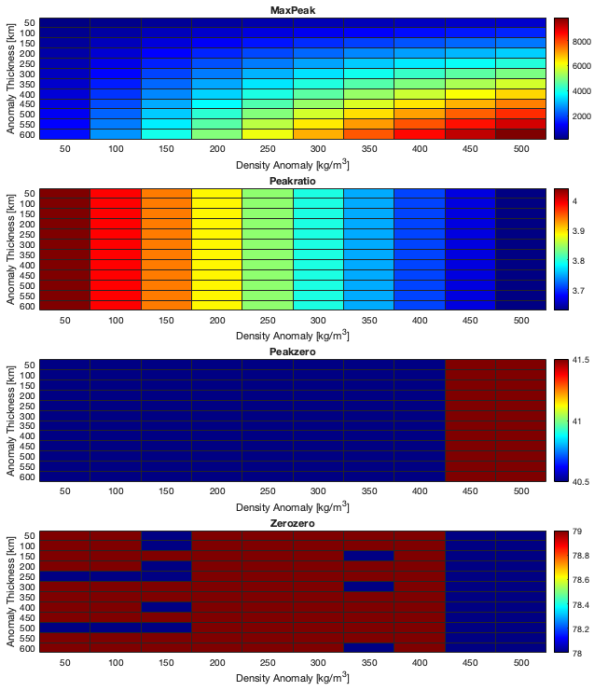

(a) Robustness as a function of the density and thickness of the anomaly. A constant depth of 500 km and a constant lateral longitude size of 25 degrees with respect to center have been assumed.

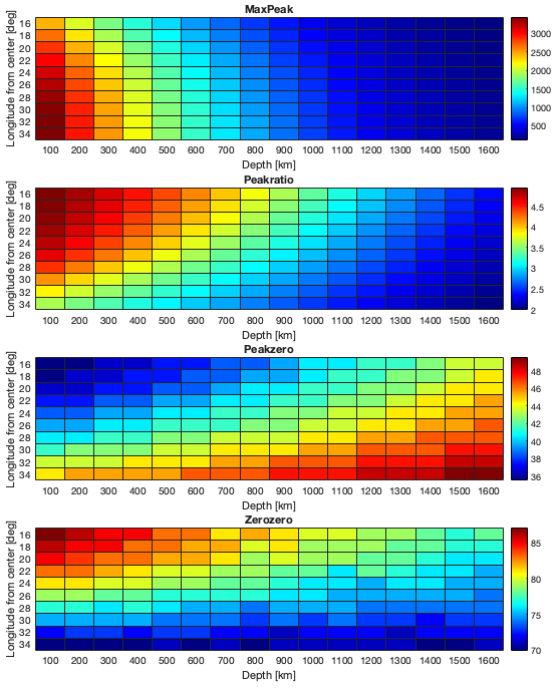

(b) Robustness as a function of the depth and longitudinal size (to both sides of the center) of the anomaly. A constant density of 200 kg/m^3 and a constant thickness of 200 km have been assumed.

Figure 4.6: Robustness study for the Maxpeak, Peakratio, Peakzero and Zerozero fitting parameters.

Looking at Figure 4.6a, Peakratio shows a change when the density is adjusted, but is completely stable for a change in anomaly thickness. Peakzero and Zerozero are geometrical distances in the gravity field and show only two values. The only dependence upon the variables that can be determined is that both change when the density of the anomaly reaches a certain value (450 kg/m^3) for this configuration. Similar to the peakratio, no dependence on the thickness of the anomaly is observed. MaxPeak, the maximum gravitational potential, shows an increase when either the thickness or the density of the anomaly is increased. Figure 4.6b shows that all parameters are dependent on the (longitude) size of the anomaly and at which depth it is located. The MaxPeak and Peakratio parameter shows that at larger depths (deeper than 1200 km), the size of the anomaly does not matter anymore (the dependence disappears). This is an effect of assuming a density of 200 kg/m^3, which effects are not significant anymore when placed at those depths.

Based on this robustness study, the search-code first looks at latitude longitude sizes to determine the shape of the anomaly since this is not dependent on variations in density and thickness of the anomaly, and also quite robust for a change in depth. The next step optimizes for a thickness. Then, the Peakratio will be

evaluated, if it is higher than the observed Peakratio, the depth will be increased (so the Peakratio will become lower in the next iteration, as shown in Figure 4.6a) or if the Peakratio is too low, the depth will be decreased. Another iteration then starts to see whether a converging solution is found, a solution is converged when all four parameters are within 10 % of the observed value. With this search-code, the results model DA-S are computed, they are presented in the next section.

4.2.2. DA-S

For a density anomaly that is symmetric around the center point, the configuration that yields the lowest RMS spatial error is a density anomaly of 400 kg/m^3 at a depth of 800 km and has a thickness of 100 km. It has a S_{lat} of 30 degrees to both sides of the center C_a and an S_{lon} of 32 degrees to both sizes of C_a. The result is presented in Figure 4.7a. The second best-fitting converged solution is shown in Figure 4.7b.

Table 4.1: Configuration settings of the solutions found by the search code for the DA-S Model.

$\Delta\rho$ [kg/m^3]	Depth D_a [km]	Thickness T_a [km]	Center Anomaly C_a	$S_{lon,left}$,$S_{lon,right}$	$S_{lat,up}$,$S_{lat,down}$	RMS [m]	Converged
20	400	500	[110°W,3°N]	32,32	30,30	231.95	No
50	400	500	[110°W,3°N]	32,32	30,30	109.73	Yes
100	600	300	[110°W,3°N]	32,32	30,30	106.26	Yes
200	800	200	[110°W,3°N]	32,32	30,30	100.05	Yes
400	800	100	[110°W,3°N]	32,32	30,30	92.85	Yes
800	700	100	[110°W,3°N]	32,32	30,30	389.04	No

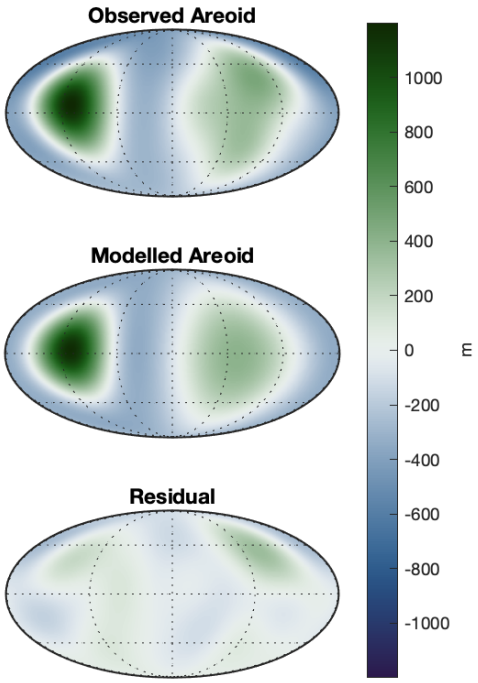

(a) Configuration: anomaly at C_a = [110°W,3°N], $\Delta\rho$ = 400 kg/m^3, depth D_a = 800 km, thickness T_a = 100 km. S_{lon} = 32 degrees (to both sides) and S_{lat} = 30 degrees to both sides of the center. A visualization of the cross-section of the anomaly is given in Appendix B Figure B.1a.

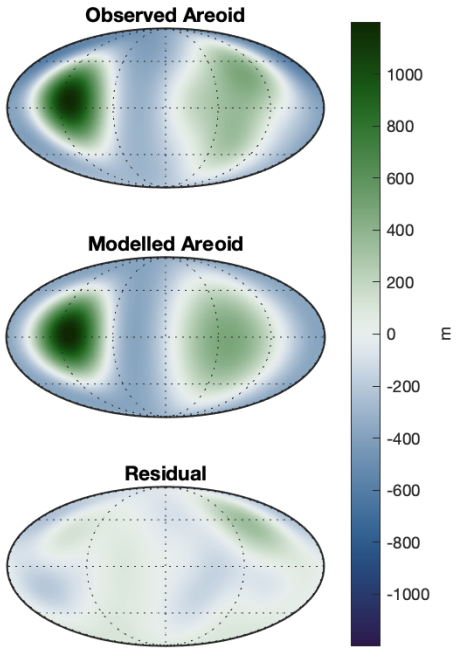

(b) Configuration: anomaly at C_a = [110°W,3°N], $\Delta\rho$ = 200 kg/m^3, depth D_a = 1000 km, thickness T_a = 400 km. S_{lon} = 32 degrees (to both sides) and S_{lat} = 30 degrees to both sides of the center. A visualization of the cross-section of the anomaly is given in Appendix B Figure B.1b.

Figure 4.7: Two best-performing (lowest RMS) converged models. Top: Observed areoid. Middle: modelled anomaly. Bottom: residual (Observed - Model). All images are in Mollweide projection with a central meridian of 0 ° longitude. The lower limit of the colorbar is manually set to the negative of the maximum observed areoid.

The results in Figure 4.7 show that the observed areoid can be modelled quite accurately by placing a single density anomaly in the mantle under Tharsis. The modelled fields have the same overall characteristics as the observed field: a high areoid region above the density anomaly, a negative areoid ring around it, and a second peak (at the antipodal location). The converged models show that the higher the density anomaly, the deeper (or thicker) the anomaly has to be placed. The optimal longitude and latitude sizes show that the

extent of the density anomaly is approximately 60 degrees to both sides. This corresponds to an anomaly of approximately 3000 by 3000 km at a depth of 800 km, meaning it is a huge structure that is much wider than it is thick. The RMS of the best fitting model from Figure 4.7a is depicted in Figure 4.8.

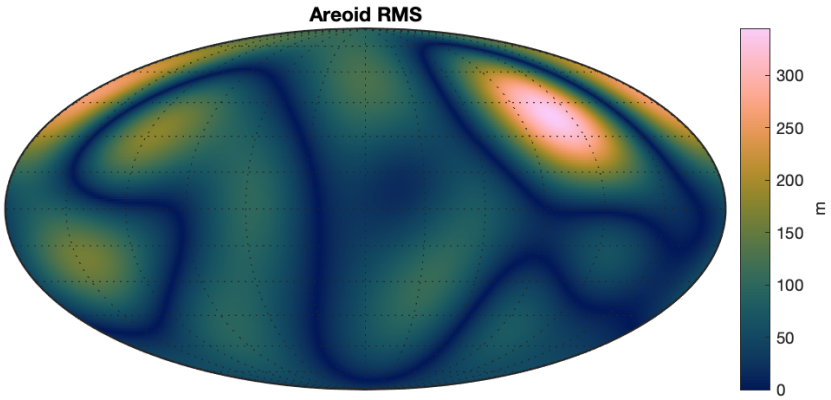

Figure 4.8: RMS of the observed and modelled gravity fields shown in Figure 4.7a. The image is in Mollweide projection with a central meridian of 0 ° longitude.

Note the high RMS at Utopia Planitia (top right), this means this feature is not modelled well by the density anomaly. This is as expected since this feature is not correlated to the Tharsis areoid pattern. This feature is therefore always present in the computed RMS. The results also contain instances in which the search-code did not converge because the 10% was not reached for all fitting parameters, for example for a density anomaly of $\Delta\rho = 20$ kg/m^3 and $\Delta\rho = 800$ kg/m^3. These instances are elaborated upon in Chapter 5. The next section considers a special case of density anomaly, where an asymmetric longitude extent is applied.

4.2.3. DA-A

The previous section showed the results assuming a symmetric anomaly (symmetric in longitudinal and latitudinal direction with respect to the center C_a). Here, a skewed anomaly is considered, the best-fitting solutions are presented in Table 4.2.

Table 4.2: Configuration settings of the solutions found by the search code for the DA-A Model.

$\Delta\rho$ **[kg/m^3]**	**Depth** D_a **[km]**	**Thickness** T_a **[km]**	**Center Anomaly** C_a	$S_{lon,left}$,$S_{lon,right}$	$S_{lat,up}$,$S_{lat,down}$	**RMS [m]**	**Converged**
20	100	500	[110°W,3°N]	30,42	30,30	173.77	No
50	400	500	[110°W,3°N]	28,42	30,30	101.42	Yes
100	600	300	[110°W,3°N]	28,40	30,30	98.06	Yes
200	400	100	[110°W,3°N]	28,42	30,30	98.96	No
400	500	100	[110°W,3°N]	28,40	30,30	193.35	No
800	500	100	[110°W,3°N]	28,40	30,30	664.45	No

An important observation to make is that the solutions for 200 and 400 kg/m^3 did not converge while they did in the DA-S study. Several better-fits (lower RMS) were found but the solutions did not converge to those because one of the four parameters was not close enough to the observation. The results for 20, 50 and 100 kg/m^3 do show improved RMS values, this indicates that the observation is modelled better with a skewed anomaly compared to a symmetric one. In Chapter 5, the downsides of the search-code and why it does not always converge to solutions with a lower RMS is elaborated upon. A visualization of the effect of a skewed anomaly is presented in Figure 4.9.

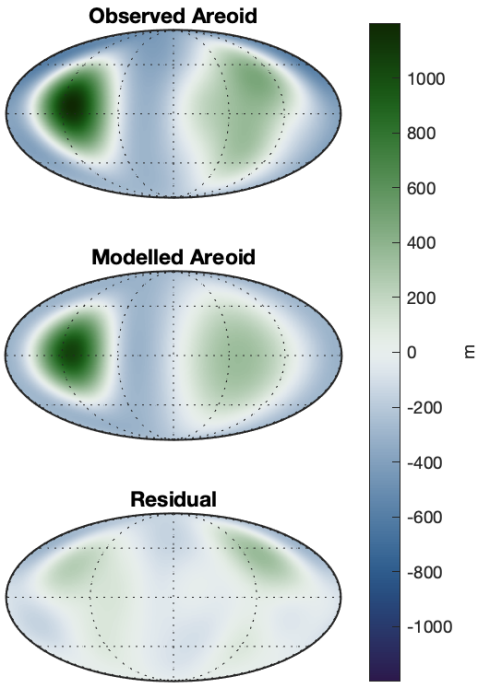

(a) Configuration: anomaly at C_a = [110°W,3°N], $\Delta\rho$ = 100 kg/m^3, depth D_a = 600 km, thickness T_a = 300 km. S_{lon} = 32 degrees (to both sides) and S_{lat} = 30 degrees to both sides of the center. A visualization of the cross-section of the anomaly is given in Appendix B Figure B.1c.

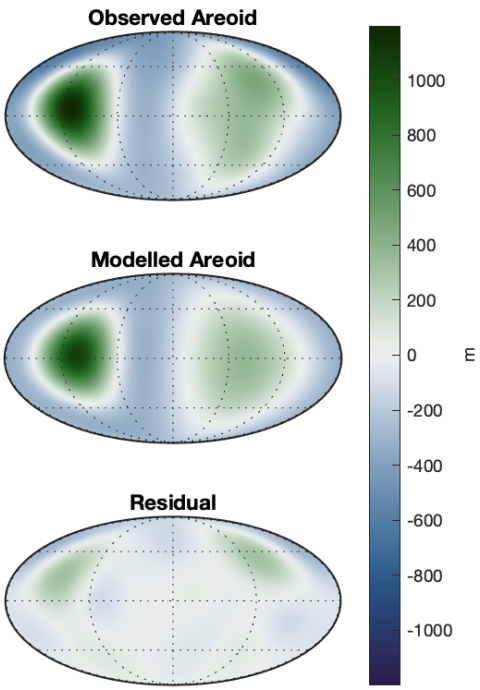

(b) Configuration: anomaly at C_a = [110°W,3°N], $\Delta\rho$ = 100 kg/m^3, depth D_a = 600 km, thickness T_a = 300 km. S_{lon} = 28 to the left and 40 to the right and S_{lat} = 30 degrees to both sides of the center. A visualization of the cross-section of the anomaly is given in Appendix B Figure B.1d.

Figure 4.9: Comparison of the converged 100 kg/m^3 solution of the DA-S and DA-A model. The images are in Mollweide projection with a central meridian of 0 ° longitude. The lower limit of the colorbar is manually set to the negative of the maximum observed areoid.

Figure 4.9a uses a symmetric anomaly where the size spans from -32 to 32 degrees with respect to the center of the anomaly. The asymmetric anomaly presented in 4.9b spans from -28 to 40 degrees, so the right side of the anomaly is stretched more than the left side. This can also be seen in the plots, especially in the white line (0m areoid contour) around Tharsis. The right side of this zero-contour matches the observations better for the asymmetric anomaly compared to the symmetric one. Although the the change are minimal, these results show that it is important to consider the lateral extent as fitting parameter when modelling such large gravity anomalies. As is evident from Tables 4.2 and 4.1, solutions were found primarily in the top and middle mantle (down to 1000 km), depending on the density of the anomaly. No converged solutions were found for anomalies below a depth of 800 km. This result would rule out the possibility of structures - similar to the LLSVPs on Earth - being the main contributor to the observed Tharsis areoid bulge. Besides, the results indicate that for anomalies at depth below 600 km, density anomalies of at least 100 kg/m^3 are required. Although the observed Tharsis bulge is probably not due to deep mantle structures, the effect of CMB topography undulations should be investigated. This is because the density of the core is much higher than the density of the mantle, so small upward deflections of the CMB into the mantle could already cause significant gravity variations. The results of this study are presented in Section 4.2.4.

4.2.4. DA-CMB

Although no density anomalies have been found in the DA-A and DA-S models that have an origin below 800 km depth, there is another potential contributor to the observed areoid high; the topography of the CMB. Two CMB deflection models have been tested, both of which are outer cases in the expected limits of the Martian core (Michel and Forni, 2011; Knapmeyer, 2011). The assumed core densities have been obtained from Steinberger et al. (2010). In both case the crust has been assumed to be 3550 kg/m^3 homogeneously throughout the mantle.

1. DA-CMB-1: CMB at a depth of 1750 km. The core density is approximately 7000 kg/m^3, meaning that the density anomaly with respect to the crust is 3450 kg/m^3.
2. DA-CMB-2: CMB at a depth of 2000 km. The core density is approximately 8400 kg/m^3, meaning that the density anomaly with respect to the crust is 4850 kg/m^3.

A density anomaly with $\Delta\rho = \rho_{core} - \rho_m$ is placed on top of the CMB to imitate a CMB undulation. The RMS of the modelled areoid is calculated as a function of the CMB undulation. Figure 4.10 visualizes the behavior of both models.

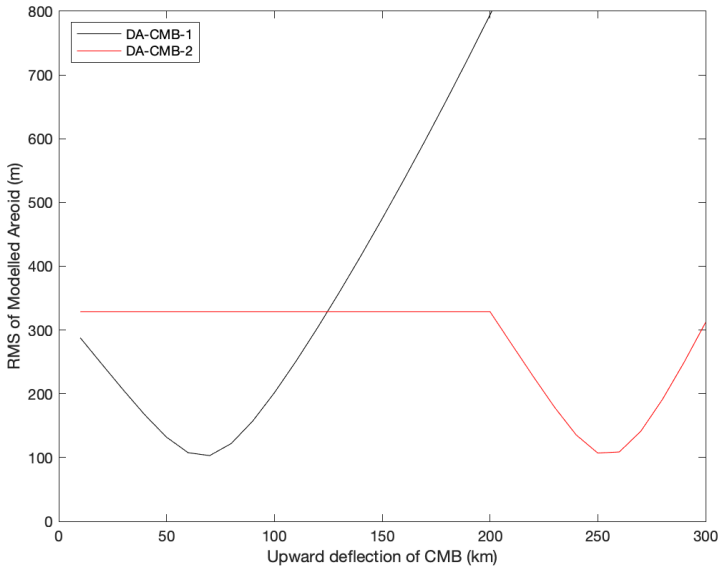

Figure 4.10: RMS of the modelled areoid as a result of an upward deflection of the CMB for two different core configurations (DA-CMB-1 and DA-CMB-2). The best-fitting solution is characterized by the lowest RMS, so at 70 km for Model 1 and 250 km for Model 2. The RMS-axis has been manually cut-off at 800 m, Model 1 keeps on increasing for higher deflections.

From Figure 4.10 can be induced that for DA-CMB-1, an upward deflection of 70 km would cause the best-fitting model. For DA-CMB-2, this is 250 km. Since these are two extreme cases for the core radius, core models from other studies would probably between DA-CMB-1 and DA-CMB-2 and therefore the required CMB undulations is between 70 km and 250 km. Table 4.3 lists the configuration settings and RMS of both of the solutions.

Table 4.3: Configuration settings of the solutions found by the search code for the DA-CMB Model.

$\Delta\rho$ [kg/m^3]	**Depth** D_a **[km]**	**Thickness** T_a **[km]**	**Center Anomaly** C_a	$S_{lon,left}$,$S_{lon,right}$	$S_{lat,up}$,$S_{lat,down}$	**RMS [m]**	**Converged**
DA-CMB-1	1680 to 1750	70	$[110°W, 3°N]$	32,32	30,30	103.06	Yes
DA-CMB-2	1750 to 2000	250	$[110°W, 3°N]$	32,32	30,30	107.09	Yes

In the RMS error plots presented in Figure 4.11 it can be seen that those configurations both model the gravity in the Tharsis region quite well (as is evident from the low RMS values in this region). DA-CMB-2 shows a slightly higher peak at the Tharsis location compared to DA-CMB-1. The RMS high at Utopia Planitia is in both cases the dominant contributor to the overall RMS value.

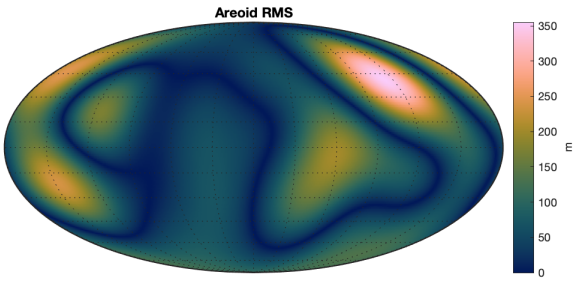

(a) DA-CMB-1. A visualization of the cross-section of the anomaly is given in Appendix B Figure B.1e.

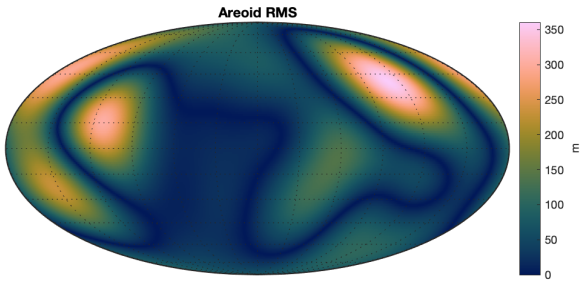

(b) DA-CMB-2. A visualization of the cross-section of the anomaly is given in Appendix B Figure B.1f.

Figure 4.11: RMSE of the observed gravity field and the models (DA-CMB-1 and DA-CMB-2). The images are in Mollweide projection with a central meridian of 0 ° longitude. A higher RMS means a higher deviation from the observed gravity field.

4.2.5. SUMMARY OF DA-MODEL RESULTS

The DA-S Models showed that the observed gravity bulge at the Tharsis region can be modelled by a single density anomaly located at a center of 70 degrees longitude and 3 degrees latitude. Not only above this density anomaly, but also in the remainder of the gravity field, do the models perform well and indicate a low RMS. An exception is Utopia Planitia (45 degrees North, 117 degrees East), which dominates the RMS field when the Tharsis region is modelled well. The DA-A models presented several solutions that create even better fitting gravity field by enabling an asymmetric density anomaly. This result shows that the mass distribution is not centered precisely radially below the areoid high. For some density anomalies, for example $\Delta\rho = 20$ kg/m^3 and $\Delta\rho = 800$ kg/m^3, the solutions did not converge, meaning that one of the four parameters (MaxPeak, Peakratio, Zerozero or zeropeak) was not close enough to that of the observed gravity field. The DA-CMB models presented an approximation of the deflection of the CMB that is required to model the observed areoid. A CMB undulation of 70 km was found for a core starting at a depth of 1750 km and an undulation of 250 km is required for a core with a smaller radius (starting at a depth of 2000 km). Those undulations have a lateral size of approximately 60 by 60 degrees, spanning an area of approximately 1/18 of the CMB surface.

4.3. BOUNDARY DEFORMATIONS

In this section, the results of the Boundary Deformation (BD) study are presented. The gravity fields that are the results of a density anomaly (and their consequential boundary deformations) are computed in SFEC. Firstly, the solutions to the Models BD-Grav-FULL and BD-Grav-SC will be elaborated upon in Sections 4.3.1 and 4.3.2. Subsequently, the dynamic topography is added as an additional constraint in Models BD-Hybrid-UC and BD-Hybrid-Superplume. The results of which are discussed in Section 4.3.4 and 4.3.5 respectively.

This chapter contains full heat map results to enable the comparison between models based on the raw data heat maps. In this way, one can determine where the best-fitting solutions did shift to, and what happened with the best-fitting solutions of the baseline as well. The interpretation is relatively straightforward; the higher the value in the heat map, the better that solution. In Appendix D, the relationships between baseline and model are presented in a different matter, which may provide the reader with additional insights.

4.3.1. BD-GRAV-FULL

For this model, a baseline is established with a density anomaly of 400 km thick, a lithosphere of 100 km, spherical harmonic degrees 2-5 and viscosity profile 1. The results are shown in Figure 4.12.

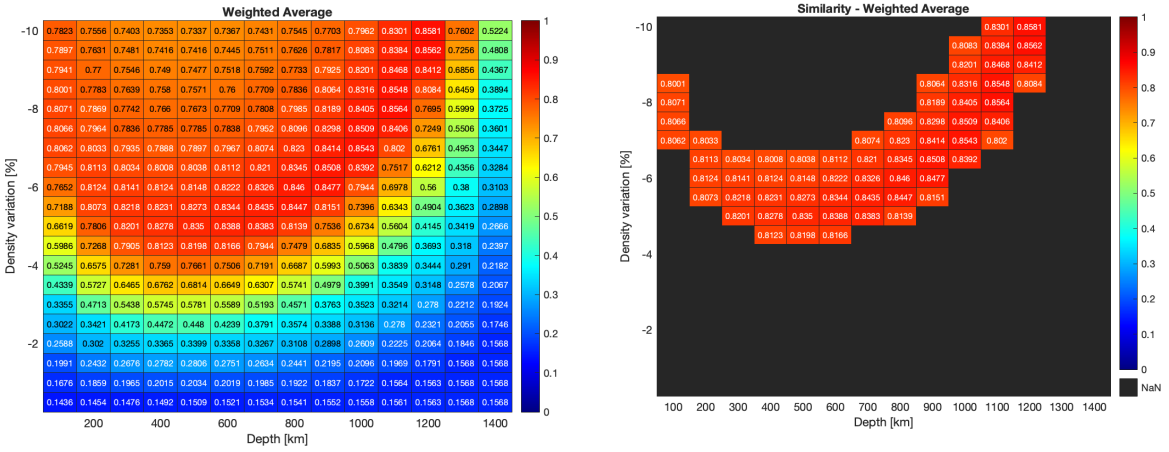

(a) Heat map of the total (weighted) similarities of the BD-Grav-FULL Baseline.

(b) Selection of the best-fitting results (similarity above 0.8). The similarities below 0.8 have been set to NaN.

Figure 4.12: The closer the values are to one, the better the fit. The horizontal axis indicates at which depth (D_a) the anomaly starts (so first column starts at a depth of 100 km). The vertical axis presents the density variation $\Delta\rho/\rho_m * 100\%$. The anomaly is centered at $C_a = [110°W, 3°N]$ and has a thickness (T_a) of 400 km. Lateral sizes: $S_{lon,left} = 24$, $S_{lon,right} = 24$, $S_{lat,down} = 30$ and $S_{lat,up} = 41$ degrees.

From an initial study into the potential regime of solutions - briefly presented and discussed in Figure 2.19 and Section 2.4.4 - it was determined that positive density variations do not result in models that have a

high similarity with the observations. This is in contrast with the (positive density anomaly) solutions found by the DA-models, it shows that taken into account the boundary deformations already has a significant impact on the set of solutions. The negative density anomalies are able to produce a positive areoid by pushing up the surface topography and attracting the CMB-topography, these boundary deformations are taken into account in the total gravity field.

Figure 4.12 shows that the similarity depends on the density variation as well as the depth. There is a band visible in which the best-fitting solutions are located (Figure 4.12b). For low depths (< 200 km), these best fitting solutions are for a density variation of approximately -7 %. For depths from 300 to approximately 800 km, the density variation is around -6 %. For deeper layers, the required density variation increases again.

It should be noted that there are many solutions in the range of similarities from 0.84 to 0.86. The best fitting configuration is a density anomaly of -10 % (corresponding to -355 kg/m^3 with respect to the surrounding mantle) at a depth of 1200 km, so with a thickness of 400 km this anomaly is from 1200 km down to 1600 km depth. This solution has a total similarity of 0.8581. The resulting topographies and areoid fields are presented in Figure 4.13.

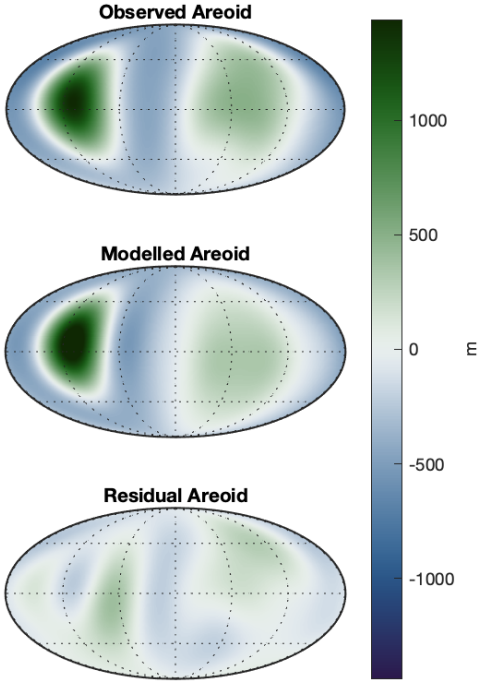

(a) Observed, modelled and residual areoid. 95% of C_{20} is removed. The lower limit of the colorbar is manually set to the negative of the maximum observed areoid.

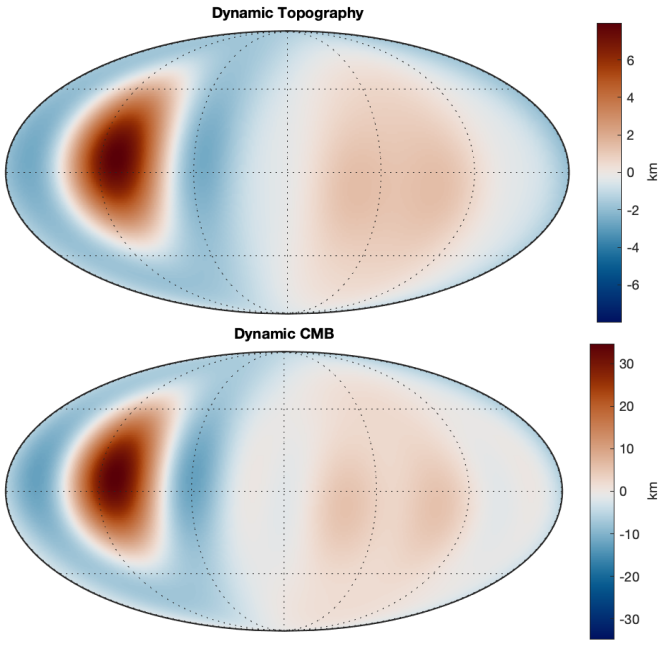

(b) Dynamic topography (due to stresses on the surface layer) and the dynamic CMB deflection as a result of the stresses on the CMB. The lower limit of the colorbar is manually set to the negative of the maximum observed topography and CMB respectively.

Figure 4.13: Best fitting configuration with a density variation of -10 % at a depth of 1200 km down to 1600 km. All images are in Mollweide projection with a central meridian of 0 ° longitude. A visualization of the cross-section of the anomaly is given in Appendix B Figure B.2a.

Figure 4.13b shows that the deflection of the CMB is slightly more than 30 km. For the other boundary, the topography, the dynamic deformation caused by the density anomaly is approximately 7 km. The effect of the density anomaly on the CMB is larger because it is closer that the CMB compared to the surface (the anomaly from 1200 km down to 1600 km depth is almost on the CMB, which starts at 1800 km depth). In essence, both the CMB and surface deflections contribute to the modelled areoid. However, as the surface is shallow and the CMB lies deep in the planet, the effect of the surface topography deflections is larger for similar deflections. In order to characterize the behaviour of the density anomalies and their resulting boundary deformations, the impact of viscosity, spectral resolution, lithosphere thickness and the thickness of the anomaly have been investigated. The results are presented in the sections below.

ANOMALY THICKNESS

The results from the DA-models already indicated that the thickness T_a of the anomaly has a significant impact on the modelled areoid. In this section, the density anomaly is modelled with a thickness of 200, 300, 400, 500 and 600 km to determine the sensitivity of the solutions to T_a. The heat maps of the similarities are depicted in Figure 4.14. A clear relationship is visible from Figures 4.14a to 4.14e; the set of best-fitting solutions shifts downwards in the heat maps. This indicates that a higher thickness implies that a lower density variation with respect to the surrounding mantle is required. An anomaly of 600 km at a depth of 400 km obtains high similarities at a density variation of approximately -4%, corresponding to an absolute density difference of 142 kg/m^3. Such a density anomaly is more likely to be present in the mantle than one with a higher density variation (e.g. -8%). This is discussed in more detail in Chapter 5.

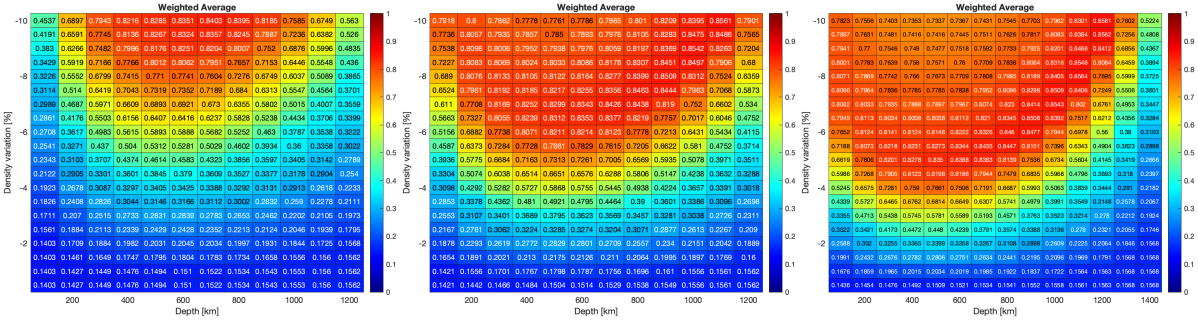

(a) 200 km anomaly thickness (b) 300 km anomaly thickness (c) 400 km anomaly thickness (baseline)

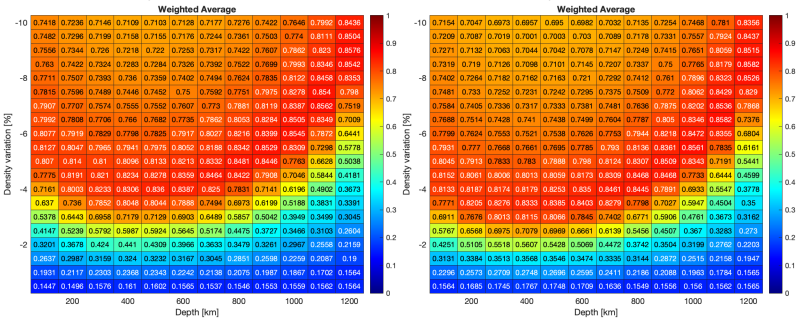

(d) 500 km anomaly thickness (e) 600 km thickness

Figure 4.14: Heat map of the total (weighted) similarities of the BD-Grav-FULL varying the anomaly thickness. The closer the values are to one, the better the fit. The horizontal axis indicates at which depth (D_a) the anomaly starts (so first column starts at a depth of 100 km). The vertical axis presents the density variation $\Delta\rho/\rho_m * 100\%$. The anomaly is centered at $C_a = [110^\circ W, 3^\circ N]$and has lateral sizes of: $S_{lon,left} = 24$, $S_{lon,right} = 24$, $S_{lat,down} = 30$ and $S_{lat,up} = 41$ degrees.

VISCOSITY PROFILE

In Section 2.4.1, three viscosity profiles were proposed. Viscosity profile 1 has been used for the results of the baseline (Figure 4.12). The same solutions have been generated for viscosity profiles 2 (Figure 4.15b) and 3 (Figure 4.15c).

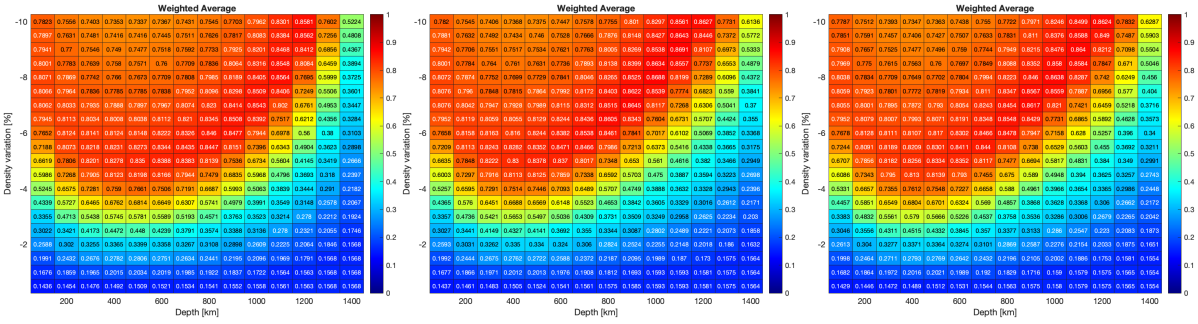

(a) Viscosity Profile 1 (baseline) (b) Viscosity Profile 2 (c) Viscosity Profile 3

Figure 4.15: Heat map of the total (weighted) similarities of the BD-Grav-FULL varying the viscosity profile. The closer the values are to one, the better the fit. The horizontal axis indicates at which depth (D_a) the anomaly starts (so first column starts at a depth of 100 km). The vertical axis presents the density variation $\Delta\rho/\rho_m * 100\%$. The anomaly is centered at $C_a = [110^\circ W, 3^\circ N]$ and has a thickness (T_a) of 400 km. Lateral sizes: $S_{lon,left} = 24$, $S_{lon,right} = 24$, $S_{lat,down} = 30$ and $S_{lat,up} = 41$ degrees.

The heat maps presented in Figure 4.15 look similar. The similarities in the best-fitting regime (indicated high similarity) from a depth of 800 km down to 1200 km increase slightly when using profile 2 instead of profile 1. The effect of increasing the viscosity of the top layers (profile 3 in comparison with profile 2) is also minimal. These results indicate that the solutions are not sensitive to a change in viscosity profile.

SPECTRAL RESOLUTION

The effect of the modelled spectral resolution is researched in this section. The results are presented in Figure 4.16. The primary change in the set of solutions that can be observed is that the band with high-similarity solutions gets smaller when decreasing the spectral resolution (from SH 2-5 to SH 2-3). This results in a better defined set of solutions that is able to model the observed areoid well in SH 2-5, but also in SH 2-3. The overall similarities decrease slightly when decreasing the spectral resolution (e.g. the solutions at a depth of 1000 km and -8 % variation is 0.8405 for SH 2-5, 0.8402 for SH 2-4 and 0.8192 for SH 2-3).

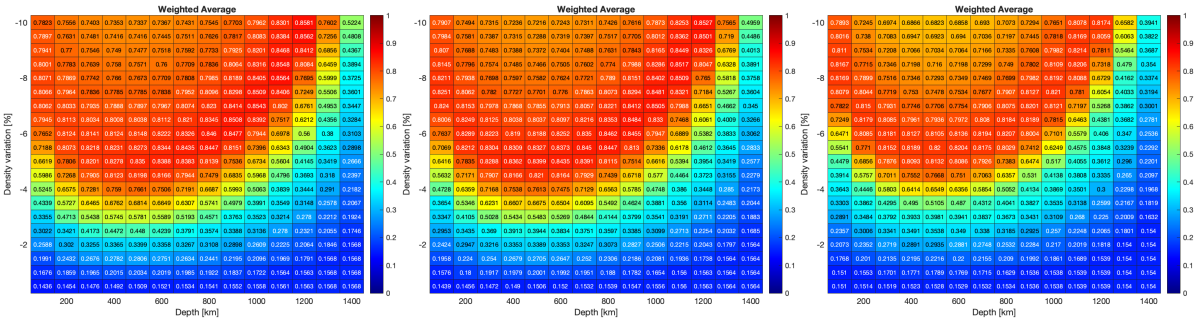

(a) Spherical harmonic degrees 2-5 (baseline) (b) Spherical harmonic degrees 2-4 (c) Spherical harmonic degrees 2-3

Figure 4.16: Heat map of the total (weighted) similarities of the BD-Grav-FULL varying the spectral resolution. The closer the values are to one, the better the fit. The horizontal axis indicates at which depth (D_a) the anomaly starts (so first column starts at a depth of 100 km). The vertical axis presents the density variation $\Delta\rho/\rho_m * 100\%$. The anomaly is centered at $C_a = [110°W, 3°N]$ and has a thickness (T_a) of 400 km. Lateral sizes: $S_{lon,left} = 24$, $S_{lon,right} = 24$, $S_{lat,down} = 30$ and $S_{lat,up} = 41$ degrees.

The observed behaviour, the shrinking band of best-fitting solutions, can be used as an additional constrain. If the configuration has to be representative of features of the wavelength corresponding to degree 3,4 and 5 then it should indicate a high similarity in all three plots of Figure 4.16. Because the Tharsis bulge is strongly present in spherical harmonics degree 2-3, the solution should fit well in the regime as well as in degrees 2-5 (and 2-4).

LITHOSPHERE THICKNESS

The lithosphere in SFEC is modelled as a highly viscous shell. The thicker this shell, the less it will deform as a result of the same stress. The effect of the lithosphere thickness on the set of solutions is presented in Figure 4.17.

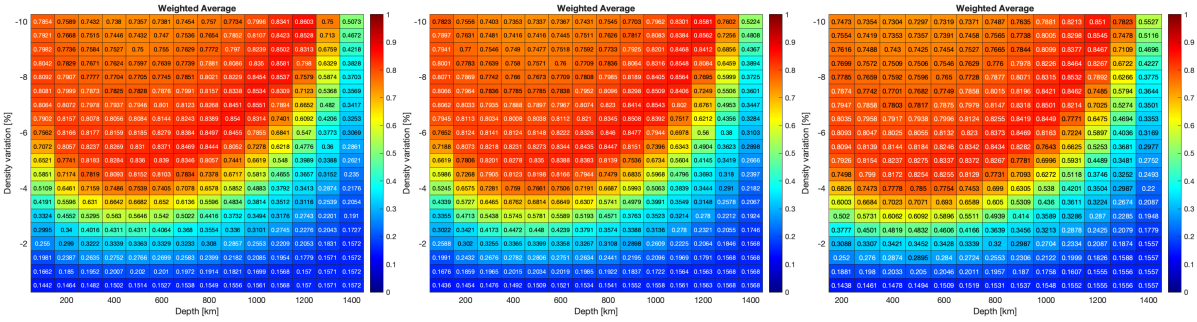

(a) 50 km lithosphere (b) 100 km lithosphere (baseline) (c) 200 km lithosphere

Figure 4.17: Heat map of the total (weighted) similarities of the BD-Grav-FULL varying the lithosphere thickness. The closer the values are to one, the better the fit. The horizontal axis indicates at which depth (D_a) the anomaly starts. The vertical axis presents the density variation $\Delta\rho/\rho_m * 100\%$. The anomaly is centered at $C_a = [110°W, 3°N]$ and has a thickness (T_a) of 400 km. Lateral sizes: $S_{lon,left} = 24$, $S_{lon,right} = 24$, $S_{lat,down} = 30$ and $S_{lat,up} = 41$ degrees.

As can be seen from those solutions, the larger the lithosphere thickness, the smaller the density variation is for shallow layers. For example, the best-fitting solution at a depth of 200 km has a similarity of 0.8166 at -6 % for 50 km lithosphere thickness. A similarity of 0.8124 at -6 % for the baseline and 0.8093 at -6% for a 200 km thick lithosphere. This means that the same density anomaly has less effect (and results in a worse fit) when the lithosphere thickness is increased. It becomes more difficult for the same density anomaly to cause an uplifted surface topography. Note that for a lithosphere of 200 km thickness, the depths of the anomaly configurations start at 200 km, immediately below the lithosphere. This is also the reason for the heat map in Figure 4.17c showing one column less (as no density anomaly is be placed at 100 km because it is inside the lithosphere).

4.3.2. BD-GRAV-SC

The deformations of the CMB topography also have an effect on the modelled areoid, as was already shown in the DA-CMB model results. In SFEC, the contribution of the core deformations can be enabled (viscous core) or disabled (completely solid core). The baseline used a viscous core, the effect of using a solid core is shown in Figure 4.18b.

It becomes clear from Figure 4.18 that the closer the density anomaly is located to the core, the more the similarities change with respect to the baseline. This is as expected because the closer an anomaly is to the CMB boundary, the higher the deformations. And consequently, the larger the effect of the CMB undulations is on the areoid. For a solid core, there are no solutions with a similarity above 0.8 for depths of 1200 km and more. For the baseline, there are solutions of 0.85 similarity at a depth of 1200 km (which are partially the result of the CMB undulations).

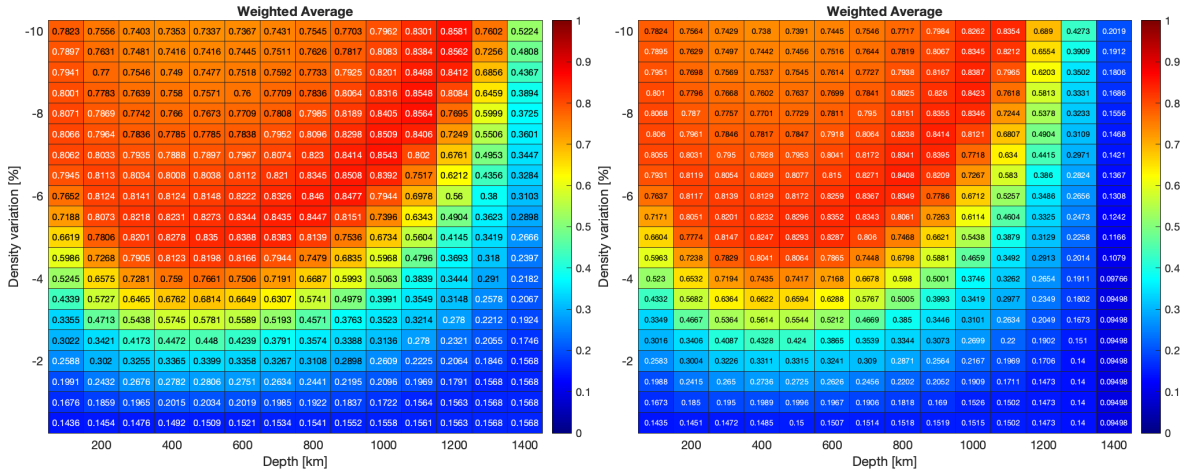

(a) Baseline

(b) Solid Core

Figure 4.18: Heat map of the total (weighted) similarities of BD-Grav-SC. The closer the values are to one, the better the fit. The horizontal axis indicates at which depth (D_a) the anomaly starts (so first column starts at a depth of 100 km). The vertical axis presents the density variation $\Delta\rho/\rho_m * 100\%$. The anomaly is centered at $C_a = [110^\circ W, 3^\circ N]$and has lateral sizes of: $S_{lon,left} = 24$, $S_{lon,right} = 24$, $S_{lat,down} = 30$ and $S_{lat,up} = 41$ degrees.

The BD-Grav-SC model results show that when the Martian core is assumed to be completely solid, the best-fitting configurations shift to a shallower (lower depth) regime. There are no significant observed changes depending on the density of the anomaly.

4.3.3. SUMMARY OF BD-GRAV MODEL RESULTS

The main difference beween the DA-Models and The BD-Grav models is that boundary deformations (due to stresses caused by the density anomalies) have been taken into account in the final calculations of the areoid. The BD-Grav-Full results show that a an anomaly with a higher density than the surrounding mantle is highly unlikely to be the cause of the observed areoid bulge at the Tharsis region. A negative density anomaly fits the observed areoid better, meaning that there is a buoyant force that uplifts the CMB topography and surface topography. The BD-Grav-Full models show a large dependence upon the thickness (T_a) of the anomaly; a larger thickness requires a smaller density variation. A thicker lithosphere makes it more difficult for the den-

sity anomalies to deform the boundaries, dampening the effect of the density anomalies slightly, especially in the shallow layers. The viscosity profiles do not seem to cause a significant change in the set of solutions that is found, the similarities change for some regimes but the best-fitting high similarity solutions are minimally affected. Besides, a decreasing spectral resolution narrows the band of high similarity solutions and could therefore be exploited to narrow down the set of solutions. The BD-Grav-SC model visualized the difference between a solid or viscous core. When assuming a solid core, there is no CMB deformation so this contribution to the modelled areoid vanishes. Because of this, the best-fitting solutions shift to shallower layers.

All in all, for several configurations, the models fit the observed areoid really well. In addition, the robustness in some of the main modelling parameters is determined. However, only this gravitational potential has been considered as reference. As shown in Figure 4.13b, the deflections of the topography can also be taken into account. This can be combined with the observed topography to create an additional constraint. For the BD-Grav Models it was assumed that the topography was completely dynamically supported by the buoyant forces from the density anomaly. In Section 4.3.4, the observed topography is added as an additional constraints, as was discussed in Section 4.1.

4.3.4. BD-HYBRID-UC

The BD-Hybrid-UC models take into account the modelled gravity and topography after placing an upwelling cell (negative density anomaly) inside the mantle. The topography is partially compensated by Airy isostasy, and partially by the dynamic upwelling of the cell. The former component is calculated by subtracting the dynamic topography due to the upwelling from the observed gravity. Note that this could result in a negative isostatically compensated topography, which would result in turn results in an upwards deflected 'Martian Moho'. If this occurs, a thinned crust is observed at this location. Solutions where the crustal thickness becomes negative are geophysically impossible because the crust always has a thickness of zero or higher. Those solutions are removed from the solution space (and depicted with NaN-values in the heat maps). Additional information about the heat maps presented in this chapter can be found in Appendix D. The effect of taking into account an isostatic compensation for the remainder of the topography can be seen in Figure 4.19a.

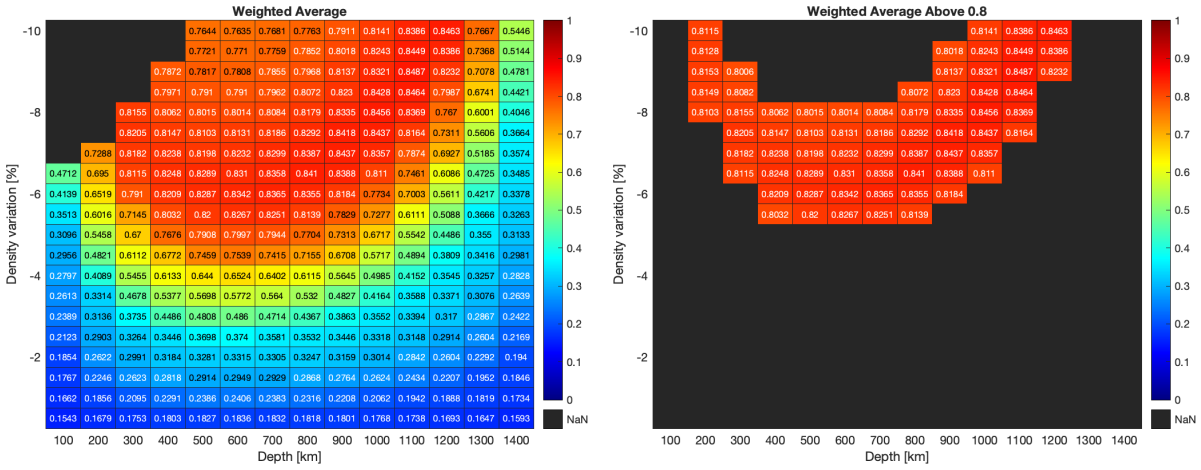

(a) Heat map of the total (weighted) similarities of the BD-Hybrid-UC baseline.

(b) Selection of the best-fitting results (similarity above 0.8). The similarities below 0.8 have been set to NaN.

Figure 4.19: The closer the values are to one, the better the fit. The solutions that result in a negative crustal thickness (assuming a zero-elevation crustal thickness of 100 km) are indicated as NaN-values. The horizontal axis indicates at which depth (D_a) the anomaly starts (so first column starts at a depth of 100 km). The vertical axis presents the density variation $\Delta\rho/\rho_m * 100\%$. The anomaly is centered at C_a = [110°W,3°N] and has a thickness (T_a) of 400 km. Lateral sizes: $S_{lon,left}$ = 24, $S_{lon,right}$ = 24, $S_{lat,down}$ = 30 and $S_{lat,up}$ = 41 degrees.

Figure 4.19a depicts a regime in which there are NaN-values. In this regime, the topography that has to be Airy compensated is negative and too large. The Airy isostatic correction of such negative topographies requires a Martian Moho that is deflected upwards. The NaN regime indicates where the Martian Moho has to be uplifted higher than the topography, which is geophysically impossible. Figure 4.19b shows the solutions that resulted in a similarity higher than 0.8. Note that some solutions at shallow depths are removed when taking into account the topography. For instance. all solutions from Figure 4.19b at a depth of 200 km are not possible anymore when taking into account the topography. Moreover, the values of this BD-Hybrid-UC

baseline changed slightly compared to the BD-grav-Full baseline because the additional contribution (Airy) to the areoid.

The best-fitting configuration occurs for a density variation of -9 % with respect to the surrounding mantle, at a depth of 1100 km (down to 1500 km). The contributions of the dynamic component and the isostatic component are presented in Figure 4.20.

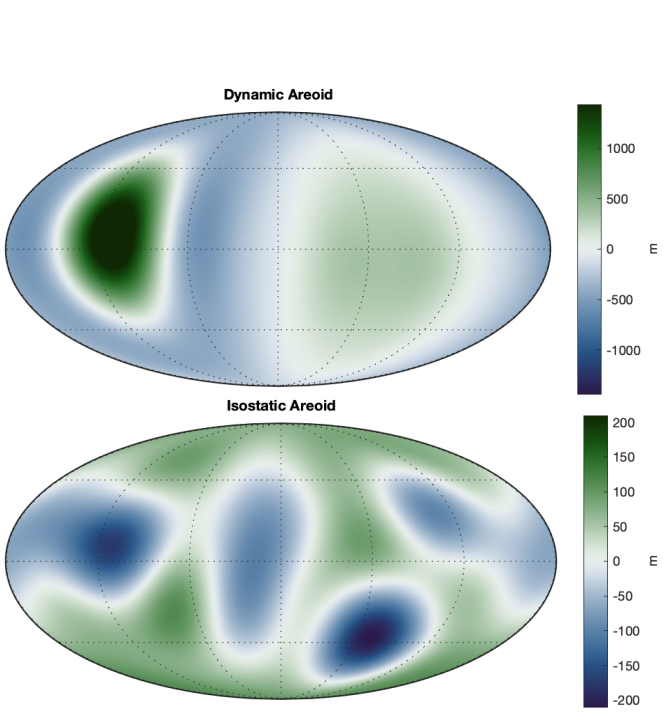

(a) Top: Dynamic component of the areoid field and Bottom: isostatic component of the areoid field. Adding those two components produces the modelled areoid presented in Figure 4.20b. Note the difference in magnitude, the limits of the colorbar of the isostatic component are approximately 6 times smaller than that of the dynamic component.

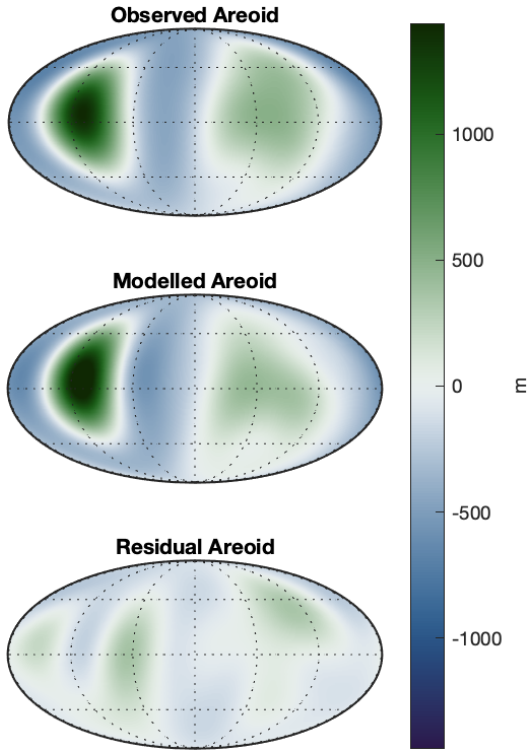

(b) Observed, modelled and residual areoid. The lower limit of the colorbar is manually set to the negative of the maximum observed areoid.

Figure 4.20: Modelling of the areoid, consisting of a dynamic and isostatic (Airy) component. The hydrostatic flattening (95% of C_{20}) is removed. All images are in Mollweide projection with a central meridian of 0 ° longitude. A visualization of the cross-section of the anomaly with respect to Mars is given in Appendix B Figure B.2b.

Figure 4.21 shows that the dynamic topography reaches a peak of approximately 8 km while the observed topography is only 4.5 km. In this case, the dynamic topography is higher than the observed topography at the location of Tharsis, meaning that the topography that is isostatically compensated should actually be negative in that region (visualized in Figure 4.21c). The result is that a small crustal thickness is observed under Tharsis. Although the isostatic topography is significant, the result areoid field is almost negligible with respect to the dynamic areoid. This shows that the dynamic areoid dominates over the airy isostatic areoid. One of the results that was removed because the crustal thickness became negative, is the solution for a density variation of -10 % at a depth of 300 km. The crustal thickness of the best-fitting and the crustal thickness plot of the removed solution are presented in Figure 4.22. A negative crustal thickness is observed at the location of Tharsis in Figure 4.22b, which is the reason this solution is removed. Figure 4.22a shows the crustal thicknesses obtained for the best-fitting solution. The smallest crustal thickness is observed at Hellas Basin. The Tharsis region also has relatively small crustal thicknesses.

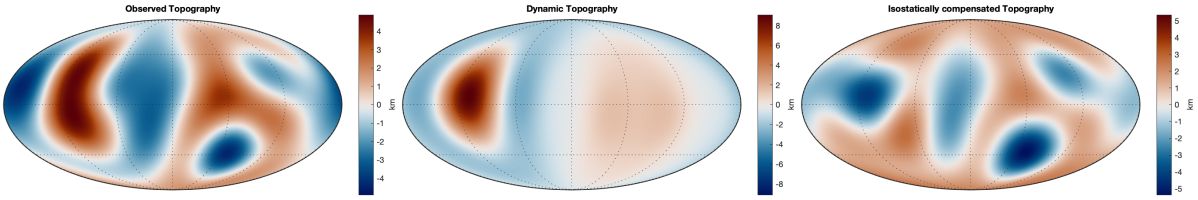

(a) Observed topography, the Martian dichotomy (degree $n = 1$) is removed. The lower limit of the colorbar is manually set to the negative of the maximum observed topography.

(b) Dynamic topography due to uplift by the buoyant density anomaly. The lower limit of the colorbar is manually set to the negative of the maximum observed dynamic topography.

(c) Airy compensated topography (observed minus dynamic topography). The lower limit of the colorbar is manually set to the negative of the maximum Airy compensated topography.

Figure 4.21: Topographies corresponding to the best-fitting model (-9% density variation at a depth of 1100 km). The addition of the dynamic topography and the isostatically compensated topography produces the observed topography. All images are in Mollweide projection with a central meridian of 0 ° longitude.

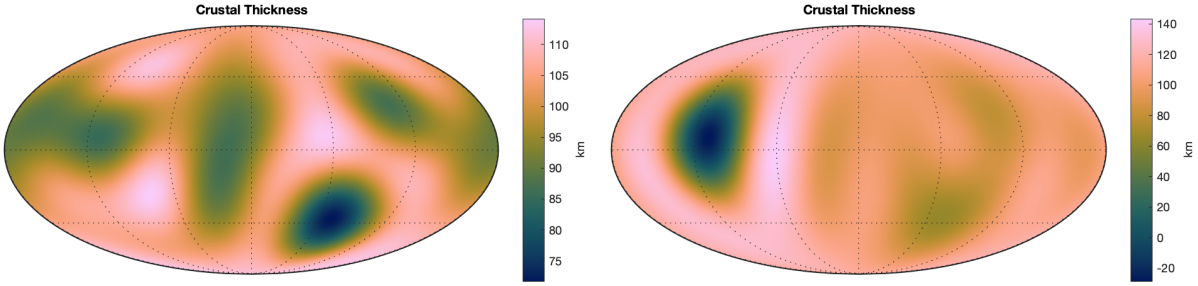

(a) Crustal thickness of the best fitting configuration, a density variation of -9 % at a depth of 1100 km. The remainder of the configuration settings is similar to that of the BD-Hybrid-UC baseline.

(b) Crustal thickness of a removed solution due to geophysically impossible characteristics (a negative crustal thickness is obtained). A density variation of -10 % at a depth of 300 km. The remainder of the configuration settings is similar to that of the BD-Hybrid-UC baseline. A visualization of the cross-section of the anomaly is given in Appendix B Figure B.2c.

Figure 4.22: Crustal thicknesses, one of a valid solution (Figure 4.22a) and one of an invalid solution (Figure 4.22b). Both images are in Mollweide projection with a central meridian of 0 ° longitude.

Similar to the BD-grav models, a sensitivity study is performed into the sensitivity with respect to the viscosity profile, spectral resolution, lithosphere thickness and anomaly thickness. Because the assumption of a solid core primarily affects the solutions in the deep layers (just above the CMB) and the BD-Hybrid models are mainly affected in the shallow layers, as is visualized in the results of the baseline, the solid core model is not expected to change significantly and is therefore left out of consideration for the BD-Hybrid models. After the sensitivity study, a 'special' configuration is researched; a superplume model.

VISCOSITY PROFILE

Three viscosity profiles have been varied, the results are depicted in Figure 4.23. Note that, like in the BD-Grav-Full models, the heat maps look very similar. It should be noted that even the regime of possible solutions (the not NaN values) is similar for all three viscosity profiles. Even for the case where the upper layers have a higher viscosity, expecting less surface topography deformations and therefore a larger range of possible solutions, the regime with possible solutions is not changed with respect to viscosity profile 2. Chapter 5 will elaborate upon this finding.

Figure 4.23 shows that adding the topography as constraint eliminates a few solutions at shallow layers. However, no significant changes occur when altering the viscosity profile. So, the solutions are robust to the change in viscosity profile.

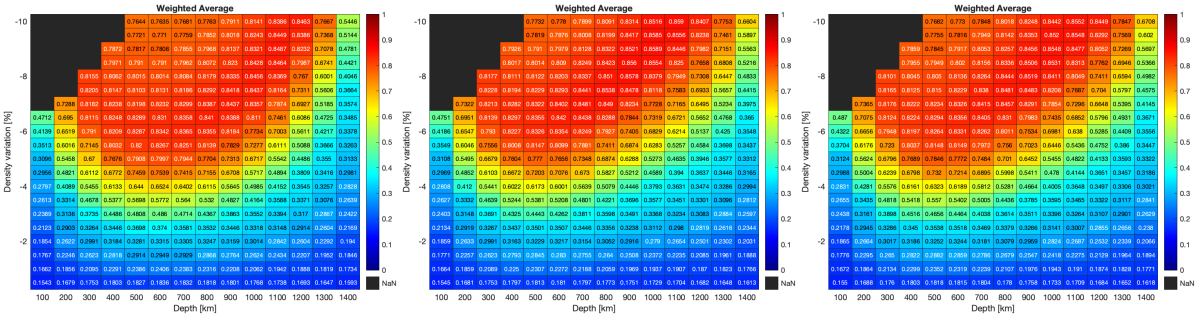

(a) Viscosity Profile 1 (baseline) (b) Viscosity Profile 2 (c) Viscosity Profile 3

Figure 4.23: Heat map of the total (weighted) similarities of the BD-Hybrid-UC varying the viscosity profile. The closer the values are to one, the better the fit. The horizontal axis indicates at which depth (D_a) the anomaly starts (so first column starts at a depth of 100 km). The vertical axis presents the density variation $\Delta\rho/\rho_m * 100\%$. The anomaly is centered at $C_a = [110°W, 3°N]$ and has a thickness (T_a) of 400 km. Lateral sizes: $S_{lon,left} = 24$, $S_{lon,right} = 24$, $S_{lat,down} = 30$ and $S_{lat,up} = 41$ degrees.

SPECTRAL RESOLUTION

The sensitivity of the models upon the spectral resolution has been computed, the results are presented in Figure 4.24.

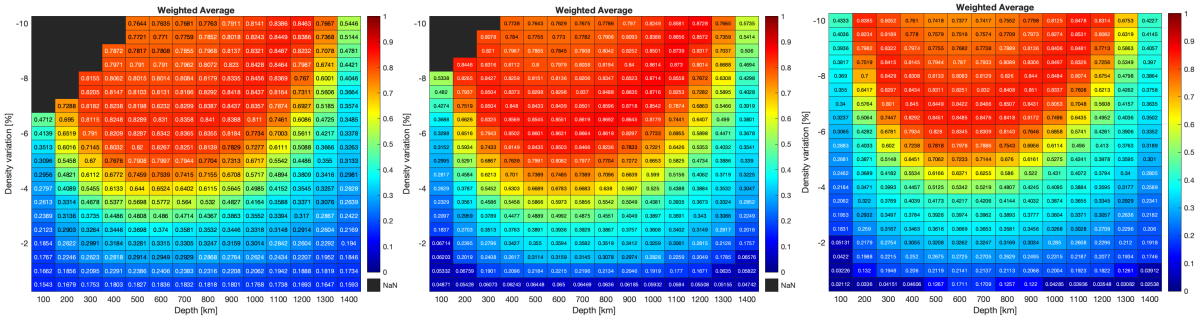

(a) Spherical harmonic degrees 2-5 (baseline) (b) Spherical harmonic degrees 2-4 (c) Spherical harmonic degrees 2-3

Figure 4.24: Heat map of the total (weighted) similarities of the BD-Hybrid-UC varying the spectral resolution. The closer the values are to one, the better the fit. The horizontal axis indicates at which depth (D_a) the anomaly starts (so first column starts at a depth of 100 km). The vertical axis presents the density variation $\Delta\rho/\rho_m * 100\%$. The anomaly is centered at $C_a = [110°W, 3°N]$ and has a thickness (T_a) of 400 km. Lateral sizes: $S_{lon,left} = 24$, $S_{lon,right} = 24$, $S_{lat,down} = 30$ and $S_{lat,up} = 41$ degrees.

Looking at the figures from Figure 4.24a to 4.24c, the amount of well-performing models (indicated by a similarity above 0.8) decreases. Another remark that should be made is that solutions with a very small density variation (<0.5 %) have a similarity close to zero for degrees 2-4 and 2-3. The similarity calculation algorithm is not able to distinguish the areoid contour lines properly because there are no clear distinguishable shapes. This is discussed in Chapter 5. The best-fitting results from the BD-Grav-Full models did not disappear due to the addition of topography constraints, so most of the best-fitting solutions are still valid at lower spectral resolutions. Note that no solutions are invalid for the configuration where SH: 2-3 is assumed (Figure 4.24). In the next section, the effect of changing the lithosphere thickness is determined.

LITHOSPHERE THICKNESS

The lithosphere thickness has been changed to 50 and 200 km in order to determine the sensitivity of the BD-Hybrid-UC model. The results are presented in Figure 4.25.

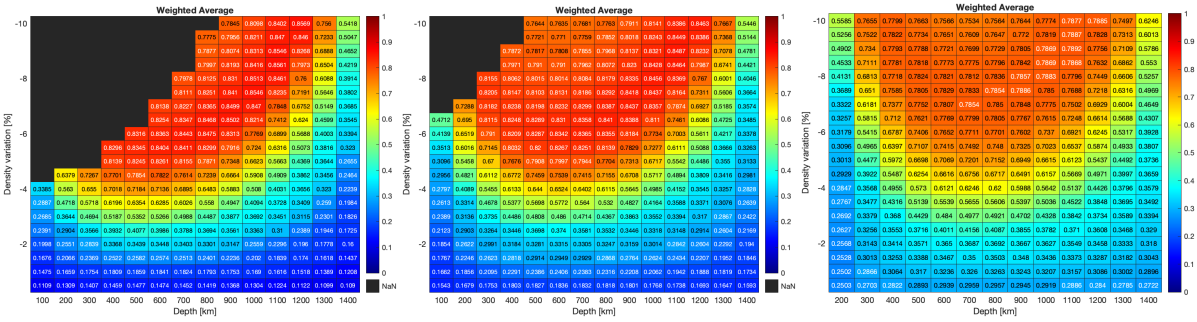

(a) 50 km lithosphere (b) 100 km lithosphere (baseline) (c) 200 km lithosphere

Figure 4.25: Heat map of the total (weighted) similarities of the BD-Hybrid-UC varying the lithosphere thickness. The closer the values are to one, the better the fit. The horizontal axis indicates at which depth (D_a) the anomaly starts. The vertical axis presents the density variation $\Delta\rho/\rho_m * 100\%$. The anomaly is centered at $C_a = [110°W, 3°N]$ and has a thickness (T_a) of 400 km. Lateral sizes: $S_{lon,left} = 24$, $S_{lon,right} = 24$, $S_{lat,down} = 30$ and $S_{lat,up} = 41$ degrees.

Note that the similarity of the solutions decreases when increasing the lithosphere thickness. For a lithosphere of 200 km thick (Figure 4.25c, no solutions are obtained with a similarity above 0.8. Such a high lithospheric thickness has a dampening effect upon the areoid high that is created by the density anomalies. Another relationship can be obtained from these results; the amount of valid (non-NaN) solutions increases when increasing the lithosphere depth. This is as expected since it becomes more difficult for Martian Moho to reach above the topography when the lithosphere is thicker. If a lithosphere of 50 km were to be found for Mars, this could limit the possible best-fitting solutions significantly as they start from a depth of 400 km or deeper.

ANOMALY THICKNESS

The sensitivity of the results as a function of the thickness of the anomaly are depicted in Figure 4.26.

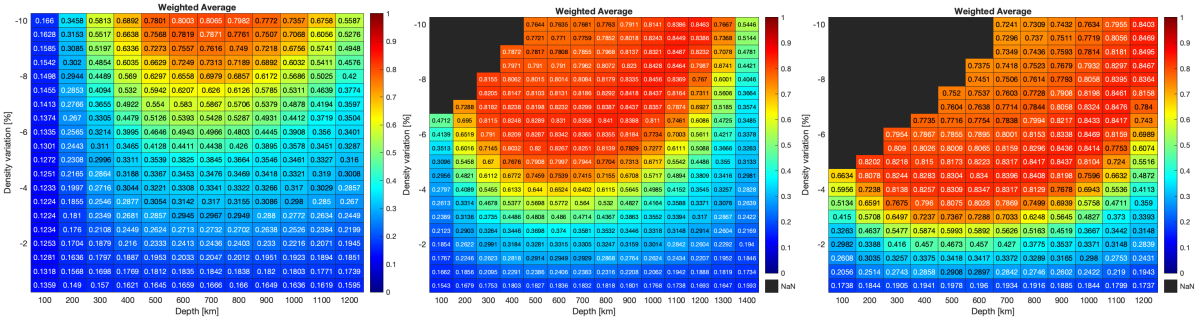

(a) 200 km anomaly thickness (b) 400 km anomaly thickness (baseline) (c) 600 km thickness

Figure 4.26: Heat map of the total (weighted) similarities of the BD-Hybrid-UC varying the anomaly thickness. The closer the values are to one, the better the fit. The horizontal axis indicates at which depth (D_a) the anomaly starts (so first column starts at a depth of 100 km). The vertical axis presents the density variation $\Delta\rho/\rho_m * 100\%$. The anomaly is centered at $C_a = [110°W, 3°N]$and has lateral sizes of: $S_{lon,left} = 24$, $S_{lon,right} = 24$, $S_{lat,down} = 30$ and $S_{lat,up} = 41$ degrees.

Looking at Figure 4.26a to 4.26c (increasing the thickness of the density anomaly), the amount of valid results decreases significantly. For a thickness of 200 km, all configurations are possible. For a thickness of 600 km, the best-fitting solutions at shallow depths and high density variations disappear. Although the number of valid solutions is decreasing, the similarity of the best-fitting solutions increases. For an anomaly thickness of 600 km, solutions are found for a density variation of -4 %. Because of this observed trend (best-fitting solutions having a lower density, and becoming higher) when increasing the thickness of the anomaly, another type of model has been researched: BD-Hybrid-Superplume.

4.3.5. BD-HYBRID-SUPERPLUME

The results of the BD-Hybrid-Superplume models are presented in this section. The superplume is a huge column from the CMB up to a shallow depth (indicated on the horizontal axis in Figure 4.27). As can be seen in this figure, most of the configurations with a density variation larger than -4% are not valid because of a negative crustal thickness that is obtained. However, for density variations smaller than -4 %, a similarity above 0.83 has never been reached in this study. This is very high compared to the maximum similarities encountered in the BD-Grav and BD-Hybrid-UC models. Since a lower density variation is more likely to be in the mantle, these solutions are investigated in more detail. For a spherical harmonic wavelengths 2-3, a similarity of 0.9 was even reached for a density anomaly of -2.5% at a depth of 500 km.

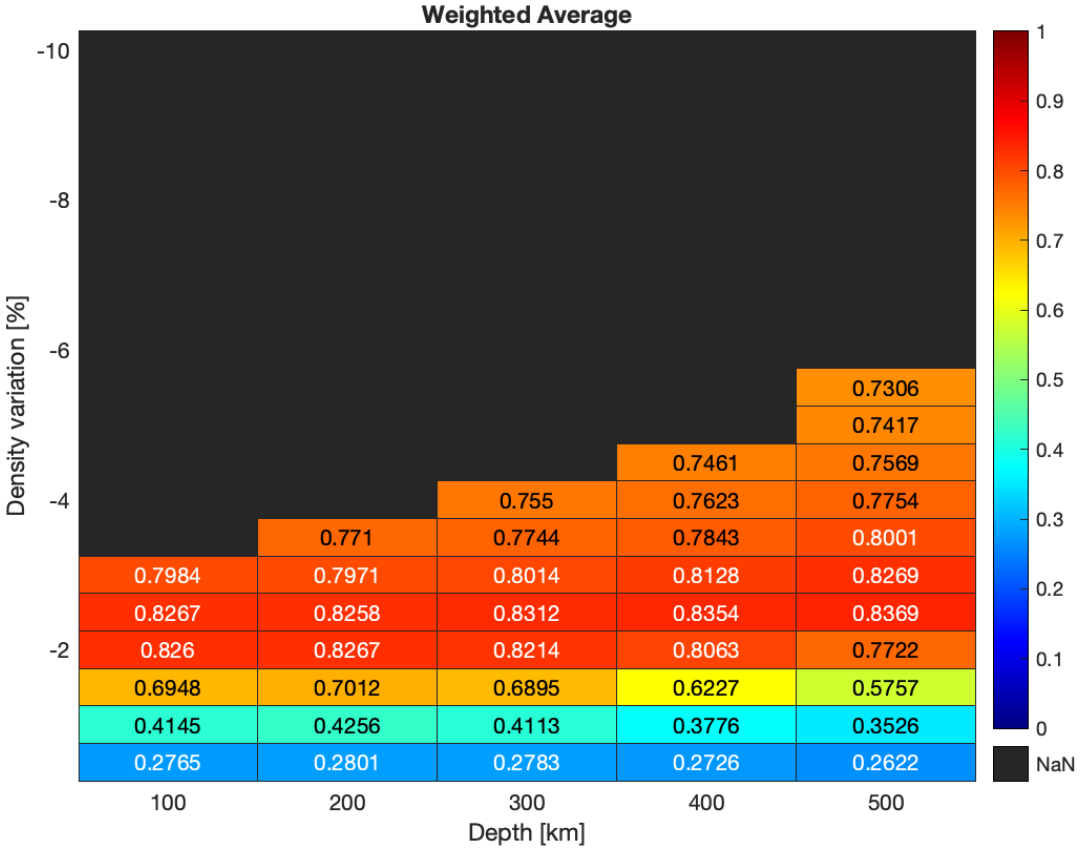

Figure 4.27: Heat map of the total (weighted) similarities of the BD-Hybrid-Superplume. The closer the values are to one, the better the fit. The solutions that result in a negative crustal thickness (assuming a zero-elevation crustal thickness of 100 km) are indicated as NaN-values. The horizontal axis indicates at which depth (D_a) the superplume starts (so first column starts at a depth of 100 km), all configurations continue down to the CMB. The vertical axis presents the density variation $\Delta\rho/\rho_m * 100\%$.

Because the longitude and latitude extent of the anomaly was optimized for the baseline study of BD-Grav-Full, a new determination of the longitude and latitude extends has been performed for a superplume from the CMB to a depth of 500 km with a density variation of -2.5 %. A similarity of 0.946 was found for a density anomaly $S_{lon,left} = 24$, $S_{lon,right} = 32$, $S_{lat,down} = 30$ and $S_{lat,up} = 35$ degrees. A visualization of the cross-section of the anomaly is given in Appendix B Figure B.1d. The size of the mantle plume under Tharsis thus has dimensions of 56 degrees longitude and 65 degrees latitude. The dynamic and isostatic areoid are depicted in Figure 4.28a, not that the dynamic areoid dominates over the isostatic areoid, which is also clearly visible in the total modelled areoid presented in Figure 4.28b.

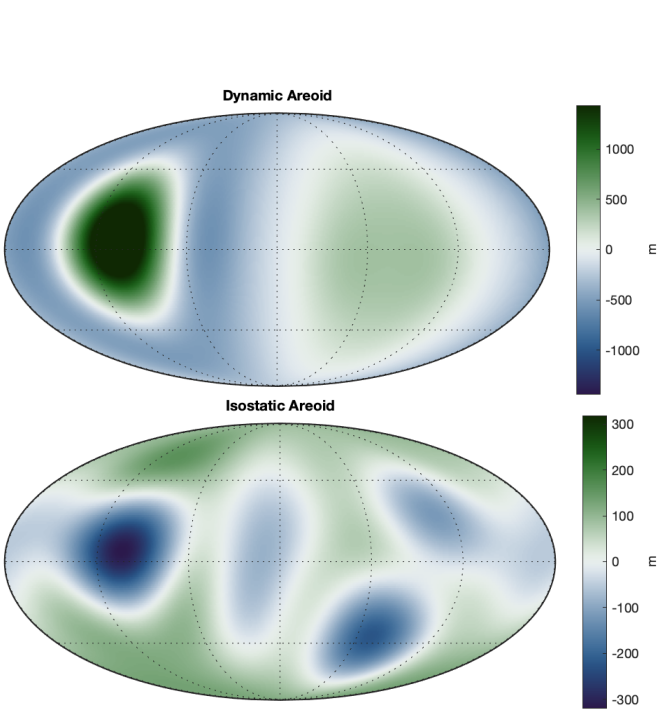

(a) Top: Dynamic component of the areoid field and Bottom: isostatic component of the areoid field. Adding those two components produces the modelled areoid presented in Figure 4.20b. Note the difference in magnitude, the limits of the colorbar of the isostatic component are approximately 6 times smaller than that of the dynamic component.

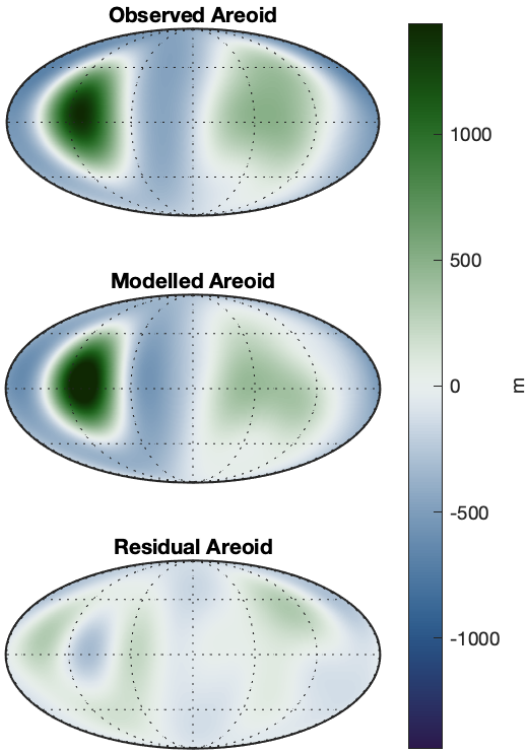

(b) Observed, modelled and residual areoid. The lower limit of the colorbar is manually set to the negative of the maximum observed areoid.

Figure 4.28: Modelling of the areoid, consisting of a dynamic and isostatic (Airy) component. The hydrostatic flattening (95% of C_{20}) is removed. All images are in Mollweide projection with a central meridian of 0 ° longitude. A visualization of the cross-section of the anomaly with respect to Mars is given in Appendix B Figure B.2d.

The dynamic topography caused by the uplift of the Superplume is presented in Figure 4.29b, the topography at Tharsis is very large (11 km) with respect to the observations (4.5 km). After subtracting the dynamic topography from the observation, the isostatically compensated topography is determined. At the Tharsis region, the isostatically compensated crust has an elevation of -8 km (shown in Figure 4.29c). This means that the crustal roots under this region are upwards deflected due to Airy compensation, resulting in an even thinner crust at this location.

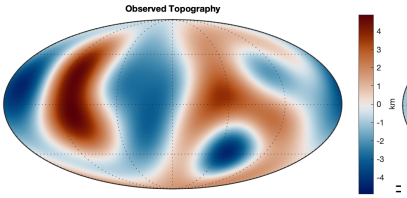

(a) Observed topography, the Martian dichotomy (degree $n = 1$) is removed. The lower limit of the colorbar is manually set to the negative of the maximum observed topography.

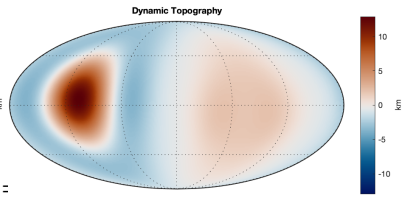

(b) Dynamic topography due to uplift by the buoyant density anomaly. The lower limit of the colorbar is manually set to the negative of the maximum observed dynamic topography.

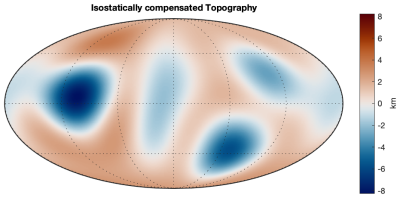

(c) Airy compensated topography (observed minus dynamic topography). The lower limit of the colorbar is manually set to the negative of the maximum Airy compensated topography.

Figure 4.29: Topographies corresponding to the best-fitting model (-2.5% density variation at a depth of 500 km down to the CMB). The addition of the dynamic topography and the isostatically compensated topography produces the observed topography. All images are in Mollweide projection with a central meridian of 0 ° longitude.

The crustal thickness of this superplume solution is depicted in Figure 4.30. A relatively small crustal thickness is observed at the location of Tharsis. The depth of Tharsis is very similar to that of Hellas Basin. As Hellas Basin also has a negative elevation that has a reduced crustal thickness when applying an airy isostatic compensation model.

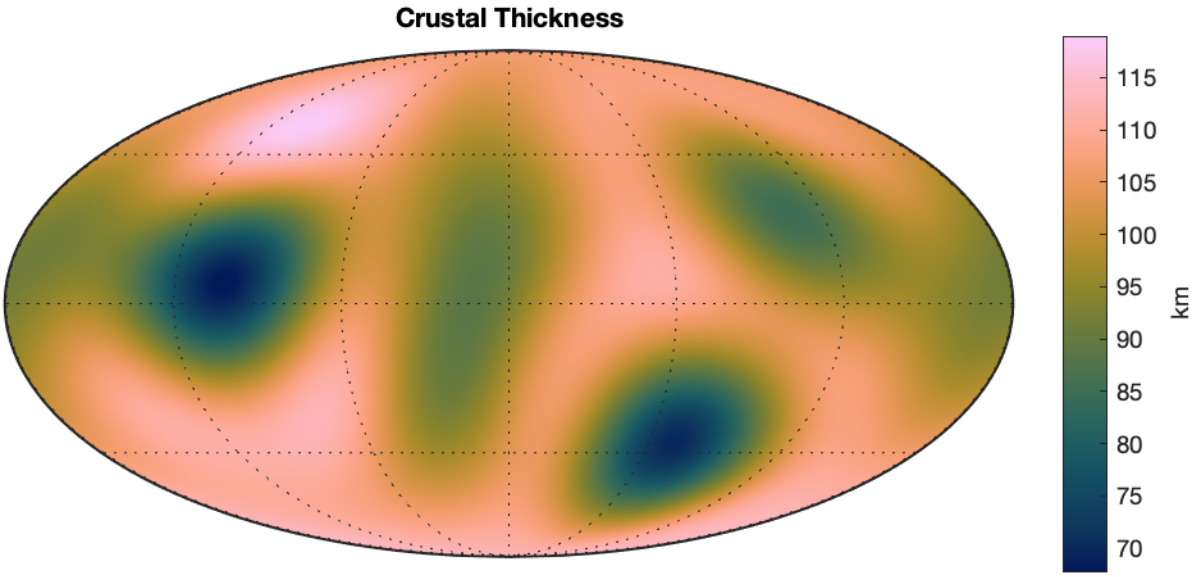

Figure 4.30: Crustal thickness after isostatic compensation has been applied to the remainder of the topography.A density variation of -2.5 % at a depth of 500 km is applied. A visualization of the cross-section of the anomaly with respect to Mars is given in Appendix B Figure B.1b. Both images are in Mollweide projection with a central meridian of 0 ° longitude.

The interpretation of these superplume results is discussed in Section 5.2.2.

4.3.6. SUMMARY OF BD-HYBRID MODEL RESULTS

The BD-Hybrid Models are characterized by an additional constraint, the observed topography, with respect to the BD-Grav Models. The remainder of the topography after subtracting the dynamic topography from the observation was assumed to be compensated by Airy isostasy. The crustal thickness changes because of this and sometimes the crustal thickness becomes negative (the crustal roots reach a higher elevation than the observed topography), in this case the solution is rendered geophysically impossible and is removed from the set of solutions. In most models of BD-Hybrid-UC, some configuration were rendered impossible, some of which were determined to be good models in the BD-Grav-Full results. The BD-Hybrid-UC sensitivity study did not yield very different results from the BD-Grav-Full sensitivity study, except that some good-fitting configurations at shallow depth have disappeared. An increasing lithosphere thickness reduces the performance of the models. In addition, the lithosphere thickness proved to be an important variable in the restriction of potential solutions as this determines if the topography can be isostatically compensated or not. There remains a robustness of the models upon the viscosity and spectral resolution. Moreover, an increasing thickness increases the performance of the models and shifts the best-fitting regime to lower density variations. The BD-Hybrid-Superplume model showed that a high similarity is obtained for a configuration in which a density anomaly is located from the CMB up to shallow layers of approximately 500 km depth. This is an interesting result because of the large nature of the modelled anomaly and the small density variation (only -2.5%) with respect to the mantle that is required. A thorough discussion of these results in shared in Chapter 5.

5

DISCUSSION

This chapter elaborates upon the results gathered in this research and compares them to studies performed by others. It is important to recall the main objective of this thesis, which is to test the hypothesis whether mantle anomalies could be present and if so, are related to the volcanism that is observed on the surface of Mars. The reason for this hypothesis are studies that link the Earth's hotspot volcanoes to the LLSVPs in the deep mantle (e.g. (Torsvik et al., 2006)). Firstly, the DA-Models and the method used to obtain them are put into perspective. Subsequently, the BD-Model results and the corresponding modelling and assessment tools are discussed.

5.1. DA-MODELS

The results found by the DA-S Model revealed that the uplifted long-wavelength gravitational potential feature at Tharsis (Figure 2.3) can be modelled by one single density anomaly in the mantle. Even the negative areoid ring around Tharsis and the positive areoid observation at the antipodal of Tharsis are modelled by this one anomaly. Because of this finding, the assumption of researching only one density anomaly in the mantle is justified.

The search space was not limited to the density anomalies expected for Earth's LLSVPs because the Martian gravity field could potentially be caused by other structures or variations that have density anomalies outside this range. However, it is useful to keep in mind that the LLSVPs on Earth show a shear-wave velocity drop of approximately 0.8 and 1.8% w.r.t the mantle (Ishii and Tromp, 1999; Trampert et al., 2004; Koelemeijer et al., 2017). This corresponds to a positive density contrast of respectively 56 and 130 kg/m^3. This was computed using a relationship between V_S and ρ: $V_S = \sqrt{\frac{\mu}{\rho}}$ (Sheriff and Geldart, 1995).

5.1.1. POSITIVE DENSITY ANOMALY UNDER THARSIS

The anomaly that is required to generate a model that is similar to the observations, depends primarily on its depth, thickness and density. For a symmetric anomaly positioned at Tharsis, the best fitting density anomaly of 400 kg/m^3, 100 km thickness is positioned at a depth of 800 km (Table 4.1). A density anomaly of 400 kg/m^3 is a density variation of approximately 11 % with respect to the mantle (ρ_m = 3550 kg/m^3), this is unrealistic from a geophysical perspective. Based on Earth studies, the density anomalies observed in the Earth's mantle are in the order of 1-2%. For LLSVPs, the density variation is expected to be around 1% (Davaille and Romanowicz, 2020) as well, which makes the obtained solution of 11 % more than an order of magnitude higher. This also implies that for configurations with even deeper anomalies (D_a > 800 km) with the same thickness would require even higher density anomalies $\Delta\rho$ to model a similar areoid. This is due to the fact that the gravity potential is weakened when increasing the distance from the observer to the mass. Looking at a more realistic density regime, a converging solution was found for a density anomaly of 50 kg/m^3 (variation of 1.4 %), starting at a depth of 400 km, down to a depth of 900 km (Table 4.1). This variation is more realistic from a geophysical perspective and it is even within the range of expected density variations for Earth's LLSVPs (Davaille and Romanowicz, 2020). Such a large (500 km thick) positive density anomaly so close to the surface could be solidified material that is remnant of the volcanic period at Tharsis, that is now sinking in the

mantle (because it is heavier than the surrounding mantle). Over a long historical period a recurring volcanic pattern was observed in the Tharsis region (Werner, 2009). It could be the case that upwelling material from the deep mantle was rising towards the surface. But instead of causing another volcanic eruption, Mars has cooled down too much already and there was not enough heat supply to cause another eruption. Instead, the material cooled down before reaching the upper layers and is now at the depth of 400 km and slowly sinking back to deeper layers.

Furthermore, an asymmetric density anomaly was modelled (DA-A). This modification is justified because it represents a more likely scenario; in the physical world almost nothing is exactly symmetrical with respect to its center. Besides, the observations already show that the maximum areoid peak is probably shifted slightly with respect to the middle of the anomaly, implying a skewness. Although most of the solutions did not converge (Table 4.2), better solutions were obtained for a density anomaly of 50 kg/m^3 and 100 kg/m^3. With respect to the areoid peak at Tharsis, the anomaly stretches 28 degrees to the left and 40 to 42 degrees to the right in order to obtain good fits. This result could have several different implications; 1) the edges of the anomaly are not sharply cut-off so a radial gradient is present, 2) there is a density gradient in the anomaly, 3) the anomaly is not actually one structure but consists of multiple smaller components, as is also the case for LLSVPs on Earth (Davaille and Romanowicz, 2020). Such skewness could be caused by mantle flows that move against one side of the anomaly, pushing the top layers more to the other side.

Even though converged solutions were obtained, they did not always result in the model with the lowest RMS error. An investigation was performed in the solutions that were rejected by the search-code, but that were really good fits. An example is presented in Table 5.1; a skewed anomaly of 200 kg/m^3 that only has an RMS of 82.946 m. The search-code rejected this as valid solution because the longitudinal distance from zero-areoid height to the next zero-areoid height (2.3.1) of the model was 10% larger than that of the observations. The fact that this solution, among many others, is removed shows that the search-code is not optimally designed to find the solutions with the lowest RMS. A potential limitation is that the allowed error for the four fitting parameters, which was set manually, had been chosen too arbitrarily and removed otherwise good-fitting parameters. The ratio between the two peaks in the areoid field has too much significance in determining whether a solution converges or not. The search-code can get stuck when going through a landscape of parameter values and a larger than observed ratio is obtained for a certain depth but a smaller than observed ratio is computed for a depth of 50 km higher. As can be seen in Figure 2.12, this causes a repetition. This was the main cause of configurations with a pre-assumed density not converging.

Table 5.1: Configuration settings of top 3 solutions based on RMS, that were rejected by the search-code.

$\Delta\rho$ **[kg/m^3]**	**Depth** D_a **[km]**	**Thickness** T_a **[km]**	**Center Anomaly** C_a	$S_{lon,left}$,$S_{lon,right}$	$S_{lat,up}$,$S_{lat,down}$	**RMS [m]**	**Converged**
100	1200	500	[110°W,3°N]	28,36	30,30	83.297	No
200	1200	300	[110°W,3°N]	28,36	30,30	82.946	No
400	800	100	[110°W,3°N]	26,36	30,30	89.315	No

5.1.2. CMB UNDULATIONS

The DA-CMB models show that the CMB-undulations have to be between 70 and 250 kilometers depending on the core model that is used for Mars. An RMS error of 103 m is obtained for the DA-CMB-1 model (Table 4.3), which is in the same order as the DA-A and DA-S model errors. The areoid created by the undulations is looks similar to the DA-A and DA-S models. Although the areoid fits well, the magnitude of the undulations is higher than expected. According to Heyn et al. (2020), variations of the Earth's CMB are in the order of 10 km. Under the assumption that Mars' CMB is similar to Earth's, variations of 70 kilometers or higher are unlikely. An undulation of 70 km for a core with a radius of approximately 1650 km means a relative increase of 4%. For Earth, assuming a core radius of 3485 km, the undulations are a mere 0.3% which is more than an order of magnitude smaller. However, little is known about the Martian core and maybe it is not similar to Earth's core at all. If there would be such an enormous CMB undulation, it could be involved in the creation of the Tharsis volcanism by pushing the mantle convection - that occurs along the CMB - upwards to the surface. The process would be similar to plume generation zones on Earth but with a CMB undulation instead of an LLSVP being the structure that forces the convective flows upwards. Another scenario, that was not explored by this modelling is the combination of a CMB undulation and a density anomaly radially above it. The method was limited to the investigation of only one density variation (may it be either as a result of CMB topography variation or a density anomaly in the mantle).

The RMS fields still present a dominant feature that is at the location of Utopia Planitia. This feature can be dampened by changing the spherical harmonic degrees to 2 and 3 only, but this also influences the distinctive shape of the Tharsis areoid bulge. Because a large part of the areoid signal of the bulge is in spherical harmonic degrees 4 and 5 (Zhong and Roberts, 2003), this assumption of computing up to spherical harmonics degree 5 is justified. The downside of an increase RMS due to Utopia Planitia was taken for granted. An improvement that could have been applied was a localized determination of the RMS (only in the Tharsis region) to filter out the contribution of Utopia Planitia.

5.1.3. TOOLS AND METHOD

The assessment of the DA-models relied upon four so-called pre-determined fitting parameters, described and presented in Section 2.3.1 and Figure 2.11. All four parameters are computed along a single latitude at 3 ° North, crossing through the areoid peak at Tharsis. Although this approach is computationally fast because it only has to find and compare four values, it also has several limitations. Firstly, the four parameters are not representative of the complete field, the model might indicate a good fit while the Southern hemisphere areoid is modelled completely wrong. Secondly, the depth of the trough (the negative ring around Tharsis) is not taken into consideration, which might actually contain important information to constrain the parameters of the anomaly. Thirdly, the search-code eliminated solutions that fitted the observations really well, based on the threshold settings of one of the four parameters. Since these settings were manually set, they should be revised and changed so that they reveal also the best-fitting models that only deviate in one of the parameters.

Besides the search-code and the assessment of models, there are several limitations in the computation of the areoid. Firstly regarding the construction of the density anomalies; although structures in the mantle are probably circular in reality, the anomalies are modelled in a rectangular (in lateral direction) shape. Besides, only one anomaly was modelled to suppress the complexity of the computations. Even with the presence of those limitations, the models performed very well and the computation time was drastically decreased by taking those assumptions on the shape of the anomalies. Moreover, several assumption were made in the approach of subtracting the crustal contributions from the total gravity field. A large assumption is the zero-elevation crustal thickness for the Airy compensated crust being 100 km. Several studies have performed a more localized estimation of the crust (e.g. Neumann et al. (2004); Wieczorek (2015); Goossens et al. (2017); McGovern et al. (2002)). Neumann et al. (2004) determined a mean global crustal thickness of at least 45 km for Mars. Note that this mean global crustal thickness referred to in many articles in not the precisely the same as the zero-elevation crustal thickness. The latter presents the thickness of the crust when there is no topography (to be compensated). Assuming this value to be 100 km, the mean crustal thickness is calculated to be 100.5 km (see Figure 5.1). Because of this small deviation, the the zero-elevation crustal thickness of this study can actually be compared with the mean crustal thickness of other studies.

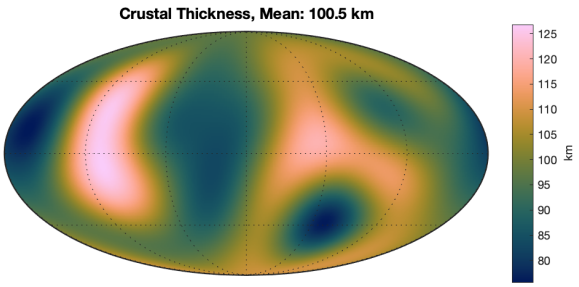

(a) The Martian dichotomy ($n = 1$) is removed.

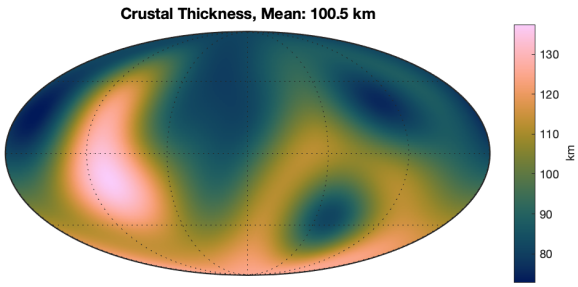

(b) The Martian dichotomy ($n = 1$) is not removed.

Figure 5.1: Crustal thicknesses with an assumed zero-elevation crustal thickness of 100 km, a crustal density of 2900 kg/m^3 and a mantle density of 3550 kg/m^3. For SH degrees 1-5. Both images are in Mollweide projection with a central meridian of 0 ° longitude.

The difference between the models used in the aforementioned literature and this study, is that the literature takes into account a flexural component and a localized density distribution (resulting in a higher density in volcanic regions). In the research, the assumptions of a homogeneous crustal density and a negligible flexural component in the long-wavelength regime were made Mussini (2020). This is one of the main

reasons that the mean crustal thickness is higher compared to the values found by literature. However, the effect of this assumption on the computed areoid is considered small since the crustal contribution to the observed Tharsis areoid bulge is found to be minimal. A more thorough discussion upon the assumption of complete local isostatic compensation at long-wavelengths is shared in Section 5.2.3. The next section will elaborate upon the results found for the studies that took into account boundary deformations due to density anomalies.

5.2. BD-MODELS

The first remark that should be made about the origin of the results of the boundary deformation models is that the solutions indicate that a negative density anomaly is positioned under Tharsis. This observation is in direct contradiction with the results gathered for the DA-Models. The boundary deformations counteract the negative areoid caused by a negative density anomaly by uplifting both the surface topography and the CMB topography, these contributions are large enough to cause the positive areoid bulge observed at Tharsis. This section discusses the solutions from both the BD-Grav and BD-Hybrid models and elaborates upon the limitations of the method.

5.2.1. UPWELLING CELLS UNDER THARSIS

The BD-Grav-Full and BD-Hybrid-UC both presented negative density anomalies as best fitting solutions. The sensitivity study showed a large dependence upon the thickness of the anomaly. Based on the earlier studies of the DA-models, where a high dependence upon the thickness was already detected, this sensitivity is no surprise. The anomalies with a larger thickness not only require the anomaly to have a smaller density variation, they also indicate larger overall similarities. Because of this, there is reason to believe that the density anomalies have a large radial thickness and relatively low (<4%) density variation with respect to the mantle. The dependence of the solution space on the viscosity profile is unexpectedly small. A potential explanation for this could be the nature of the SFEC computations, since SFEC computes a steady-state solution the visco-elastic effect is not demonstrated in the solutions. In addition, the thickness of the lithosphere mainly affects the models at shallow layers. For a larger lithospheric thickness, a higher density anomaly is required to create the same areoid field. This is as expected since the boundary deformation of the lithosphere will be less if there is a larger (highly viscous) lithosphere radially above the anomaly. A solid core primarily affects the models with deep mantle anomalies (located just above the CMB), so assuming a solid vs viscous core has a decreasing impact when considering anomalies at shallower depths.

A negative density anomaly in the mantle means that there is a buoyant region, due to a density anomaly, temperature anomaly, or both. The results from the BD-Grav-Full and BD-Hybrid-UC show that the anomaly should have at least -5% density variation. This value corresponds to an absolute variation of - 178 kg/m^3. Such a density anomaly is very large to encounter in the mantle and would mean that the anomaly would rise upwards with a high velocity. The only way to obtain well-fitting models in a regime with lower density variations, is to increase the thickness of the anomalies (the BD-Hybrid-Superplume model).

5.2.2. SUPERPLUME UNDER THARSIS

The best-fitting solutions that is obtained by this research illustrates a Superplume radially below the Tharsis region. It is characterized by a density anomaly of -2.5 %. Using equation 5.1, the corresponding temperature difference with the surrounding mantle is determined.

$$\Delta T = \Delta\rho / (\alpha * \rho_m) \tag{5.1}$$

Filling in $\Delta\rho = 0.025 \cdot \rho_{m,top}$, with $\rho_{m,top} = 3550$ kg/m^3 (the density assumption of the mantle at a shallow region) and the thermal expansivity $\alpha = 3 * 10^{-5}$. This results in a temperature anomaly of 833K at the top of the plume. For deeper locations, the radial temperature gradient has to be taken into account. At a mantle density of 4000 kg/m^3, the temperature would be $\Delta T = 0.025 * 3550/(3 * 10^{-5} * 4000) = 750K$. These temperature can be put into perspective by computing the rising plume conduit velocity with the approximation by Steinberger and O'Connell (1998):

$$u_i = \frac{k_c * \Delta\rho * g * r_c^2}{\eta} \tag{5.2}$$

Where $k_c = 0.54$ is an empirically obtained constant, $\Delta\rho$ is the difference in density between plume and the surrounding mantle, η is the reference viscosity, g the gravitational acceleration and r_c the radius of the plume conduit. The radius of the plume conduit is approximated by using the cross section of the plume at a radius of 1600 km from the center of Mars. The superplume has a radius of approximately 800 km.

$$u_i = \frac{0.54 * 0.025 * 3550 * 3.711 * 800000^2}{10^{22}} = 35 \text{ cm/yr} \tag{5.3}$$

This rate is huge compared to rising plume conduit velocities on Earth, which are in the order of a few cm/yr. It would mean that material from the CMB, at a depth of 1800 km, would be brought to the surface by the plume in approximately 5 million years. The result was computed with the assumptions of a chemical plume, actual velocities of material inside a thermal plume are expected to be even higher than this conduit velocity (Steinberger and O'Connell, 1998). One of the main reasons for this high plume velocity is the large radius of the (super)plume. A limitation of this modelled superplume is that the plume has a rectangular shape from the CMB to the lithosphere upwards, no distinction is made between the original head and tail of a plume. It could be the case that the plume velocity is higher on Mars than on Earth looking at the size of the volcanism that is the consequence of it. However, with speeds of an order 30 higher than expected based on Earth studies, this research should definitely be followed up to find out the robustness of these results.

MAGMATIC ACTIVITY

The volcanic record on Mars shows a recurring state of magmatic activity (Mège and Masson, 1996; Werner, 2009; Breuer et al., 1996). This periodicity could be closely correlated with the activity of the mantle plume. The records show large volcanic activity approximately every 100 Ma, so 5 Ma to bring CMB material to the surface is relatively fast. This means that the remainder of the time a superplume is not present in the mantle, such periods could be characterized by volcanic remnant material sinking back to the CMB. If there is a huge buoyant plume under Tharsis at this moment, it could indicate that another period of activity is near. The results suggest the plume under Tharsis to be positioned at a depth of approximately 500 km, this distance can be covered by the uprising plume material within 1500 years. Another period of volcanic eruptions in only 1500 years is on geological timescales very soon. However, it should be stressed that the assumptions made for this prognosis are susceptible to large deviations. Another scenario is that this plume is dying out and slowly sinking, for instance if the supplied heat was not sufficient to cause eruptions. In both scenarios, the plume material is moving, so it could be interesting to research the change in gravity field, as the movement of such a large anomaly might be well visible in the data. If the gravity field high increases over time, the plume is moving upwards towards the surface. If the gravity field decreases, it means that the plume is slowly sinking towards the lower mantle. If there is a mantle plume, the core may be still actively cooling. It would also suggest that the models of a thickened crust under Tharsis might be wrong, and the crust including topography might actually be only about 70 km thick (Figure 4.30). This could also explain the size of volcanic constructs in the Tharsis region, which is only possible when the crust is not dampening the buoyant plume material significantly.

The wavelength of the Superplume is 3312 km in longitudinal direction and 3844 km in latitudinal direction, projected on the surface. Figure 5.2 depicts this area and shows its dimensions with respect to the Tharsis region. Even for a superplume, this extent is very large. Note that the region of the Superplume corresponds closely to the region that does not 'obey' the rules of the Martian dichotomy.

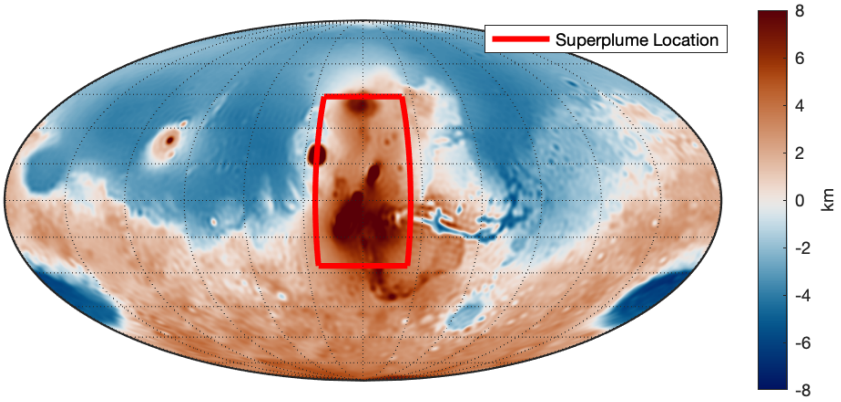

Figure 5.2: Illustration of the size of the Superplume under Tharsis (red outline). The image is in Mollweide projection with a central meridian of 110 ° W longitude. The colorbar has been clipped at -8 and 8 km.

The largest part of the areoid high is due to mantle anomalies and the fact that they are still located under the the topographic high could mean that they are laterally at a stable position (on geological timescales). This does imply that the Martian mantle is not exhibiting any major lateral convection flows, otherwise it would have shifted the anomaly that causes the areoid high in one way or the other. This could mean that a process is occurring mainly in radial direction, for instance the heating of mantle material by cooling of the core, this mantle material flows upwards in a plume, at this point in time the material cools off and part of it sinks down to the core, where it is heated up again and if there is enough hot material gathered at the CMB, the material becomes buoyant enough to cause another plume. This can be seen as a radially oscillating mass anomaly and could explain the periodicity of the volcanic activity in the Tharsis region. This periodicity would obviously decrease and eventually cease to appear, because the core is cooling and will run out of heat. Like a dampened harmonic oscillator looses its amplitude and eventually stops oscillating. The next section investigates the fault pattern in relationship to the location of the solutions.

FAULT PATTERN

The location of the upwelling solution of the BD-Hybrid-UC study and the Superplume both are positioned under Tharsis, as was shown for the Superplume position in Figure 5.2. In addition, the fault pattern is compared to the superplume location and presented in Figure 5.3. Note that the compressional faults are very scarce at the location of the upwelling superplume. A possible explanation is that there were compressional faults everywhere on the planet at first. Once the volcanic activity started, the Tharsis region (including the compressional faults) was completely covered by basaltic material. The question then remains why this uplifted region contains such an enormous amount of extensional faults. A possible explanation is that the large upwelling force (by a superplume or a convection cell) remained under Tharsis for a long time, causing the extensional faults. This also suggests that compressional faults are never formed when the topography is uplifted by buoyant forces, otherwise there would be compressional faults visible as well.

The modelling results of this study reveal a large upwelling force that is still present up to today. It would be an interesting study to determine whether the extensional faults are still increasing in number or size. The rate of such an increase could reveal more about the amount of buoyant material under Tharsis. In addition, an increase in compressional faults would suggest a decreasing uplifting force and could therefore indicate that the superplume (or cell) is losing its strength.

To put this theory into perspective, Banerdt et al. (1982) concluded that a dynamic support of the lithosphere would cause compressional features within the supported region and radial (extensional) features in the periphery. Although the latter condition is satisfied, no compressional features are detected within the supported region. Therefore, it is recommended that future research is performed into the effect of an uplifting force under Tharsis on the stress field and fault patterns. Another research into the fault pattern on Mars was performed by Carr (1974), they suggest that the formation of the Tharsis bulge happened before the formation of the volcanoes. If this was the case, it is peculiar that the extensional faults were not covered by the volcanism that occurred after the formation of the bulge. However, it could be possible that the extensional faults were initially covered by the volcanism, but new ones emerges due to the continuous uplift by the upwelling material.

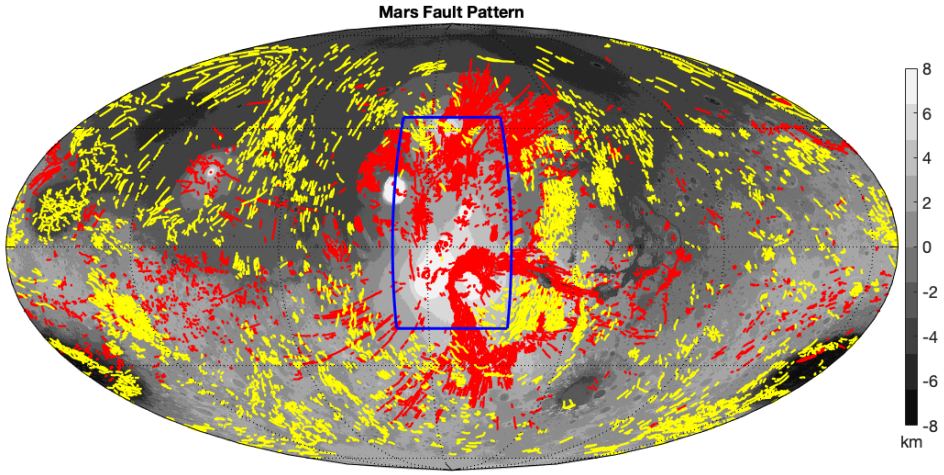

Figure 5.3: A representation of the fault patterns on Mars, the compressional faults are marked in yellow, the extensional faults in red. In addition, the Superplume is illustrated with the blue outline. Data was obtained from Knapmeyer et al. (2006). The map is a Mollweide projection with a central meridian of 0 ° longitude. The topographic colorbar has been clipped at -8 and 8 km.

TEMPERATURE ANOMALY

The density of the modelled anomalies can be computed into temperature anomalies. Although there is a scarce knowledge about heat fluxes and temperature in the Martian mantle, one could try to model the heat dissipation in future models. A study that has taken into account heat production rates and present day Heat Producing Elements (HPE) abundance is Plesa et al. (2018). Their model suggests that the present-day plume under Tharsis is currently stable and has been over a significant part of its thermal evolution. They find a temperature of approximately 1400 K just 150 km below the center of the Tharsis bulge. In our model a value of -2.5% density variation corresponds to 833 K temperature increase with respect to the mantle temperature at 500 km depth, which is between 800 K and 1600 K (minimum temperature profile vs maximum temperature profile (Plesa et al., 2018)). Resulting in a temperature of at least 1633 K in the mantle plume. The temperature difference created by the plume thus comes close to other research when assuming the minimum temperature profile. Additionally, the superplume that was found by our modelling is larger in size (approximately 3000 by 3000 km) and is located under a thinner crust. This thin crust is the consequence of assuming that only Airy compensation is happening at the very long-wavelength features. The Airy compensation has to counteract the increase in dynamic topography by creating a negative elevation, with the consequence of a thinner crust. As a result, the heat production rates and heat dissipation would be higher in our model compared to models where the same radial temperature is assumed but with a smaller plume and thicker crust. Researching whether our heat production rate would still agree with for example gamma-ray measurements of heat production (Hahn et al., 2011) would be an important step in the interpretation of these results. The differences in plume size and temperatures could also be attributed to the fact that Plesa et al. (2018) includes a spatially varying crustal thickness model and a viscosity that is an order of magnitude higher in all layers of the mantle. The varying crustal thickness has a large influence on the temperature of the mantle plumes at shallow layers (above 600 km), this assumption could therefore also be an important contributor to the differences between the observed plumes. As the results have been put into perspective, the limitations of the method will be addressed in the following sections, beginning with the crustal reduction in Section 5.2.3.

5.2.3. CRUSTAL REDUCTION

An Airy isostatic model was assumed for the crustal compensation at low spherical harmonic degrees, several recent findings have pointed out that this assumption is prone to errors. A study by Zhong and Roberts (2003) showed that a thermal plume under the Tharsis does not contribute more than 15 % to the observed long-wavelength areoid and 25% to the topography of the Tharsis Rise. A constraint within this research was the

topography; Zhong and Roberts (2003) assumed that the topography deformation as a result of an upwelling mantle plume cannot produce topographies larger than the observed topography. Zhong did not look into the possibility that the topography is completely upholded by dynamic forces and the lithosphere actually counteracts this by its elastic lithosphere. In this research, solutions were found that create a larger-than-observed topography, resulting in a negative isostatically compensated topography. In agreement with this enormous dynamic uplift is a study by Harder and Christensen (1996), they also found results indicating a giant plume under Tharsis being the main contributor to the areoid high, and also neglected taking into account an elastic lithosphere of 150 km (McGovern et al., 2002; Zuber, 2000; Zhong, 2002). A major difference between the research Zhong and Roberts (2003) conducted and this research is the modelling of the compensation. Mussini (2020) found that the long wavelength spherical harmonic wavelength are dominated by Airy compensation, and regional flexure is negligible. Because of this, only Airy isostasy has been assumed as crustal model while Zhong and Roberts (2003) implemented a thin shell flexure model which influences the results significantly. A next step for our research would be to add a thin elastic shell to SFEC in order to research the dependence of the solutions on the flexure properties. Wieczorek and Zuber (2004) states that the Tharsis province is dominated by loading and flexure up to degree 6. This claim is also supported by results of Zuber and Smith (1997) and Phillips et al. (2001); the Airy compensation has minor influence on the gravitational potential. Although this assumption would influence our models, the results indicate that the gravitational field could be completely explained by upwelling mantle material below Tharsis. Figure 5.4 presents the power spectrum of the GMM-3 observed gravity, and the gravity caused by topography for an uncompensated case, Airy compensated case and a flexure (thin shell) case.

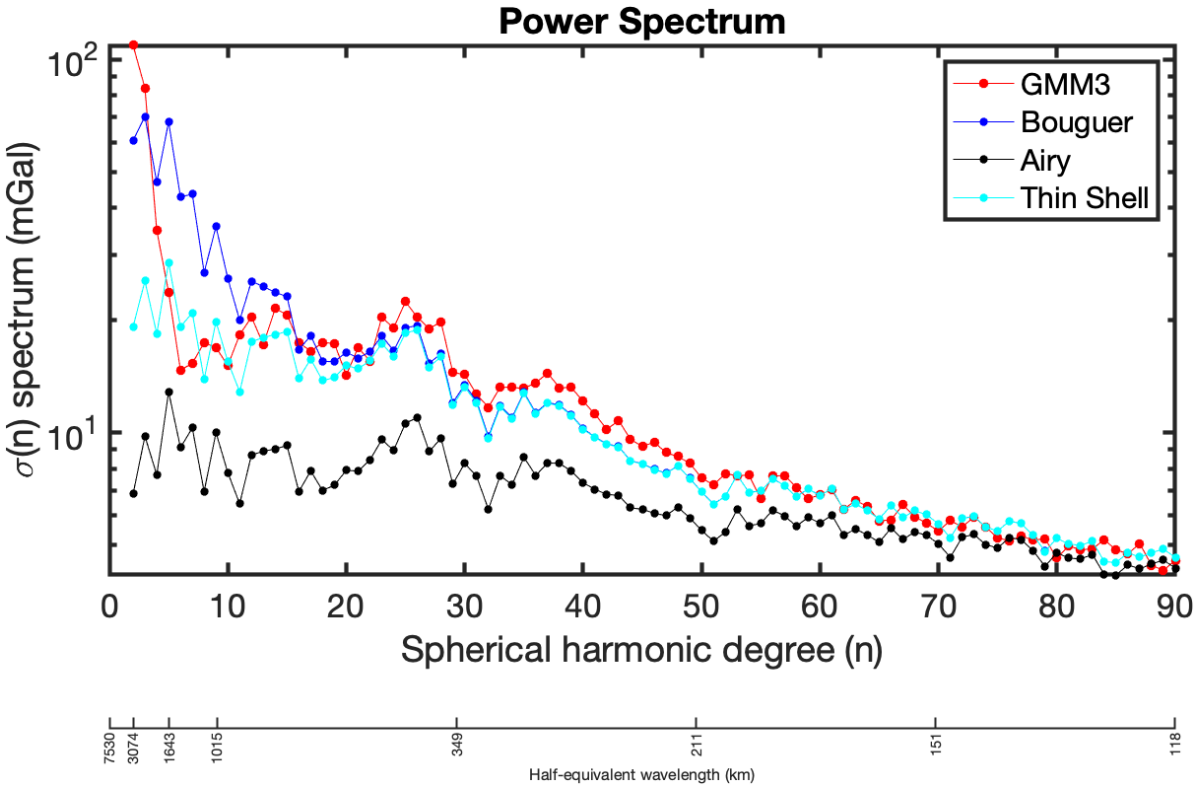

Figure 5.4: Power spectrum of the GMM-3 gravity and topography (uncompensated, Airy compensated, or regionally (flexure) compensated).

Figure 5.4 shows that at low spherical harmonic degrees $n < 6$, the gravity signal in the case of Airy compensation is very low compared to the observed gravity. Consequently, the observed gravity seems more likely to be consisting out of uncompensated topography or a thin shell model. The Airy gravity comes closes to the observation at very high spherical harmonic degrees, but this part of the spectrum is not of interest for this study. To conclude, assuming the long-wavelength features to be primarily compensated by Airy isostasy is likely to be wrong. In future studies, a thin shell flexure model should be implemented to obtain a better model representing the crust at long wavelengths. Section 5.2.4 discusses the approach that was taken in

obtaining the assessment of BD-model results.

5.2.4. COMPUTATION AND ASSESSMENT

Firstly, this section presents a discussion on SFEC in general. Subsequently, the method to assess the models is elaborated upon. In addition, the performance of the similarity with respect to the χ^2 assessment is discussed. SFEC has a very low computation time due to its decoupling in radial FEM elements and lateral spherical harmonic description, enabling the user to perform over a thousand simulations per hour. The layers of the model have to be adjusted manually, therefore the radial density profile as well as the viscosity profile are discrete. Other mantle convection models are able to ingest radial profiles of much more detail (e.g. Gaia (Plesa et al., 2018)). Since there is so little known about Mars' interior this limitation is not expected to be significant. Another downside is that the SFEC modelling does not result in a time-dependent mantle convection pattern, only the ultimate situation when all stress differences have been taken into account. This does not make it possible to see whether a solution is stable after a specific amount of time, it limits the analysis to the current situation. Although it would be great to see the time dependence, it is not required for our models to be valid, since the only gravity and topography data are of geologically recent timescales. Extrapolating the solutions in time would introduce many more (time-dependent) uncertainties. The Young's modulus (elastic properties) of the lithospheric shell that is implemented in SFEC, cannot be modified. Only the thickness and density of the lithosphere can be modified. Although flexure was not taken into account during this study, it would have been useful to study the effect of the elastic properties of the lithosphere in order to find out whether the solutions are robust or not.

Initially, the density (in addition to the thickness) of the lithosphere in SFEC was expected to be of influence to the results. A higher density would make it more difficult for the buoyant anomalies to create a topographic uplift as more mass has to be moved. However, the contrary was the case; the mathematical expressions in SFEC indicate that for a non self-gravitating model the lithosphere density have no effect on the observed areoid. A visualization is given in Figure 5.5.

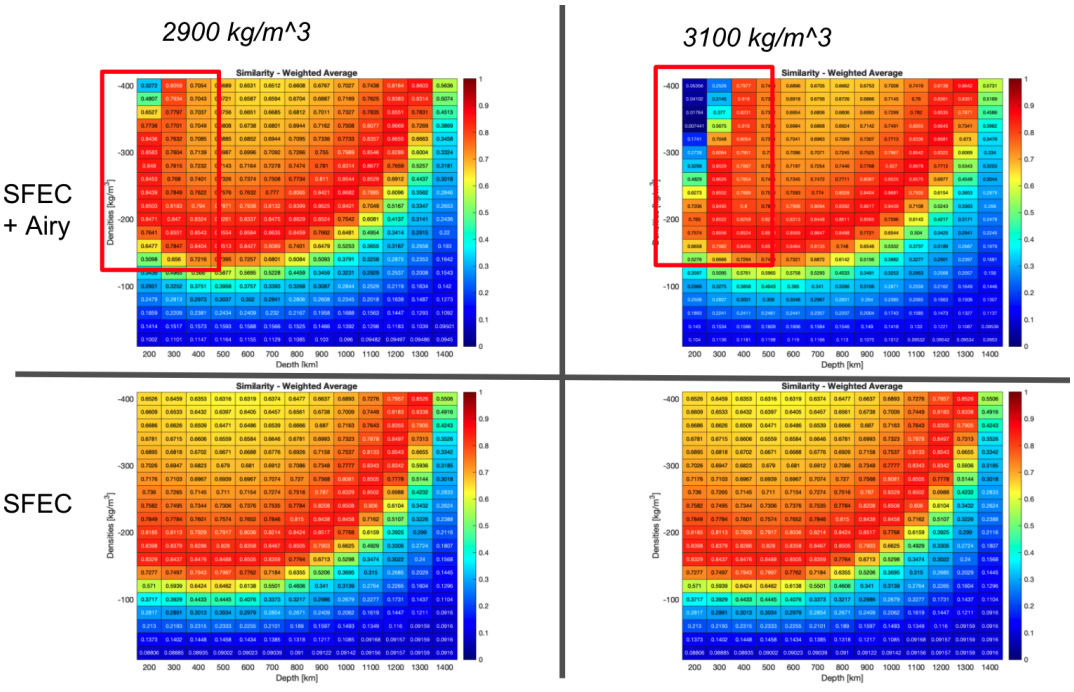

Figure 5.5: Top: similarities obtained for a hybrid study (dynamic and isostatic) for lithosphere densities of 2900 kg/m^3 and 3100 kg/m^3. Bottom: similarities obtained for a purely dynamic (SFEC) configuration for lithosphere densities of 2900 kg/m^3 and 3100 kg/m^3. Note that the lithosphere density has no effect in the purely dynamic case. It does influence the shallow solutions in the hybrid study.

It is the case that for a non self-gravitating model, the gravitational potential computed by SFEC do not change when increasing the lithosphere density. This is shown by the bottom two heat maps in the quadrant of Figure 5.5. If the Airy isostasy is taken into account for the remainder of the topography, the results change

for the upper layers. The reason why the computed fields by SFEC are not sensitive to a change in lithosphere density is that the stresses scale with the density and the gravitational potential is calculated by dividing the stresses by the lithospheric density, annihilating the scaling done in the stress calculations.

For the assessment of the models, the 'Similarity' approach was developed. This worked very well in determining whether a model fits the observations and how it compares with other models. Taking a weighted average where the weight factors are determined by the area of the contour at a specific area height make sure that each contour is taken into account appropriately. For instance, the zero-areoid contour lines always have a large area and it is therefore easy to create a large overlapping region between model and observation. The areoid height contour at 800 m is much more susceptible and it is more difficult to create overlap for these contour since they are smaller. Therefore, the smaller area contours should be weighted higher in comparison with larger area contours. In addition, this method proves to be user-friendly and easily customizable. The user is enabled to specify which contours should be considered, for instance; if a localized analysis has to be done only on the Tharsis bulge, those contours can be selected. If one also desires to take into account the Tharsis trough (negative ring), those contours can be added to the computation. No other studies have been found that exploit the similarity to test their models, this is probably due to the limitation that it can only be used for low degree spherical harmonic fields ($n < 6$ for Mars). For higher spherical harmonic degrees, the contour detection becomes more problematic because the smaller wavelength features will result in more variation in areoid heights. Consequently, it could create a field where 20 contours at an areoid of 200 m are found. In that case, selecting the correct contours is a limitation of the code.

SIMILARITY VS χ^2

In order to analyse the statistical significance of a set of solutions, the Chi-squared method is often used. The χ^2 is calculated according to the following formula:

$$\chi^2 = \frac{1}{N}\sum_{i=1}^{N}\left(\frac{V_{obs,i} - V_{mod,i}}{\sigma_{obs,i}}\right)^2 \tag{5.4}$$

Where N is the number of observations, V_{obs} are the spherical harmonic coefficients of the observed field and V_{mod} that of the modelled field. The standard deviation is given by σ_{obs}. The χ^2 of each of the models is calculated, the lower the value, the better the fit. This can be done for a complete parameter space, in order to determine which of the parameters fits the observations best. Figure 5.6a presents the χ^2 values relative to that of the best fitting model.

The χ^2 values are very high, this could be due to bad fit (with respect to the error of the observations). It is not because of the parameter space that was selected, because the best-fit (lowest χ^2 was in the order to 10^13. Since these values do not present a distribution that can be statistically interpreted, a more robust way to determine the goodness-of-fit was explored; the L1-misfit (Van Der Wal et al., 2013);

$$\chi^2 = \frac{1}{N}\sum_{i=1}^{N}\left\|\frac{V_{obs,i} - V_{mod,i}}{\sigma_{obs,i}}\right\| \tag{5.5}$$

The L1-misfit is presented in Figure 5.6b.

The L1 misfit has significantly smaller values and the sensitivity to outliers is dampened, but it is still difficult to interpret these with a gamma distribution. All values above 5.99 would be refused if a confidence interval of $\alpha = 0.05$ would be selected with two degrees of freedom. It could also be that the model is just extremely sensitive to the depth and density of the density anomaly. However, if we were to select best fits from this χ^2 distribution, there would be only 1 good solution at a resolution of 100 km layer thickness and 20 kg/m^3, while it is expected that there is a large range of possible solutions. The limitation of the assessment code is that it cannot be interpreted statistically by the use of a χ^2-distribution. Other statistical tools (e.g. Pearson correlation matrix, vote maps, RMS) have been explored but were not applicable to these models. Since the error of the observations (σ_{obs}) is very small, the deviation between the models and observations is always large. However, this limitation is partially nullified by the use of the Similarity approach. Below it is explained that the best-fitting results from the χ^2 plot correspond to the best-fitting models presented in the Similarity heat maps. Although the χ^2-values are too high, their relative performance, statistically spoken, is still presented in the plots of Figures 5.6a and 5.6b.

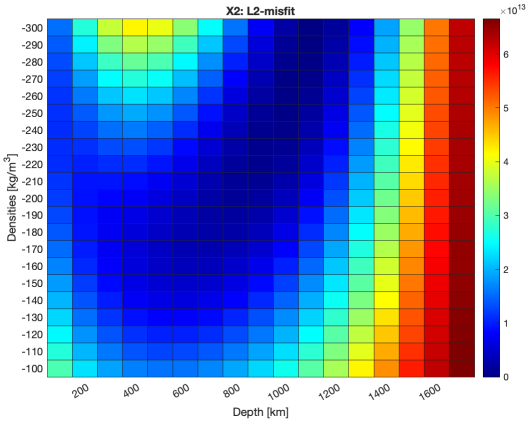

(a) χ^2 values for models with a density anomaly at a certain depth. Only spherical harmonic degree $n = 2$ was taken into account.

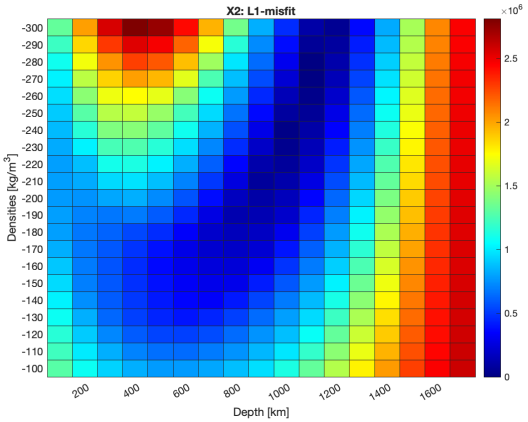

(b) L1-misfit for models with a density anomaly at a certain depth. Only spherical harmonic degree $n = 2$ was taken into account.

Figure 5.6: χ^2 values for (a) the original format and (b) the L1-misfit.

The similarity is a measurement of the goodness-of-fit, since it compares the complete model with the observations in a sophisticated way. There are two factors that are neglected in the similarity method that are not for χ^2: (1) making the comparison with the best-fitting solution in order to define which solutions are closest to the best-fit (threshold) and (2) taking into account the relative uncertainties of the observations. A threshold is established to determine the best-fitting results in the χ^2, the same is done for the results from the similarity, see Figure 5.7.

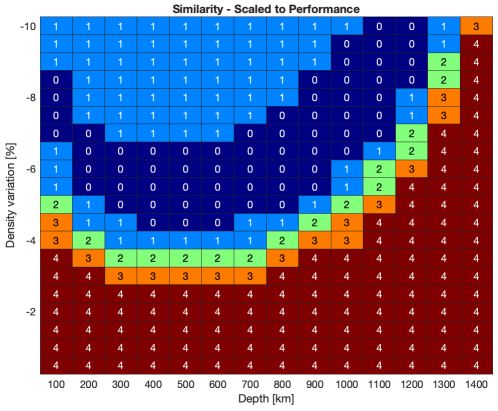

(a) Similarity solutions rated from 0 to 4 based (0 has a similarity above 0.8, 1 a similarity between 0.7 and 0.8, 2 a similarity between 0.6 and 0.7, and so on).

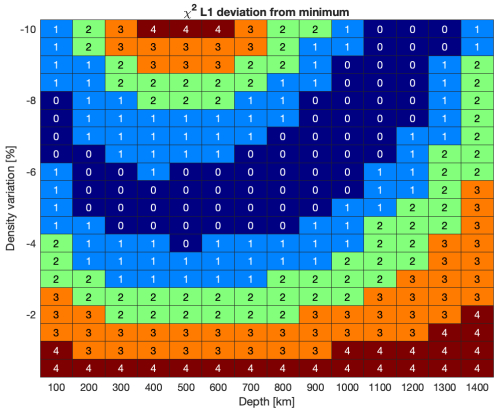

(b) χ^2 solutions rated from 0 to 4 based on the deviation of the best-fitting solution (0 has a χ^2 close to the best-fit, 4 deviates the most). Only spherical harmonic degree $n = 2$ was taken into account.

Figure 5.7: Comparison between χ^2 values and similarity values.

Figure 5.7 shows that the best-fitting solutions from the χ^2 plot (Figure 5.7b) correspond closely to the best-fitting solutions of the similarity plot (5.7a). To conclude, the limitation of not having a statistical significance on the model assessment is largely accounted for by the similarity method. Therefore, the assumption of only using similarity for the assessment of models is justified.

6

CONCLUSION

A study was performed to gain insights into the possible origin of the volcanism on Tharsis. Tomographic studies on Earth's mantle indicated a possible relationship between the geoid, structures in the mantle, and the volcanism that is observed on the surface. It was researched if Mars could exhibit a similar relationship between its volcanic topographic features (in Tharsis) and density anomalies in the mantle. The following research question is answered:

Could the unique volcanic topographic features of the Tharsis region be related to density anomalies in the Martian mantle?

There could definitely be a relationship between the unique volcanic topographic features of Tharsis and density anomalies in the mantle. The solutions that were obtained indicate that large, negative density anomalies in the upper mantle of Mars represent the most likely scenario. These negative anomalies have a buoyant character and therefore an uplifting effect on the topography of Tharsis. In addition, based on the temperature it can be concluded that those anomalies could have provided enough heat in the period of volcanic activity. This conclusion results rejects the hypothesis of mantle structures similar to LLSVPs being the main contributor of the uplifted areoid and topography at Tharsis. However, it does not imply that no structures similar to LLSVPs are present in the deep mantle of Mars, only that they are not the dominating factor in the expression of the areoid and topography. In the following paragraphs this conclusion is supported by answering the sub-questions about crustal models, possible density anomalies and the relationships between anomalies and volcanism.

The Tharsis region is characterized by a long-wavelength (spherical harmonic degree $n < 5$) areoid and topography anomaly. In order to derive the gravity field of the mantle, an Airy crustal reduction was applied because Airy is the dominant form of compensation at those long-wavelengths, based on Mussini (2020). The remainder after crustal reduction was assumed to be solely responsible to density variations in layers beneath the crust, so the mantle and CMB. A sensitivity study was performed to find possible relationships between depth, density, thickness and size of the modelled anomaly and the resulting areoid. Consequently, the best-fitting solutions were determined and it was found that the best-fitting anomaly has a density anomaly of $\Delta\rho = 400$ kg/m^3 and is located from 800 to 900 km depth. For deeper anomalies, the density anomaly or the thickness has to increase in order to create a similar areoid. A density anomaly of 400 kg/m^3 was rendered unrealistic after geophysical interpretation (it corresponds to a density anomaly of 3500 K, which is too large for a mantle anomaly). In addition to anomalies in the mantle, the CMB topography undulations were found to be a potential cause of the observed areoid and topography high at Tharsis. The results showed that the undulations should be at least 70 km, in order to generate a gravitational potential that is close to the observations. Although these undulations are large compared with the expected CMB variations of at most 10 km, it cannot be excluded that they have a partial contribution to the observations.

The models were improved by computing the boundary deformations that are the result of anomaly-induced stresses. This computation was performed by a mantle convection code called SFEC (Tosi, 2007). The topography is taken into account by subtracting the SFEC surface boundary deformation from the ob-

served topography, the remainder was assumed to be Airy compensated. These models showed that the observed areoid high at Tharsis is likely not due to a positive density anomaly in the mantle, but a negative one. Such a negative density anomaly could be compositional or thermal and manifests itself as an upwards moving cell (or superplume). Such a superplume would have a temperature of 833 K and a rising velocity of 35 cm/yr. A remarkable conclusion is that the topography to be compensated isostatically is negative because of the major contribution of the dynamic topography. Consequently, the crust under Tharsis is only a few kilometers thick. The buoyancy created by the anomaly not only pushes the surface topography upwards, it also results in a positive CMB topography at the specific location. It was determined that this CMB variation is unlikely to be the main contributor to the observed areoid and topographic high. The solutions are sensitive to changes in anomaly thickness and lithosphere thickness. However, they are very robust to changes in viscosity profiles (e.g. Steinberger et al. (2010) and Plesa et al. (2018)) or the spectral resolution.

Although a superplume starting at a depth of 500 km below the lithosphere of Tharsis is the best-fitting solution, it does not imply that structures just above the CMB do not occur in Mars. There could be a positive density anomaly similar to the LLSVPs on Earth, but this is definitely not the main contributor to the observed degree 2-5 areoid high at Tharsis. The relationship between the mantle gravity anomaly and volcanism is clear, the superplume is likely to have supplied the required heat to create volcanic structures in the Tharsis region. The extensional faults around, and the lack of compressional faults in the Tharsis region suggest that the compressional faults were covered by volcanism that occurred after the topographic uplift. The results obtained in this research indicate that there remains to be a superplume, as well as an enormous dynamic support, under Tharsis. Whether this plume might have existed from the beginning of the evolution, or is time-dependent and closely related to the magmatic periodicity, is still up for debate. In the following section some recommendations for future research are shared.

RECOMMENDATIONS

Based on the research that was conducted, recommendations were established for upcoming research. Firstly, it might help in the assessment of SFEC as useful mantle convection model for Mars to determine the effect of implementing visco-elastic relaxation instead of Instantaneous Viscous Flow (IVF) for our configurations. Moreover, the assumption of Airy compensation at long-wavelengths should be re-investigated, recent studies suggest flexural loading to be the main contributor at long-wavelengths. This also implies that one might look into the effect of elastic thickness and hybrid loading models assuming a thin elastic shell. In addition, one could explore the possibility of adding the topography and first crustal layers to SFEC to make calculations with GSH redundant.

Subsequently, one might try to determine exactly how much of observations is modelled by plume and what is left for deep mantle anomalies. In order to do this, the contribution of the plume should be researched in more detail. An interesting insight would be to do determine whether the plume is currently stable, or moving up or downwards in the mantle. This could give an indication whether this plume can be linked to the periodicity of magmatic activity, whether it is old-volcanic material sinking towards the CMB or a rising plume reaching for the surface, which could potentially lead to another volcanic episode in Tharsis. For this study, one might investigate whether the gravitational potential field shows a time-dependency in degree 2 and 3. If the areoid increases over time, it could mean that a plume is rising towards the surface.

In addition, it would be interesting to investigate whether a density anomaly such as the superplume would result in the movement of the polar rotation axis (polar movement). In this way, one can determine whether a solution could have been stable over a certain duration. For the relationship between volcanism and the topographic and gravity fields, one might consider creating a Martian eruption site density density distribution. Such a hotspot density map can be translated into spherical harmonics and the correlation with topography and gravity could be determined.

Finally, the mantle anomalies that were considered during this research were based on several assumptions that do not represent a realistic situation. A shape other than a rectangular should be considered. For example one that is thinner in the middle and has a circular cross section as this is often the case for anomalies subdue to a gravity field of a planet. Moreover, one might consider investigating a hybrid anomaly which has a negative density anomaly in the shallow layers (corresponding to the observed plume) and a another anomaly near the CMB representing a structure similar to the LLSVPs observed in Earth.

A

Airy Isostasy

The Airy model is most sensitive to a change in zero-elevation crustal thickness (which is close to the mean crustal thickness). In addition to the results presented in Section 4.1 (where a zero-elevation crustal thickness of 100 km was computed), this appendix shows how a change in this thickness affects the Airy model. A mantle density ρ_m of 3550 kg/m^3, a crustal density ρ_c of 2900 kg/m^3 are assumed. The spherical harmonics used are 2-5.

The topography in SH 2-5 is independent of the assumed zero-elevation crustal thickness and is presented in Figure 4.3a. The crustal depth is computed by calculating the roots under the compensated topography. As can be seen in Figure A.1, an increase in zero-elevation crustal thickness results in a linear increase in the crustal depth plot. The crustal depth variations stay the same, only it is moved downwards.

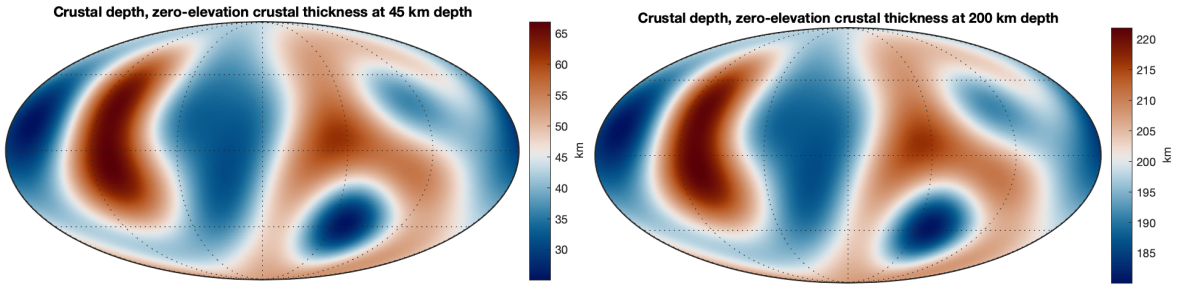

Figure A.1: Crustal depths for an Airy model assuming a zero-elevation crustal thickness of 45 km (left) and 200 km (right). The images are in Mollweide projection with a central meridian of 0 ° longitude. All figures are in SH degree 2-5 so the crustal thickness dichotomy ($l = 1$) has been removed.

With the topography and the crustal depths, the R-component of the gravity vector can be calculated for both cases. The resulting gravity field due to the Airy isostasy is subtracted from the observations. The residual is the gravity field due to the mantle (assuming that the Airy isostasy is a complete representation of the crust). As can be seen in Figure A.2, an increase in the zero-elevation crustal thickness results in a gravity field caused by the crust. The is because the density variations (which are on the boundary of the crust and mantle) are shifted downwards, their effect is dampened and the gravity field due to the topography dominates.

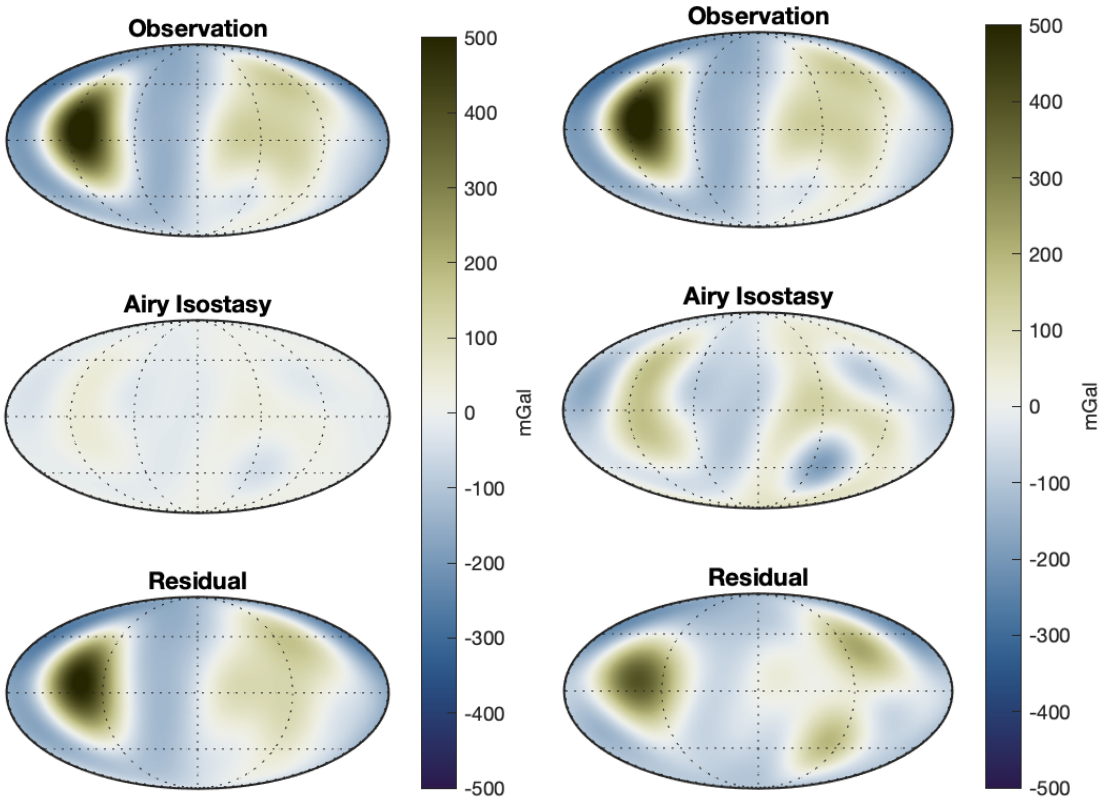

(a) Zero-elevation thickness of 45 km. C_{20} is removed for 95%.

(b) Zero-elevation thickness of 200 km. C_{20} is removed for 95%.

Figure A.2: Top: observed gravity field (R-component of gravity vector). Middle: gravity field of the topography compensated with Airy isostasy, assuming a zero-elevation crustal thickness of 100 km, a crustal density of 2900 kg/m^3 and a mantle density of 3550 kg/m^3. Bottom: Airy isostasy gravity field subtracted from the observed gravity field to obtain a gravity field representative of the lower layers. The colorbar has been clipped at -500 and 500 mGal. All images are in Mollweide projection with a central meridian of 0 ° longitude.

Moreover, the gravitational potential after crustal reduction is computed and presented in Figure A.3.

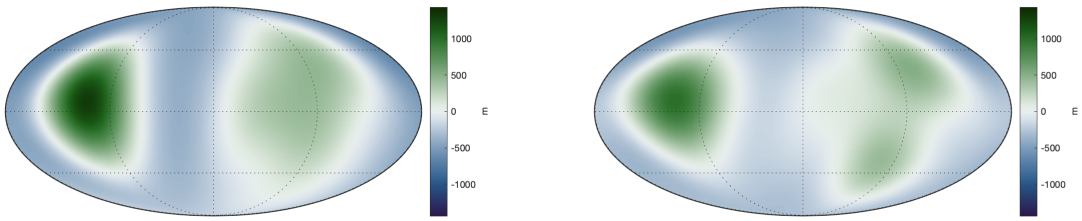

(a) Zero-elevation thickness of 45 km. C_{20} is removed for 95%.

(b) Zero-elevation thickness of 200 km. C_{20} is removed for 95%.

Figure A.3: Areoids (in meters) after crustal reduction of an Airy compensated crust with a zero-elevation crustal thickness of 100 km, a crustal density of 2900 kg/m^3 and a mantle density of 3550 kg/m^3. Both images are in Mollweide projection with a central meridian of 0 ° longitude. The lower limit of the colorbar is manually set to the negative of the maximum observed areoid.

For smaller zero-elevation crustal thicknesses, the areoid field in degrees 2-5 presents a more united antipodal (seen on the Eastern hemisphere). The antipodal for a thickness of 200 km shows two independent features, one being Utopia Planitia and one being Hellas Basin.

B

CROSS SECTIONS

This appendix visualizes a lateral cross-section of the best-fitting configurations. The longitudinal coordinates, radial limits of the density anomaly are indicated in the plot. The red area is the density anomaly placed inside the mantle. The solid black circles denotes the Martian core.

B.1. LATERAL CROSS-SECTION OF DA-MODELS

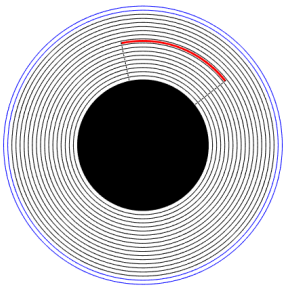

Longitude Coordinates: 142 W to 78 W deg
Bottom of anomaly = 2497 km
Top of anomaly = 2597 km

(a) Anomaly at a depth of 800 km down to 900 km.

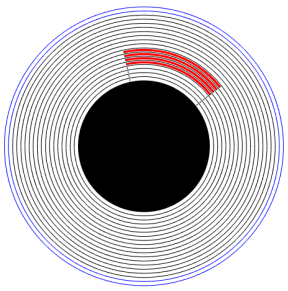

Longitude Coordinates: 142 W to 78 W deg
Bottom of anomaly = 1997 km
Top of anomaly = 2397 km

(b) Anomaly at a depth of 1000 km down to 1400 km.

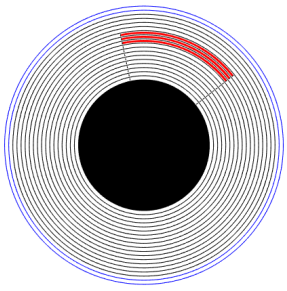

Longitude Coordinates: 142 W to 78 W deg
Bottom of anomaly = 2497 km
Top of anomaly = 2797 km

(c) Anomaly at a depth of 600 km down to 900 km.

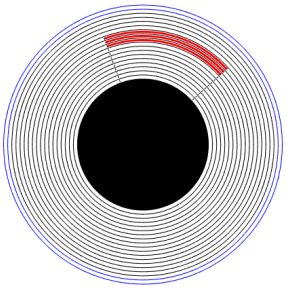

Longitude Coordinates: 138 W to 70 W deg
Bottom of anomaly = 2497 km
Top of anomaly = 2797 km

(d) Anomaly at a depth of 600 km down to 900 km.

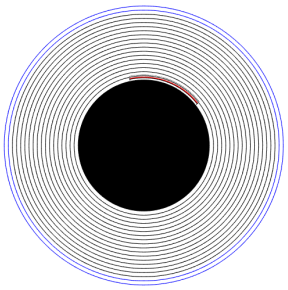

Longitude Coordinates: 142 W to 78 W deg
Bottom of anomaly = 1647 km
Top of anomaly = 1717 km

(e) Anomaly at a depth of 1680 km down to 1750 km.

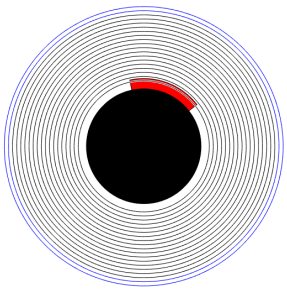

Longitude Coordinates: 142 W to 78 W deg
Bottom of anomaly = 1397 km
Top of anomaly = 1647 km

(f) Anomaly at a depth of 1750 km down to 2000 km. A smaller core has been used in this configuration (DA-CMB-2).

B.2. LATERAL CROSS-SECTION OF BD-MODELS

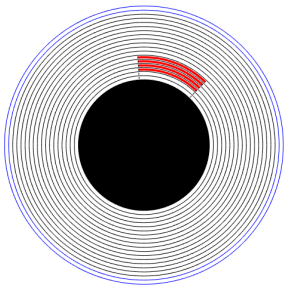

Longitude Coordinates: 134 W to 86 W deg
Bottom of anomaly = 1797 km
Top of anomaly = 2197 km

(a) Anomaly at a depth of 1200 km down to 1600 km.

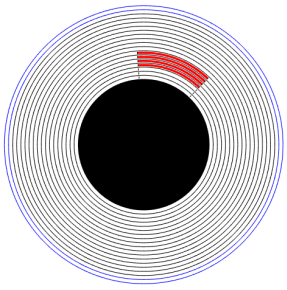

Longitude Coordinates: 134 W to 86 W deg
Bottom of anomaly = 1897 km
Top of anomaly = 2297 km

(b) Anomaly at a depth of 1100 km down to 1500 km.

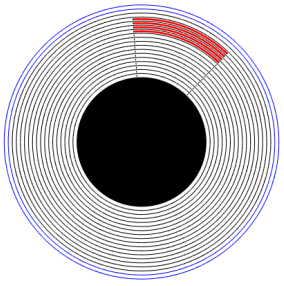

Longitude Coordinates: 134 W to 86 W deg
Bottom of anomaly = 2697 km
Top of anomaly = 3097 km

(c) Anomaly at a depth of 300 km down to 700 km.

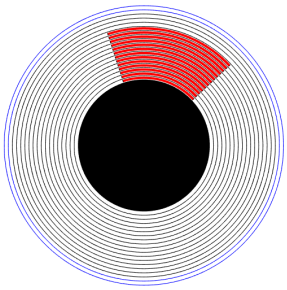

Longitude Coordinates: 137 W to 72 W deg
Bottom of anomaly = 1497 km
Top of anomaly = 2897 km

(d) Anomaly at a depth of 500 km down to CMB.

C

DA-Models Additional Information

This appendix contains supportive information for determination of the four fitting parameters used in the DA-Models. The fitting parameters are determined for the observed areoid and the modelled areoid field separately. This is done by selection the data at a latitude of 3 degrees N because this is the latitude at which the Tharsis bulge has a peak. Figure C.1 shows how the points in the areoid fields and in a 2D plot at the specified latitude. The approach to the calculation of each of the parameters is described below:

1. Highest gravity field value: determined by finding the locations where the differential of the areoid line equals zero and selecting the point where the areoid has the highest value.
2. Longitude distance (in degrees) from MP to the first zero-gravity line, computed by determining the longitudinal distance from parameter 1 to the most nearby zero-crossing to the right of the peak (at higher longitude)
3. Longitude distance (in degrees) from the first zero-potential line from MP to the second zero-potential line, computed by determining the second closest zero point to the right of the zero crossing found in the determination of parameter 2.
4. Ratio of MP and second maximum peak (often at the antipodal), the second peak is determined by finding the second highest point that has a zero differential with respect to longitude.

All four parameter values can be calculated with the information depicted in Table C.1 and Table C.2. Note that the zero areoid height are already the same, only the locations and magnitudes of the peaks deviate.

Table C.1: Observed peaks and zero areoid height locations

Peaks (m)	1105.5	360.7		
Locations (lon deg)	70.5	260.5		
Zero areoid height (lon)	28	120	190	312

Table C.2: Modelled peaks and zero areoid height locations

Peaks (m)	1195.4	399.3		
Locations (lon deg)	68.5	248.5		
Zero areoid height (lon)	28	120	190	312

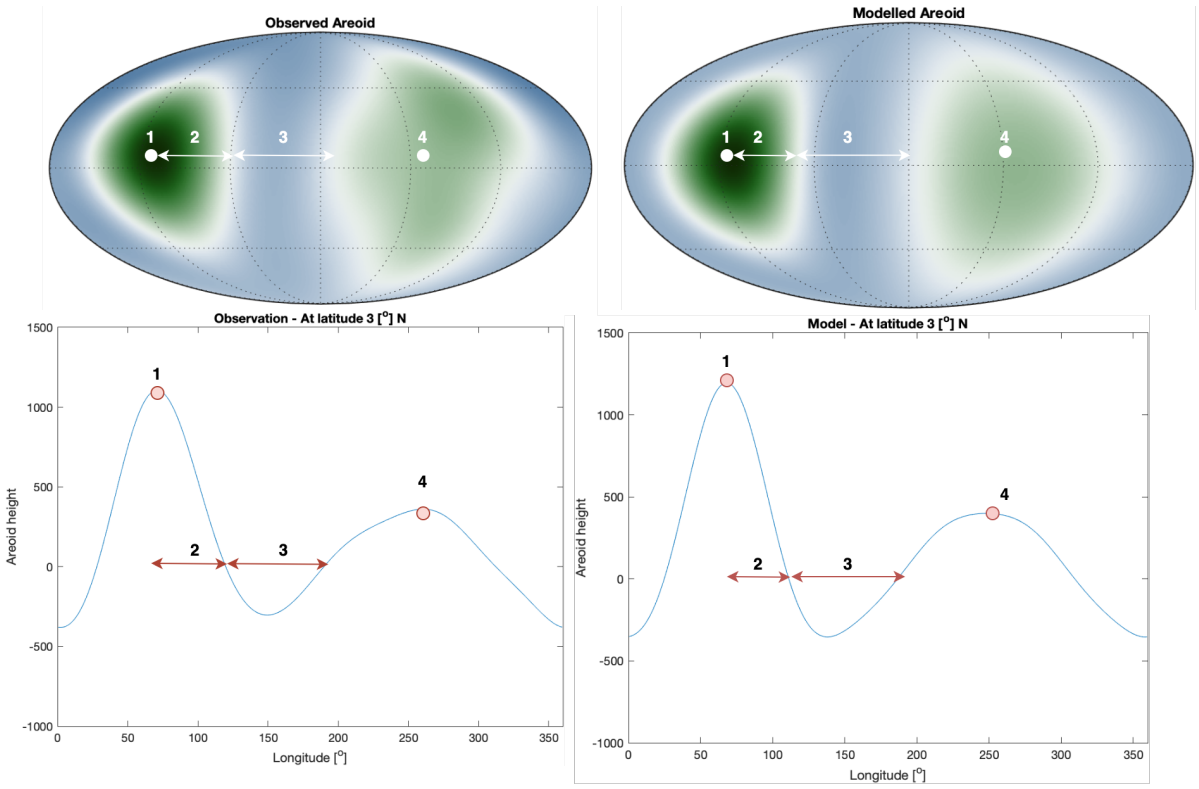

Figure C.1: Observed and modelled areoids. The magnitude of the areoid at a latitude of 3 ° N has been plotted and the four fitting parameters are indicated in the plot.

D

BD-Models Additional Information

This appendix contains supportive information for the interpretation of the results (heat maps) of the BD-Models that are presented in Section 4.3.

D.1. BD-Grav Models

For the BD-Grav-Full Models, the sensitivity of the solutions with respect to anomaly thickness, lithosphere thickness, spectral resolution and viscosity is analysed. Although the heat maps were already described in Chapter 4.3, the sensitivity is illustrated in more detail in the following section. Firstly, the baseline heat map is presented in Figure D.1.

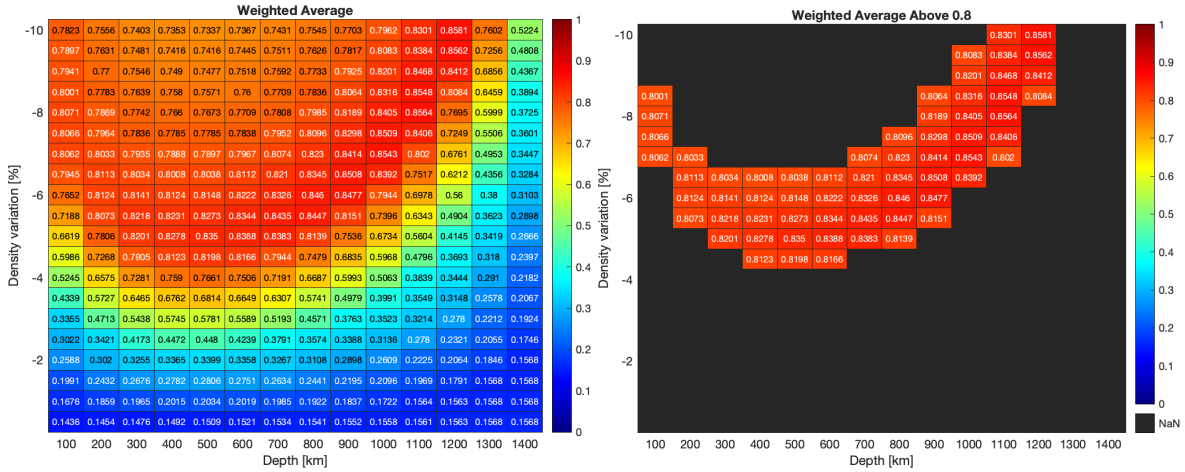

(a) Complete heat map.

(b) The models that produce a similarity above 0.8 (best-fitting regime).

Figure D.1: heat maps of the total (weighted) similarities of the BD-Grav-FULL Baseline. The closer the values are to one, the better the fit. The horizontal axis indicates at which depth (D_a) the anomaly starts (so first column starts at a depth of 100 km). The vertical axis presents the density variation $\frac{\Delta\rho}{\rho m} * 100\%$. The anomaly is centered at C_a = [70,3], has a thickness (T_a) of 400 km. Lateral sizes: $S_{lon,left}$ = 24, $S_{lon,right}$ = 24, $S_{lat,down}$ = 30 and $S_{lat,up}$ = 41 degrees.

This analyses presents four different heat maps (plots) for each configuration that is tested. Each set is presented in a separate subfigure. From left to right (column 1 to 4), the following is depicted:

- Left: complete heat map with the calculated average similarities, these heat maps were already presented in the results (Chapter 4).
- Middle left: the average similarities from the left heat map that exceed a similarity of 0.8 - this is the 'best-fitting' regime of this configuration.
- Middle right: the relative change in similarity of this configuration (left heat map) and the baseline heat map. Blue values indicate a decrease in similarity with respect to the baseline, red indicates an

increase and therefore a better performing model. A value close to 1 means that the solution did not change in similarity (with respect to the baseline). If the value is smaller/larger than one, the similarity decreased/increased.

- Right: the relative change in similarity of the best-fitting regime of the baseline. This is used to establish whether changing the configuration did lead to an improvement of the best-fitting solutions or whether is did not. A value close to 1 means that the solution did not change in similarity (with respect to the baseline). If the value is smaller/larger than one, the similarity decreased/increased.

With these plots, it can be determined which depth-density regime is improved by a change in configuration and which regime is not. For each configuration, the results will be briefly elaborated upon.

D.1.1. ANOMALY THICKNESS

The sensitivity of the solutions with respect to the thickness of the anomaly is illustrated in Figure D.2.

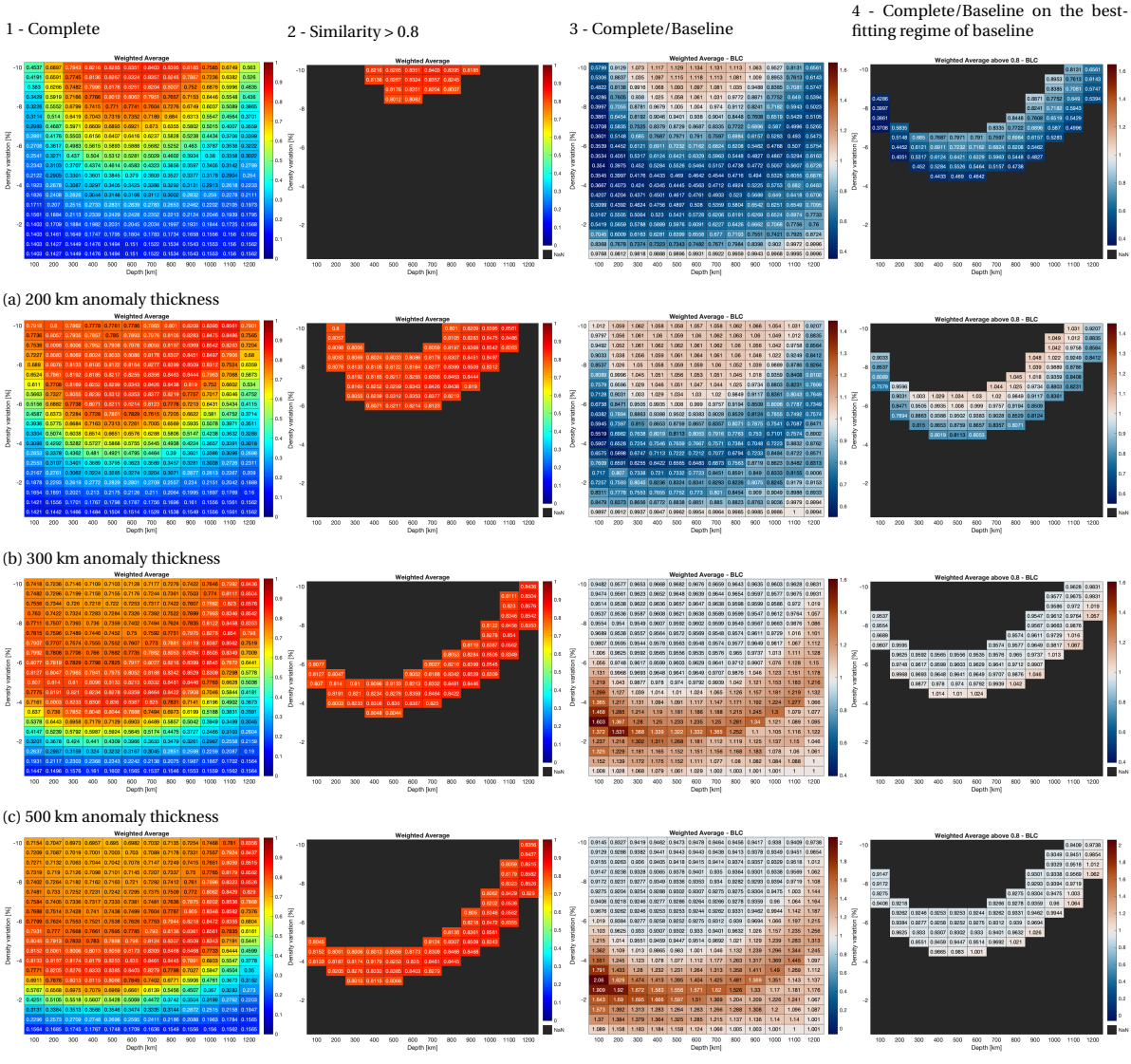

Figure D.2: Heat maps of the total (weighted) similarities of the BD-Grav-FULL varying the anomaly thickness. The horizontal axis indicates at which depth (D_a) the anomaly starts (so first column starts at a depth of 100 km). The vertical axis presents the density variation $\Delta\rho/\rho_m * 100\%$. The anomaly is centered at $C_a = [70, 3]$and has lateral sizes of: $S_{lon,left} = 24$, $S_{lon,right} = 24$, $S_{lat,down} = 30$ and $S_{lat,up} = 41$ degrees.

Column 1 and 2 clearly show that the regime of best-fitting solutions changes drastically when altering the

thickness of the anomaly. With respect to the baseline (column 3), it can be seen that if a smaller thickness is assumed (Figure D.2a and D.2b), only the configurations at very high density variation and at the middle of the mantle slightly improve in similarity. For the lower density variations, the similarities go down (blue in the heat maps). If the thickness of the anomaly is larger than the thickness of the baseline (Figure D.2c and D.2d), the solutions at a low density variation regime (-4% to 0%) improve. Column 4 depicts how the best-fitting regime of the baseline changes, they worsen significantly when assuming smaller anomaly thicknesses. Moreover, when assuming a larger thickness, the best-fitting from the baseline also decreases slightly (with a factor of 0.95-1).

D.1.2. LITHOSPHERE THICKNESS

The sensitivity of the solutions with respect to the thickness of the lithosphere is illustrated in Figure D.3.

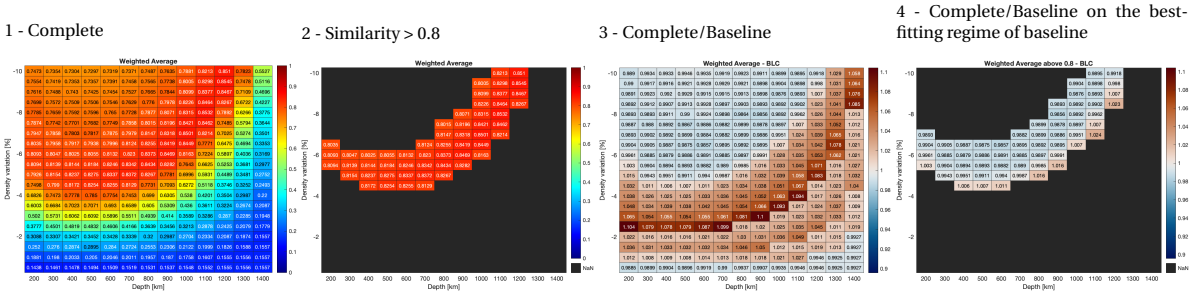

(a) 50 km lithosphere thickness

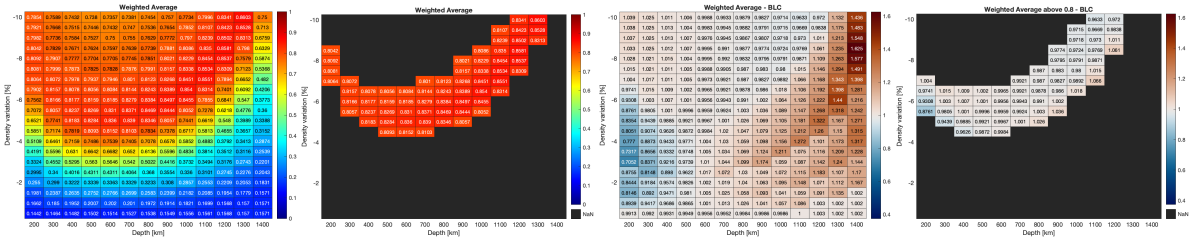

(b) 200 km lithosphere thickness

Figure D.3: Heat maps of the total (weighted) similarities of the BD-Grav-FULL varying the lithosphere thickness. The horizontal axis indicates at which depth (D_a) the anomaly starts (so first column starts at a depth of 100 km). The vertical axis presents the density variation $\Delta\rho/\rho_m * 100\%$. The anomaly is centered at $C_a = [70, 3]$ and has lateral sizes of: $S_{lon,left} = 24$, $S_{lon,right} = 24$, $S_{lat,down} = 30$ and $S_{lat,up} = 41$ degrees.

Column 1 and 2 do not show large differences in either the magnitude of the similarities or the best-fitting regime. Column three shows that shows that for a lithosphere thickness of 50 km (Figure D.3a), a band of solutions increases in similarity. For a thicker lithosphere of 200 km, there are no significant changes compared to a lithosphere of 100 km, except for solutions with a very high density variation just above the CMB (at a depth of 1400 km). The best-fitting regime of the baseline (column 4) does not show large similarity changes as a result of adjusting the lithosphere thickness.

D.1.3. SPECTRAL RESOLUTION

The sensitivity of the solutions with respect to the spectral is illustrated in Figure D.4.

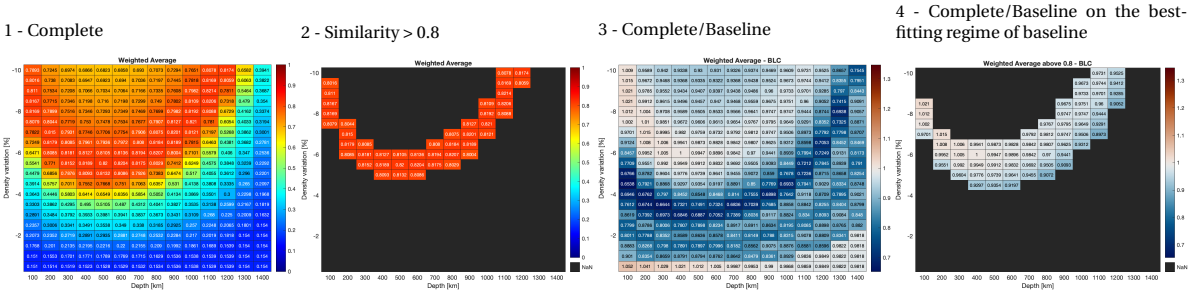

(a) SH 2-3

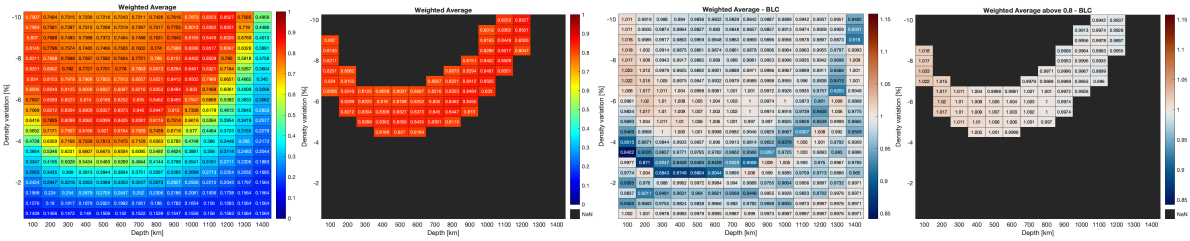

(b) SH 2-4

Figure D.4: Heat maps of the total (weighted) similarities of the BD-Grav-FULL varying SH degrees to 2-3 and 2-4. The horizontal axis indicates at which depth (D_a) the anomaly starts (so first column starts at a depth of 100 km). The vertical axis presents the density variation $\Delta\rho/\rho_m * 100\%$. The anomaly is centered at C_a = [70,3] and has lateral sizes of: $S_{lon,left}$ = 24, $S_{lon,right}$ = 24, $S_{lat,down}$ = 30 and $S_{lat,up}$ = 41 degrees.

When researching SH degrees 2-4, a broader band of solutions results in a similarity above 0.8 compared to the solutions for SH 2-3. Moreover, the similarities of both a spectral resolution of 2-4 and 2-3 are in general lower compared to the similarities at SH 2-5. Although several solutions at shallow depth and high density variation show a light red color in columns 3 and 4, indicating a slight increase in similarity.

D.1.4. VISCOSITY

The sensitivity of the solutions with respect to viscosity profile is illustrated in Figure D.5.

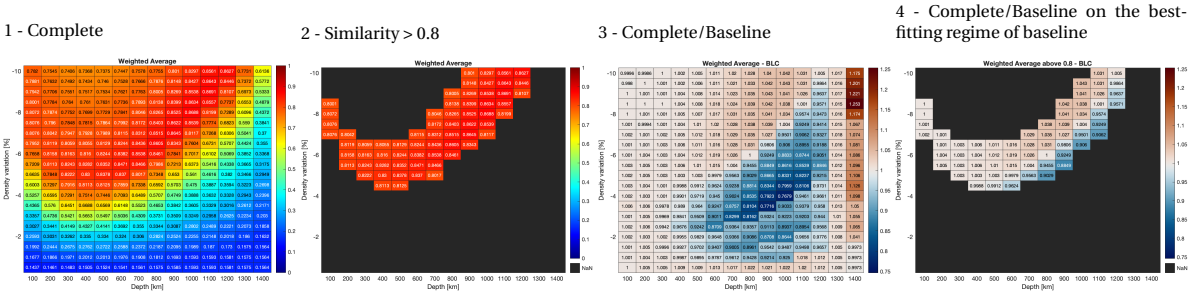

(a) Profile 2

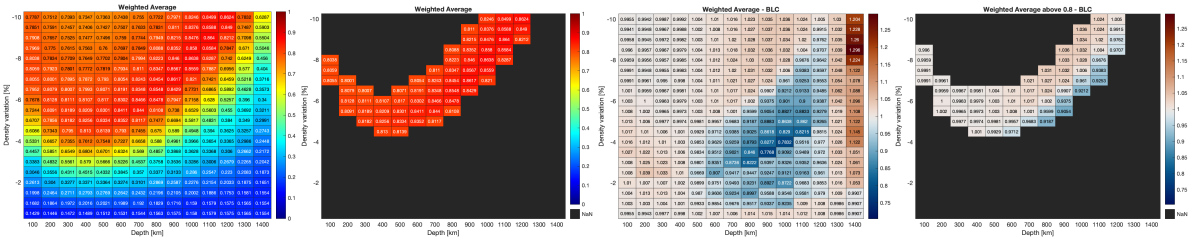

(b) Profile 3

Figure D.5: Heat maps of the total (weighted) similarities of the BD-Grav-FULL varying the viscosity profile. The horizontal axis indicates at which depth (D_a) the anomaly starts (so first column starts at a depth of 100 km). The vertical axis presents the density variation $\Delta\rho/\rho_m * 100\%$. The anomaly is centered at C_a = [70,3] and has lateral sizes of: $S_{lon,left}$ = 24, $S_{lon,right}$ = 24, $S_{lat,down}$ = 30 and $S_{lat,up}$ = 41 degrees.

The plots for changing the viscosity profile from profile 1 to 2 (Figure D.5a) or 3 (Figure D.5b) look very similar. In both cases, only a specific region (from a depth of about 700 km down to 1200 km, and a. density variation between -2% and -8%) contains solutions that decrease in similarity. However, in the best-fitting range from the baseline (profile 1), the models do not perform worse. The difference between profile 2 and 3 is a higher viscosity in the top layers of profile 3. Besides some minor differences, this effect is not visible in the heat maps.

D.1.5. SOLID CORE

The similarity heat maps under the assumption of a solid core is illustrated in Figure D.6.

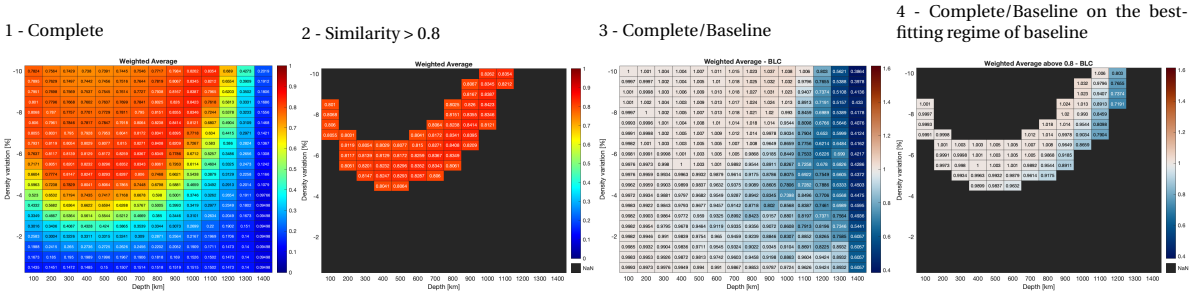

Figure D.6: Heat map of the total (weighted) similarities of BD-Grav-SC. The closer the values are to one, the better the fit. The horizontal axis indicates at which depth (D_a) the anomaly starts (so first column starts at a depth of 100 km). The vertical axis presents the density variation $\frac{\Delta\rho}{\rho_m} * 100\%$. The anomaly is centered at C_a = [70,3]and has lateral sizes of: $S_{lon,left}$ = 24, $S_{lon,right}$ = 24, $S_{lat,down}$ = 30 and $S_{lat,up}$ = 41 degrees.

Only the solutions close to the CMB (at large depths, especially 1400 km) are affected by the change in configuration. The solutions that are located on top of the CMB are worsened significantly (deep blue).

D.2. BD-HYBRID MODELS

For the BD-Hybrid-UC Models, the sensitivity of the solutions with respect to anomaly thickness, lithosphere thickness, spectral resolution and viscosity is analysed. Although the heat maps were already described in Chapter 4.3, the sensitivity is illustrated in more detail in the following section. Firstly, the baseline heat map is presented in Figure D.7.

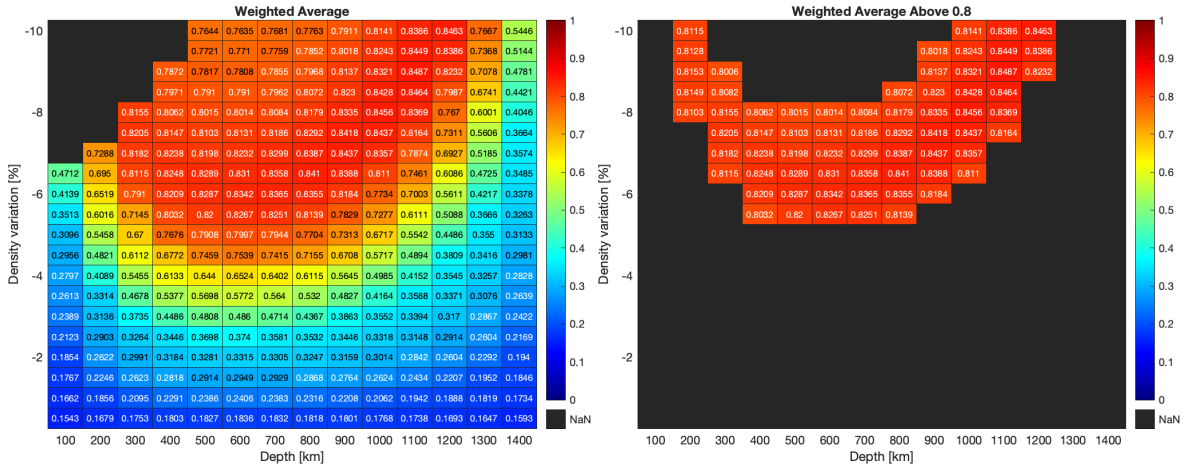

(a) Complete heat map.

(b) The models that produce a similarity above 0.8 (best-fitting regime).

Figure D.7: Heat maps of the total (weighted) similarities of the BD-Hybrid-UC Baseline. The closer the values are to one, the better the fit. The horizontal axis indicates at which depth (D_a) the anomaly starts (so first column starts at a depth of 100 km). The vertical axis presents the density variation $\frac{\Delta\rho}{\rho_m} * 100\%$. The anomaly is centered at C_a = [70,3], has a thickness (T_a) of 400 km. Lateral sizes: $S_{lon,left}$ = 24, $S_{lon,right}$ = 24, $S_{lat,down}$ = 30 and $S_{lat,up}$ = 41 degrees.

D.2.1. ANOMALY THICKNESS

The sensitivity of the solutions with respect to the thickness of the anomaly is illustrated in Figure D.8.

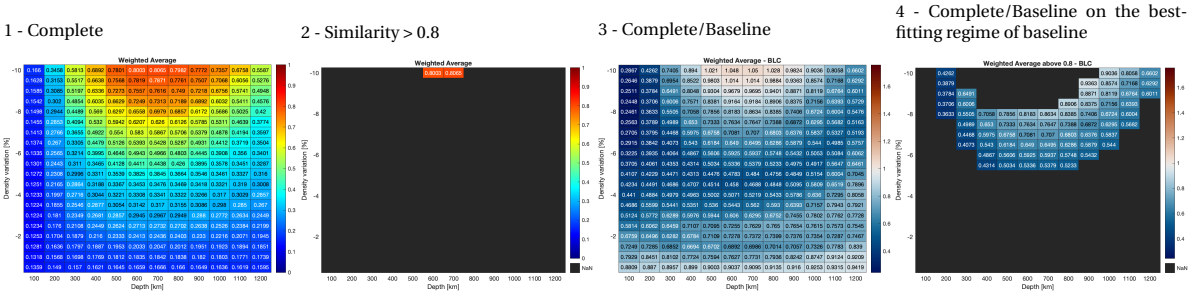

(a) 200 km anomaly thickness

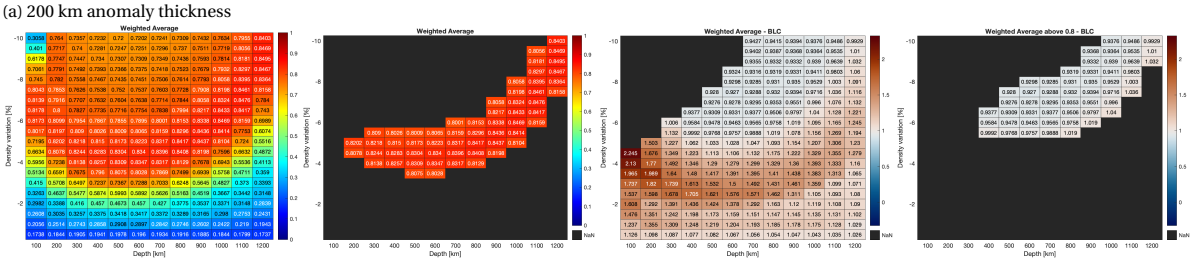

(b) 600 km anomaly thickness

Figure D.8: Heat map of the total (weighted) similarities of the BD-Hybrid-UC varying the anomaly thickness. The closer the values are to one, the better the fit. The horizontal axis indicates at which depth (D_a) the anomaly starts (so first column starts at a depth of 100 km). The vertical axis presents the density variation $\Delta\rho/\rho_m * 100\%$. The anomaly is centered at $C_a = [70,3]$ and lateral sizes of $S_{lon,left} = 24$, $S_{lon,right} = 24$, $S_{lat,down} = 30$ and $S_{lat,up} = 41$ degrees.

Figure D.8a shows that there are only two solutions for a 200 km thick anomaly that result in a similarity above 0.8 Compared to the baseline of the BD-Hybrid-UC study, the heat maps (column 3 and 4) are colored blue, indicating a decrease in similarity. For an anomaly of 600 km thick (Figure D.8b, so 200 km thicker than the baseline, some is visible in the heat map in column 3. For the best-fitting solutions from the baseline that are also valid for the 600 km anomaly thickness configuration, the heat map (column 4) shows a small decrease in similarity for almost all solutions.

D.2.2. LITHOSPHERE THICKNESS

The sensitivity of the solutions with respect to the thickness of the lithosphere is illustrated in Figure D.9.

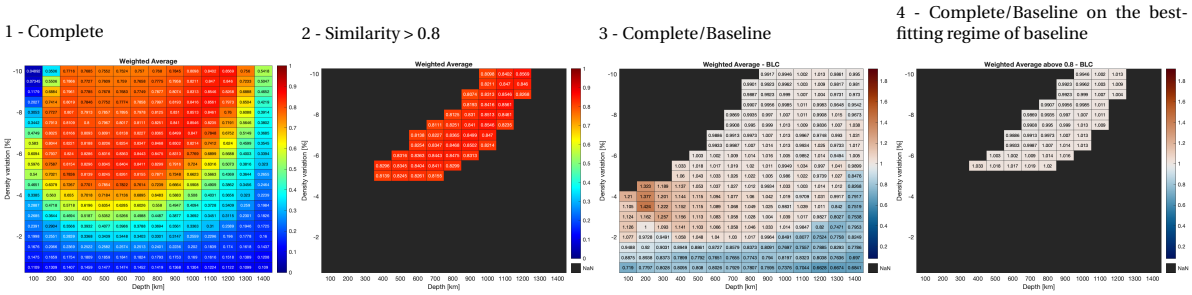

(a) 50 km lithosphere thickness

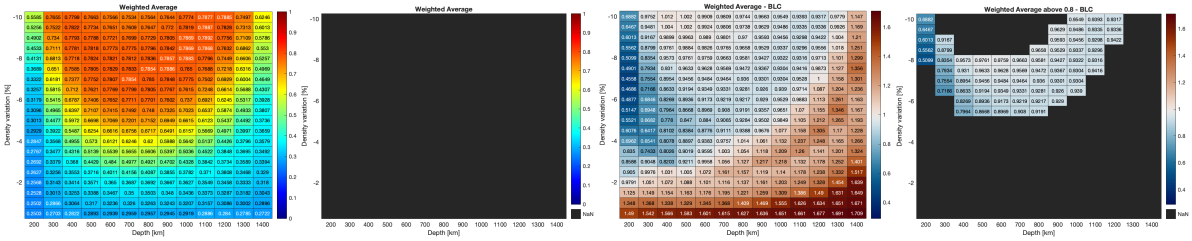

(b) 200 km lithosphere thickness

Figure D.9: Heat map of the total (weighted) similarities of the BD-Hybrid-UC varying the lithosphere thickness. The closer the values are to one, the better the fit. The horizontal axis indicates at which depth (D_a) the anomaly starts (so first column starts at a depth of 100 km). The vertical axis presents the density variation $\Delta\rho/\rho_m * 100\%$. The anomaly is centered at C_a = [70,3], has a thickness (T_a) of 400 km. Lateral sizes: $S_{lon,left}$ = 24, $S_{lon,right}$ = 24, $S_{lat,down}$ = 30 and $S_{lat,up}$ = 41 degrees.

It should be noted that assuming a thinner lithosphere (Figure D.9a) decreases the similarities of small density variations from 0 to -2%. But the similarities are slightly increased for the larger density variations. For a lithosphere thickness of 200 km, there were no models that resulted in a similarity above 0.8. It worsened all the best-fitting solutions of the baseline study (as can be derived from the completely blue heat map in Figure D.9b, column 4).

D.2.3. SPECTRAL RESOLUTION

The sensitivity of the solutions with respect to the spectral resolution is illustrated in Figure D.10.

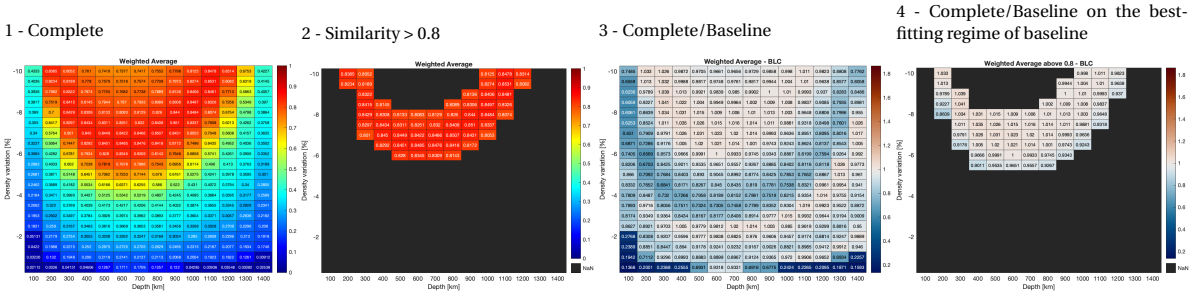

(a) SH 2-3

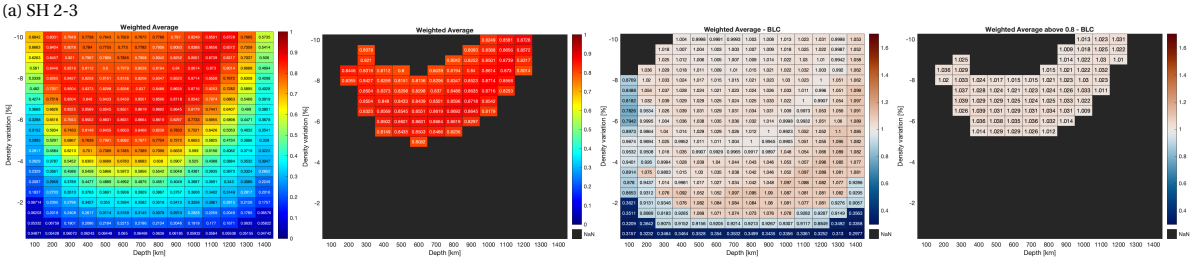

(b) SH 2-4

Figure D.10: Heat map of the total (weighted) similarities of the BD-Hybrid-UC varying the spectral resolution. The closer the values are to one, the better the fit. The horizontal axis indicates at which depth (D_a) the anomaly starts (so first column starts at a depth of 100 km). The vertical axis presents the density variation $\Delta\rho/\rho_m * 100\%$. The anomaly is centered at C_a = [70,3], has a thickness (T_a) of 400 km. Lateral sizes: $S_{lon,left}$ = 24, $S_{lon,right}$ = 24, $S_{lat,down}$ = 30 and $S_{lat,up}$ = 41 degrees.

Similar to the results for BD-Grav-Full, changing the spectral resolution does not significantly influence the best-fitting results from the baseline. This can be derived from the values in the heat maps in column 4, which are all close to 1 (meaning there is no difference with the baseline). A dark blue line is visible at small density variations at all depths in the heat maps in column 3. This is an artifact of the software that computes the similarity, it is not able to distinguish the correct zero-potential areoid lines in these cases.

D.2.4. VISCOSITY

The sensitivity of the solutions with respect to the viscosity is illustrated in Figure D.11.

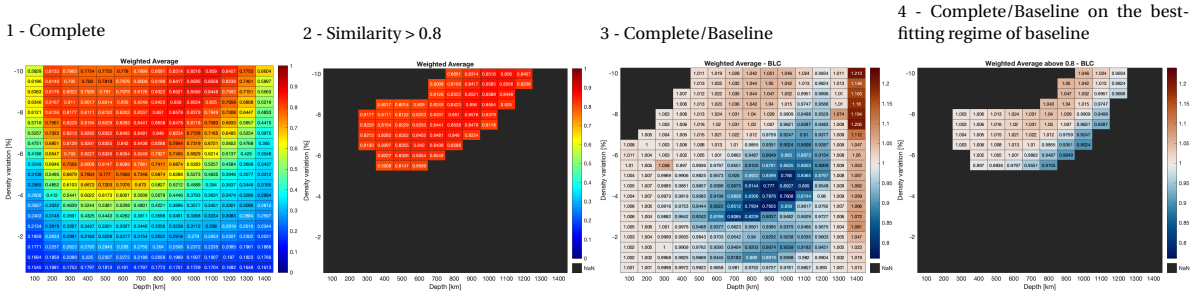

(a) Profile 2

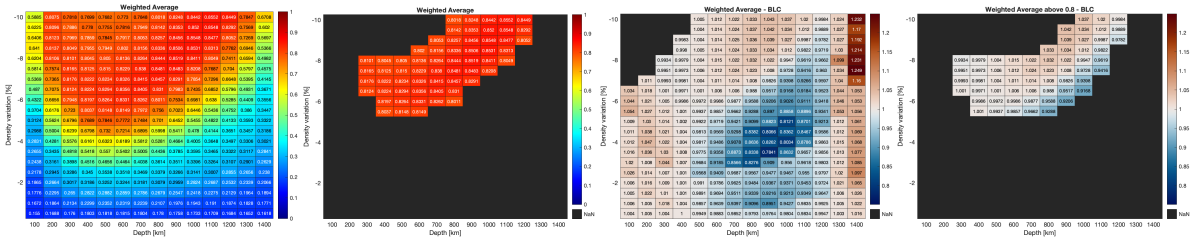

(b) Profile 3

Figure D.11: Heat map of the total (weighted) similarities of the BD-Hybrid-UC varying the viscosity profile. The closer the values are to one, the better the fit. The horizontal axis indicates at which depth (D_a) the anomaly starts (so first column starts at a depth of 100 km). The vertical axis presents the density variation $\Delta\rho/\rho_m * 100\%$. The anomaly is centered at C_a = [70,3], has a thickness (T_a) of 400 km. Lateral sizes: $S_{lon,left}$ = 24, $S_{lon,right}$ = 24, $S_{lat,down}$ = 30 and $S_{lat,up}$ = 41 degrees.

Similar to the solutions found in the BD-Grav-Full study, changing the viscosity profile does not have a significant impact on the best-fitting solutions of the baseline study, as can be seen in the heat maps in column four. All values are close to one, meaning no changes with respect to the baseline.

BIBLIOGRAPHY

Anderson, D. L. (1981), 'Hotspots, polar wander, Mesozoic convection and the geoid.', *Nature* **297**(June), 391–393.

Ardalan, A. A., Karimi, R. and Grafarend, E. W. (2010), 'A New Reference Equipotential Surface, and Reference Ellipsoid for the Planet Mars', *Earth Moon and Planets* **106**(1), 1–13.

Austermann, J., Kaye, B. T., Mitrovica, J. X. and Huybers, P. (2014), 'A statistical analysis of the correlation between large igneous provinces and lower mantle seismic structure', *Geophysical Journal International* **197**(1), 1–9.

Backer, L. D. (2018), 'Seismic analysis of Mars using gravitational potential stresses - InSight', *MSc. Thesis* .

Banerdt, W. B., Phillips, R. J., Sleep, N. H. and Saunders, R. S. (1982), 'Thick shell tectonics on one-plate planets: Applications to Mars', *Journal of Geophysical Research* **87**(B12), 9723.

Becker, T. W. and Boschi, L. (2002), 'A comparison of tomographic and geodynamic mantle models', *Geochemistry, Geophysics, Geosystems* **3**(1), n/a–n/a.

Böse, M., Clinton, J. F., Ceylan, S., Euchner, F., van Driel, M., Khan, A., Giardini, D., Lognonné, P. and Banerdt, W. B. (2017), 'A probabilistic framework for single-station location of seismicity on Earth and Mars', *Physics of the Earth and Planetary Interiors* **262**, 48–65.

Breuer, D., Zhou, H. and Yuen, D. A. (1996), 'Implications for the planet's volcanic history stability', *Journal of Geophysical Research* **101**(96), 7531–7542.

Burke, K., Steinberger, B., Torsvik, T. H. and Smethurst, M. A. (2008), 'Plume Generation Zones at the margins of Large Low Shear Velocity Provinces on the core-mantle boundary', *Earth and Planetary Science Letters* **265**(1-2), 49–60.

Burke, K. and Torsvik, T. H. (2004), 'Derivation of Large Igneous Provinces of the past 200 million years from long-term heterogeneities in the deep mantle', *Earth and Planetary Science Letters* **227**(3-4), 531–538.

Burke, K., Werner, S. C., Steinberger, B. and Torsvik, T. H. (2012), 'Why is the areoid like the residual geoid?', *Geophysical Research Letters* **39**(17).
URL: *https://agupubs.onlinelibrary.wiley.com/doi/abs/10.1029/2012GL052701*

Carr, M. H. (1974), 'Tectonism and volcanism of the Tharsis Region of Mars', *Journal of Geophysical Research* **79**(26), 3943–3949.

Courtillot, V., Davaille, A., Besse, J. and Stock, J. (2003), 'Three distinct types of hotspots in the Earth's mantle', *Earth and Planetary Science Letters* **205**(3-4), 295–308.

Davaille, A. and Romanowicz, B. (2020), 'Deflating the LLSVPs: Bundles of Mantle Thermochemical Plumes Rather Than Thick Stagnant "Piles"', *Tectonics* **39**(10), 1–21.

Davies, D. R., Goes, S. and Sambridge, M. (2015), 'On the relationship between volcanic hotspot locations, the reconstructed eruption sites of large igneous provinces and deep mantle seismic structure', *Earth and Planetary Science Letters* **411**(February), 121–130.

DePaolo, D. J. and Manga, M. (2003), 'Deep origin of hotspots - The mantle plume model', *Science* **300**(5621), 920–921.

Doubrovine, P. V., Steinberger, B. and Torsvik, T. H. (2016), 'A failure to reject: Testing the correlation between large igneous provinces and deep mantle structures with edf statistics', *Geochemistry, Geophysics, Geosystems* **17**(3), 1130–1163.

Dziewonski, A. M. and Anderson, D. L. (1981), 'Preliminary reference earth model', *Physics of the Earth and Planetary Interiors* **25**(4), 297 – 356.

Fowler, C. M. R. (2004), *The Solid Earth: An Introduction to Global Geophysics*, 2 edn, Cambridge University Press.

Genova, A., Goossens, S., Lemoine, F. G., Mazarico, E., Neumann, G. A., Smith, D. E. and Zuber, M. T. (2016), 'Seasonal and static gravity field of Mars from MGS, Mars Odyssey and MRO radio science', *Icarus* **272**, 228–245.

Golabek, G. J., Keller, T., Gerya, T. V., Zhu, G., Tackley, P. J. and Connolly, J. A. (2011), 'Origin of the martian dichotomy and Tharsis from a giant impact causing massive magmatism', *Icarus* **215**(1), 346–357.

Goossens, S., Sabaka, T. J., Genova, A., Mazarico, E., Nicholas, J. B. and Neumann, G. A. (2017), 'Evidence for a low bulk crustal density for mars from gravity and topography', *Geophysical Research Letters* **44**(15), 7686–7694.

Goossens, S., Sabaka, T. J., Wieczorek, M. A., Neumann, G. A., Mazarico, E., Lemoine, F. G., Nicholas, J. B., Smith, D. E. and Zuber, M. T. (2020), 'High-Resolution Gravity Field Models from GRAIL Data and Implications for Models of the Density Structure of the Moon's Crust', *Journal of Geophysical Research: Planets* **125**(2), 1–31.

Gripp, A. E. and Gordon, R. G. (1990), 'Current plate velocities relative to the hotspots incorporating the nuvel-1 global plate motion model', *Geophysical Research Letters* **17**(8), 1109–1112.

Hager, B. H. (1984), 'Subducted slabs and the geoid: Constraints on mantle rheology and flow', *Journal of Geophysical Research: Solid Earth* **89**(B7), 6003–6015.
URL: *https://agupubs.onlinelibrary.wiley.com/doi/abs/10.1029/JB089iB07p06003*

Hahn, B. C., McLennan, S. M. and Klein, E. C. (2011), 'Martian surface heat production and crustal heat flow from Mars Odyssey Gamma-Ray spectrometry', *Geophysical Research Letters* **38**(14), 1–5.

Harder, H. and Christensen, U. R. (1996), 'A one-plume model of martian mantle convection', *Nature* **380**(6574), 507–509.

Heyn, B. H., Conrad, C. P. and Trønnes, R. G. (2020), 'Core-mantle boundary topography and its relation to the viscosity structure of the lowermost mantle', *Earth and Planetary Science Letters* **543**, 116358.
URL: *https://doi.org/10.1016/j.epsl.2020.116358*

Ishii, M. and Tromp, J. (1999), 'Normal-mode and free-air gravity constraints on lateral variations in velocity and density of earth's mantle', *Science* **285**(5431), 1231–1236.

Kiefer, W. S. and Hager, B. H. (1989), 'The Role of Mantle Convection in the Origin of the Tharsis and Elysium Provinces of Mars', *MEVTV Workshop on Early Tectonic and Volcanic Evolution of Mars* pp. 48–50.

Kimura, J.-I. and Kawabata, H. (2015), 'Geochemistry, Geophysics, Geosystems', *Geochemistry Geophysics Geosystems* **16**(1), 267–300.

Knapmeyer, M. (2011), 'Planetary core size: A seismological approach', *Planetary and Space Science* **59**(10), 1062–1068.
URL: *http://dx.doi.org/10.1016/j.pss.2010.03.016*

Knapmeyer, M., Oberst, J., Hauber, E., Wählisch, M., Deuchler, C. and Wagner, R. (2006), 'Working models for spatial distribution and level of mars' seismicity', *Journal of Geophysical Research: Planets* **111**(E11).
URL: *https://agupubs.onlinelibrary.wiley.com/doi/abs/10.1029/2006JE002708*

Koelemeijer, P., Deuss, A. and Ritsema, J. (2017), 'Density structure of Earth's lowermost mantle from Stoneley mode splitting observations', *Nature Communications* **8**(May), 1–10.

Li, M. and Zhong, S. (2017), 'The source location of mantle plumes from 3D spherical models of mantle convection', *Earth and Planetary Science Letters* **478**, 47–57.

Li, M., Zhong, S. and Olson, P. (2018), 'Linking lowermost mantle structure, core-mantle boundary heat flux and mantle plume formation', *Physics of the Earth and Planetary Interiors* **277**(January), 10–29.

McGovern, P. J., Solomon, S. C., Smith, D. E., Zuber, M. T., Simons, M., Wieczorek, M. A., Phillips, R. J., Neumann, G. A., Aharonson, O. and Head, J. W. (2002), 'Localized gravity/topography admittance and correlation spectra on Mars: Implications for regional and global evolution', *Journal of Geophysical Research Planets* **107**(12), 19–1.

McNamara, A. K. and Zhong, S. (2005), 'Thermochemical structures beneath Africa and the Pacific Ocean', *Nature* **437**(7062), 1136–1139.

Mège, D. and Masson, P. (1996), 'Stress models for Tharsis formation, Mars', *Planetary and Space Science* **44**(12), 1471–1497.

Michel, N. and Forni, O. (2011), 'Mars mantle convection: Influence of phase transitions with core cooling', *Planetary and Space Science* **59**(8), 741–748.
URL: *http://dx.doi.org/10.1016/j.pss.2011.02.013*

Montelli, R., Nolet, G., Dahlen, F. A. and Masters, G. (2006), 'A catalogue of deep mantle plumes: New results from finitefrequency tomography', *Geochemistry, Geophysics, Geosystems* **7**(11).

Mussini, J. (2020), 'An anisotropic flexural isostasy method for investigating the Martian lithosphere'.

NASA (1999), 'Tharsis rise (true color)'. Accessed: 2021-02-01.
URL: *https://svs.gsfc.nasa.gov/654*

Neukum, G. and Hiller, K. (1981), 'Martian ages', *Journal of Geophysical Research: Solid Earth* **86**(B4), 3097–3121.

Neumann, G. A., Zuber, M. T., Wieczorek, M. A., McGovern, P. J., Lemoine, F. G. and Smith, D. E. (2004), 'Crustal structure of Mars from gravity and topography', *Journal of Geophysical Research Planets* **109**(8), 1–18.

Ni, S., Tan, E., Gurnis, M. and Helmberger, D. (2002), 'Sharp sides to the African superplume', *Science* **296**(5574), 1850–1852.

Phillips, R. J., Zuber, M. T., Solomon, S. C., Golombek, M. P., Jakosky, B. M., Banerdt, W. B., Smith, D. E., Williams, R. M., Hynek, B. M., Aharonson, O. and Hauck, S. A. (2001), 'Ancient geodynamics and global-scale hydrology on Mars', *Science* **291**(5513), 2587–2591.

Plesa, A. C., Padovan, S., Tosi, N., Breuer, D., Grott, M., Wieczorek, M. A., Spohn, T., Smrekar, S. E. and Banerdt, W. B. (2018), 'The Thermal State and Interior Structure of Mars', *Geophysical Research Letters* **45**(22), 12,198–12,209.

Redmond, H. L. and King, S. D. (2004), 'A numerical study of a mantle plume beneath the Tharsis Rise: Reconciling dynamic uplift and lithospheric support models', *Journal of Geophysical Research Planets* **109**(9), 1–14.

Richards, M. A., Duncan, R. A. and Courtillot, V. E. (1989), 'Flood basalts and hot-spot tracks: Plume heads and tails', *Science* **246**(4926), 103–107.

Robbins, S. and Achille, G. D. (2011), 'Timeline of Martian Volcanism: High-Resolution Crater-Based Studies of the Calderas of 20 Volcanoes', *Icarus* pp. 1179–1203.

Root, B., Novák, P., Dirkx, D., Kaban, M., Van der Wal, W. and Vermeersen, L. (2016), 'On a spectral method for forward gravity field modelling', *Journal of Geodynamics* **97**, 22–30.

Schubert, Bercovici, G. (1990), 'Lithosphere on Three-Dimensional Mantle Convection ß (Os ' v '', **90**.

Sheriff, R. E. and Geldart, L. P. (1995), *Exploration Seismology*, 2 edn, Cambridge University Press.

Smith, D. e. a. (2003), 'Mars global surveyor laser altimeter mission experiment gridded data record'. Accessed: 2021-02-01.
URL: $https://pds-geosciences.wustl.edu/mgs/mgs-m-mola-5-megdr-l3-v1/mgsl_300x/$

Steinberger, B. (2000), 'Plumes in a convecting mantle: Models and observations for individual hotspots', *Journal of Geophysical Research: Solid Earth* **105**(B5), 11127–11152.

Steinberger, B. and O'Connell, R. J. (1998), 'Advection of plumes in mantle flow: Implications for hotspot motion, mantle viscosity and plume distribution', *Geophysical Journal International* **132**(2), 412–434.

Steinberger, B., Werner, S. C. and Torsvik, T. H. (2010), 'Deep versus shallow origin of gravity anomalies, topography and volcanism on Earth, Venus and Mars', *Icarus* **207**(2), 564–577.

Tan, E., Leng, W., Zhong, S. and Gurnis, M. (2011), 'On the location of plumes and lateral movement of thermochemical structures with high bulk modulus in the 3-D compressible mantle', *Geochemistry, Geophysics, Geosystems* **12**(7), 1–13.

Torsvik, T. H., Burke, K., Steinberger, B., Webb, S. J. and Ashwal, L. D. (2010), 'Diamonds sampled by plumes from the core-mantle boundary', *Nature* **466**(7304), 352–355.

Torsvik, T. H., Smethurst, M. A., Burke, K. and Steinberger, B. (2006), 'Large igneous provinces generated from the margins of the large low-velocity provinces in the deep mantle', *Geophysical Journal International* **167**(3), 1447–1460.

Tosi, N. (2007), 'Numerical modeling of present-day mantle convection', *Thesis* (c).

Trampert, J., Deschamps, F., Resovsky, J. and Yuen, D. (2004), 'Probabilistic tomography maps chemical heterogeneities throughout the lower mantle', *Science* **306**(5697), 853–856.

Trønnes, R. G. (2010), 'Structure, mineralogy and dynamics of the lowermost mantle', *Mineralogy and Petrology* **99**(3-4), 243–261.

Turcotte, D., Willemann, R., Haxby, W. and Norberry, J. (1981), 'Role of membrane stress in the support of planetary topography', *Journal of Geophysical Research* **86**.

Van Der Wal, W., Barnhoorn, A., Stocchi, P., Gradmann, S., Wu, P., Drury, M. and Vermeersen, B. (2013), 'Glacial isostatic adjustment model with composite 3-D Earth rheology for Fennoscandia', *Geophysical Journal International* **194**(1), 61–77.

Watts, A. (2001), *Isostasy and Flexure of the Lithosphere*, Vol. 458.

Werner, S. C. (2009), 'The global martian volcanic evolutionary history', *Icarus* **201**(1), 44–68.

Wieczorek, M. (2007), 'Gravity and Topography of the Terrestrial Planets', *Volume 10: Planets and Moons* (January 2006), 165–206.

Wieczorek, M. A. (2015), *Gravity and Topography of the Terrestrial Planets*, Vol. 10, Elsevier B.V.
URL: *http://dx.doi.org/10.1016/B978-0-444-53802-4.00169-X*

Wieczorek, M. A. and Simons, F. J. (2005), 'Localized spectral analysis on the sphere', *Geophysical Journal International* **162**(3), 655–675.

Wieczorek, M. A. and Zuber, M. T. (2004), 'Thickness of the Martian crust: Improved constraints from geoid-to-topography ratios', *Journal of Geophysical Research E: Planets* **109**(1), 1–16.

Wise, D. U., Golombek, M. P. and McGill, G. E. (1979), 'Tharsis province of Mars: Geologic sequence, geometry, and a deformation mechanism', *Icarus* **38**(3), 456–472.

Zhang, N., Zhong, S. and Flowers, R. M. (2012), 'Predicting and testing continental vertical motion histories since the Paleozoic', *Earth and Planetary Science Letters* **317-318**, 426–435.

Zhong, S. (2002), 'Effects of lithosphere on the long-wavelength gravity anomalies and their implications for the formation of the Tharsis rise on Mars', *Journal of Geophysical Research Planets* **107**(7), 8–1.

Zhong, S. and Liu, X. (2016), 'The long-wavelength mantle structure and dynamics and implications for large-scale tectonics and volcanism in the Phanerozoic', *Gondwana Research* **29**(1), 83–104.

Zhong, S. and Roberts, J. H. (2003), 'On the support of the Tharsis Rise on Mars', *Earth and Planetary Science Letters* **214**(1-2), 1–9.

Zuber, M. T. (2000), 'Internal structure and early thermal evolution of Mars from Mars global surveyor topography and gravity', *Science* **287**(5459), 1788–1793.

Zuber, M. T. and Smith, D. E. (1997), 'Mars without tharsis', *Journal of Geophysical Research E: Planets* **102**(E12), 28673–28685.